Journal of
Materials Chemistry A

ROYAL SOCIETY
OF CHEMISTRY

REVIEW

View Article Online
View Journal | View Issue

Cite this: *J. Mater. Chem. A*, 2024, **12**, 28618

Artificial CO_2 photoreduction: a review of photocatalyst design and product selectivity regulation

Chen Fu, Zhenyu Wan, Xin Yang, Junhui Zhang and Zizhong Zhang *

Received 3rd July 2024
Accepted 14th September 2024

DOI: 10.1039/d4ta04600e

rsc.li/materials-a

Mimicking natural photosynthesis, artificial photosynthesis for the reduction of CO_2 into valuable hydrocarbon fuels is a promising approach for solar energy utilization and carbon neutrality. However, great challenges are present in the development of efficient photocatalysts for CO_2 reduction and controlling the selectivity for reduction products. This review summarizes the progress in photocatalyst design strategies to improve the efficiency and selectivity of photocatalytic CO_2 reduction. Six popular modification methods are introduced, namely, creation of defect structures, cocatalyst loading, doping, heterojunction formation, single-atom engineering, and surface organometallic catalysis. The effects of these different strategies on the promotion of light absorption, charge separation and migration and catalyst surface reactions in the process of CO_2 reduction are analyzed. In addition, the latest research results on selective reduction to C_1, C_2, and C_{2+} products in CO_2 and H_2O systems are summarized. Finally, the article delves into the future prospects and inherent hurdles in photocatalyst design, focusing on enhancing the selectivity of CO_2 conversion towards specific products. This review provides insights into the efficiency and selectivity of photocatalytic CO_2 reduction across various photocatalysts, thereby serving as valuable guidance for the advancement of high-performance photocatalysts.

1 Introduction

Excessive carbon dioxide emissions from the use of fossil fuels have significantly affected the climate, resulting in global warming.[1] According to the “Global Carbon Budget 2023” report, it is estimated that the worldwide emissions of carbon dioxide will reach an unprecedented level of 36.8 billion tons in 2023, witnessing a 1.1% increase from the previous year. This not only underscores the inevitable depletion of humanity's predominant energy source—fossil fuels—but also highlights excessive CO_2 emissions resulting from their combustion.[2–6] Therefore, it is imperative for experts to devise viable strategies to convert vast quantities of renewable energy sources such as solar energy, which can potentially supply the earth with approximately 120 000 TW of power annually, into usable chemical energy.[7–11] Possible chemical transformation pathways for CO_2 reduction include enzymatic catalysis, electrocatalysis, chemical reforming, and photocatalysis (Scheme 1). In the case of enzymatic catalysis, it is easy to achieve C–C

State Key Lab of Photocatalysis on Energy and Environment, College of Chemistry, Fuzhou University, Fuzhou, P. R. China. E-mail: z.zhang@fzu.edu.cn

Chen Fu

Chen Fu received her BS from Hanjiang Normal University in 2018. She is currently pursuing her master's degree at Fuzhou University under the supervision of Prof. Zizhong Zhang. Her research focuses on photocatalytic CO_2 reduction.

Zhenyu Wan

Zhenyu Wan received his BS degree from Qilu University of Technology (Shandong Academy of Sciences) in 2018. He is currently pursuing his master's degree at Fuzhou University under the supervision of Prof. Zizhong Zhang. His research focuses on the photocatalytic oxidation coupling of methane.

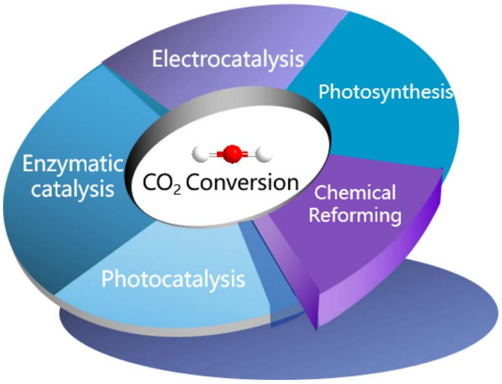

Scheme 1 Possible pathways for the chemical conversion of CO_2.

coupling, which can convert CO_2 into complex chemicals with high added value under mild conditions. However, a variety of problems such as the uncertain enzyme structure, poor stability, low activity, expensive cofactors, sensitivity to oxygen, and difficulty in purification are obstacles to large-scale greenhouse gas fixation.[12] Regarding electrocatalytic CO_2 conversion, its reaction conditions are relatively mild, reaction rate is controllable, and selective generation of target products can be controlled by adjusting reaction potential as well as electrolyte and catalyst type reasonably. However, the activity and stability of electrocatalysis are still low at industrial current density. In addition, owing to the amplification effect caused by complex multi-field coupling such as electric field, flow field and thermal field, reaction performance, such as reaction life and energy consumption, is reduced, which further limits the large-scale application of CO_2 electrolysis technology.[13] In the chemical reforming reaction of CO_2, the formed products are rich in variety and have heat resistance due to the carbonization reaction. However, if the chemical reforming reaction occurs in the absence of steam, traditional reforming catalysts will be rapidly deactivated.[14] To date, there are no effective commercial catalysts that can operate without producing carbon; meanwhile, the chemical reforming process is an energy-intensive process that does not meet the requirements of green sustainability. Accordingly, the photocatalytic reduction of CO_2 to useful chemicals by simulating natural photosynthesis is the most ideal way. Compared with other methods, the photocatalysis process is carried out at room temperature and pressure, the raw materials are simple and easy to obtain, and the direct use of solar energy does not require auxiliary energy and can truly realize the recycling of carbon materials; thus, it is considered to be the most promising CO_2 conversion method.[15–19] Not only does it tackle the issue of excessive carbon dioxide emissions, but it also addresses the escalating need for energy.

Photocatalytic CO_2 reduction has been extensively explored in terms of photocatalyst materials, product yield and selectivity, and mechanism.[20,21] Consequently, substantial progress has been made in enhancing the efficiency and product selectivity through diverse catalyst development strategies. Researchers have explored various strategies for the modification of catalysts aimed at improving their catalytic efficiency. Generally, there are two main concerns in the development of photocatalysts. Firstly, it is necessary to improve the separation and transfer of photogenerated charge in the photocatalyst *via* the typically heterojunction composition or cocatalyst loading. For instance, Cheng *et al.*[22] developed an ultra-thin Z-type heterojunction with a double-defect structure to enhance the efficiency of charge separation. Ran *et al.*[23] proposed that the presence of a co-catalyst can enhance the separation and

Xin Yang

Xin Yang received her BS degree from Anhui University of Science and Technology in China in 2017, and later, she obtained her MS degree at Fuzhou University in 2021. Her research focuses on photocatalytic CO_2 reduction.

Junhui Zhang

Junhui Zhang received his BS degree from Nanchang Hangkong University in China in 2017, and later, he obtained his MS degree at Fuzhou University in 2021. His research focuses on photocatalytic CO_2 reduction.

Zizhong Zhang

Zizhong Zhang is Full Professor in the State Key Laboratory of Photocatalysis on Energy and Environment at Fuzhou University. He received his PhD in physical chemistry at Fuzhou University. His research interests mainly focus on heterogeneous photocatalysis in water splitting, CO_2 conversion, CH_4 transformation, and environmental purification.

transfer of photoinduced electron–hole pairs and provided an overview of the co-catalysts developed to date. Secondly, it is necessary to enhance the CO_2 absorption and activation on photocatalysts *via* single atom or defect engineering. Zhang *et al.*[24] proposed that anchoring Cu single atoms in COFs can provide more adsorption and activation sites for CO_2 molecules, showing excellent photocatalytic activity for reducing CO_2. Huo *et al.*[25] synthesized surface amine-functionalized SnO_2 with oxygen vacancies, where the defects served as CO sites, enhancing the CO_2 adsorption capacity, and the presence of surface vacancies altered the local electron density distribution, facilitating electron injection into the π antibonding orbitals of CO_2, thus effectively activating the CO_2 molecules. However, the total efficiency of photocatalytic CO_2 reduction is far from satisfactory to date. Thus, the development of efficient photocatalysts is crucial to promote the CO_2 reduction efficiency in photocatalytic systems.

The focus on photocatalyst performance in CO_2 reduction is accompanied with significant interest in the selectivity for the resulting products. Various products (such as CO, HCOOH, CH_3OH, CH_4, C_2, and C_{2+}) can result from this photocatalytic process.[26,27] Due to the complexity of the photocatalytic process, controlling the selectivity for the reduction products is very challenging.[28–31] Thus, it is necessary to understand the factors in the reaction to affect the product selectivity for efficient catalyst design. Both thermodynamic and kinetic aspects, including the energy levels of the conduction band and valence band of the photocatalyst,[32,33] reduction potential for CO_2 to the products, CO_2 adsorption and activation, intermediate adsorption/desorption,[34,35] lifetime and concentration of photogenerated electrons,[36,37] and competing reactions,[38] are the key influencing factors when considering the product selectivity.[39,40] Wang *et al.*[41] found that Ag could inhibit the H_2O reduction reaction on a TiO_2 shell, demonstrating the effect of competitive reaction on the product selectivity. It was discovered by Wang *et al.*[42] that the energy band configuration of TiO_2 can be optimized through the incorporation of cobalt, ultimately influencing the selectivity for the CO_2 photolysis end-products. Xie *et al.*[35] revealed that alkaline earth metal oxides possessed a higher aptitude for CO_2 absorption and activation, subsequently altering the reaction pathway and product selectivity in photocatalytic CO_2 reduction. In addition, strong and weak adsorption between the intermediates and photocatalysts will also affect the selectivity of photocatalytic CO_2 reduction. When the interaction between the intermediates and photocatalyst is weak, their desorption and release from the surface of the photocatalyst will be easier, and these substances will become important by-products. Zhang *et al.*[43] found through theoretical calculation that changing the adsorption pattern of the intermediate CO can improve its product selectivity. Wang *et al.*[44] summarized the possible reaction mechanism of photocatalytic CO_2 conversion to produce C_1 and C_2 products. Four principal mechanisms were outlined for the generation of these products on the surface of TiO_2, including the formaldehyde route, carbene route, glyoxal pathway, and formyl route. Therefore, gaining a holistic comprehension of these distinct reaction mechanisms can facilitate the development of photocatalysts with improved activity and selectivity for CO_2 photoreduction.

This review comprehensively examines the advancements in photocatalyst optimization strategies aimed at enhancing the charge separation in photosynthesis and boosting the CO_2 conversion process. The connection between the architectural design and the efficiency of photocatalysts and selectivity for CO_2 photocatalytic reduction is analysed. Moreover, we outline the impending prospects and obstacles in photocatalyst design, particularly in augmenting the selectivity of CO_2 reduction towards specific products. Serving as a synopsis of yield and selectivity across various photocatalysts for CO_2 reduction, this review is intended to stimulate the advancement of high-performance photocatalysts for this purpose.

2 Principle of photocatalytic reduction of CO_2

Photocatalytic CO_2 reduction with the H_2O reaction process is complex and involves multiple reaction steps.[45,46] The use of light as the excitation energy to trigger CO_2 reduction and H_2O oxidation reactions on semiconductors can be separated into the following steps (Fig. 1):[47–51] (1) adsorption activation of CO_2 molecules. The first key step in photocatalysis involves the absorption of CO_2 on the active sites on the catalyst surface. Adsorption interactions produce partially charged $CO_2^{\delta-}$, and different binding modes of $CO_2^{\delta-}$ will produce different intermediates, which will influence the reaction trajectory to some extent, thus changing the product selectivity. (2) Upon the absorption of light, electron–hole pairs are generated. When the energy of the absorbed light exceeds the bandgap energy (E_g) of the catalyst, it results in an abundance of photoexcited electrons and holes. These charge carriers migrate towards the catalyst surface, where they engage in redox processes. To ensure that photocatalysts can reduce CO_2 and oxidize H_2O, semiconductors are required to have appropriate valence and conduction band positions.[39,52–54] The conductive band minimum should lie at a potential lower than that required for CO_2 reduction, whereas the maximum points of the valence band should reside at a potential surpassing the level needed for water oxidation.

(3) Efficient charge carrier mobility and separation are crucial. Given that electron–hole pair recombination occurs significantly faster than charge transport and depletion, the lifespan of photoexcited electrons must be sufficiently

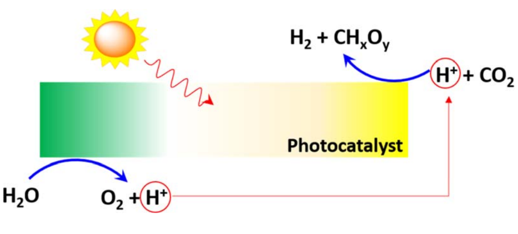

Fig. 1 Basic steps of photocatalytic conversion of CO_2 and H_2O on semiconductors.

prolonged to facilitate photocatalytic redox reactions. The efficient separation of photogenerated electrons–holes improves the density of surface photogenerated electrons, which is beneficial for accelerating the redox reaction and promoting the generation of hydrocarbons.[55–60] (4) The photogenerated electrons on the surface active sites undergo a reduction reaction with CO_2 to produce hydrocarbons, while the photo-generated holes undergo an oxidation reaction with H_2O to produce oxidation products such as O_2 and $^{\bullet}OH$. This is a key step in photocatalytic CO_2 reduction. (5) The reaction products are desorbed from the surface of the photocatalyst, and the newly generated surface active sites participate in the next catalytic reaction.[61–64] To design an efficient photocatalyst for CO_2 conversion, the above-mentioned conditions must be satisfied simultaneously.

In terms of thermodynamics, the fundamental determinant of the efficiency in photocatalytic reactions is the semiconductor band structure. The relative position of the semiconductor conduction and valence bands determines the oxidation-reduction ability.[65–67] In the context of photocatalytic conversion of CO_2, it is essential that the conduction band (CB) of the photocatalysts possess a chemical potential that is notably more negative compared to the reduction potential of CO_2. Conversely, for the process of water oxidation, the valence band (VB) must have a positive potential exceeding the energy level required for water oxidation. Fig. 2 shows the bandgap, conduction band and valence band positions of some common semiconductor catalysts. The potential in Fig. 2 refers to a normal hydrogen electrode (NHE) reference with $pH = 7$ in an aqueous solution. According to different reaction mechanisms and pathways, CH_4, CH_3OH, CO, HCOOH, C_2H_6, C_2H_5OH, and even $H_2C_2O_4$ are all possible products of CO_2 reduction. Although CO has a high reduction potential, it is easier to produce than CH_4, HCHO and CH_3OH due to the fact that its formation only requires two electrons. Usually, when selecting a catalyst for CO_2 reduction, the reduction potential of CO_2 to the required products need to be more positive than the conduction band edge potential of the selected semiconductor.

The thermodynamic characteristics of photocatalytic CO_2 reduction significantly influence both the feasibility of the photocatalytic process and the ultimate reduction products. Alternatively, the kinetic aspects of this reduction govern the pace of the reaction in terms of rate and product formation. The detailed analysis of the photocatalytic kinetics is complex given that it involves many processes,[68–71] including the photogeneration and separation of holes and electrons and the adsorption and activation of the reactant molecules.

(1) Separation of photogenerated electron–hole pairs. In photocatalytic reactions, the recombination lifetime of the photogenerated electrons–holes is very fast, usually only a few picoseconds, exceeding their transport rate from the bulk phase to the surface layer (which takes hundreds of picoseconds). Simultaneously, the recombination rate of charge carriers on the catalyst surface is relatively rapid, occurring within tens of picoseconds, much faster than the speed at which they participate in catalytic reactions (ranging from a few nanoseconds to a few milliseconds).[72–77] The swift combination of electrons and holes significantly diminishes the photocatalytic performance. The poor quantum efficiency observed in numerous photocatalysts is attributed to the premature recombination of these charge carriers before engaging with the adsorbed substances. Thus, enhancing the separation of charge carriers or inhibiting their recombination is pivotal to enhancing CO_2 reduction reactions. Furthermore, the accelerated migration of photogenerated charge carriers towards the semiconductor catalyst surface contributes to elevating the rate of the multi-electron CO_2 reduction process, thereby enhancing the yield of the end products and the photocatalytic kinetics.[54,78–81]

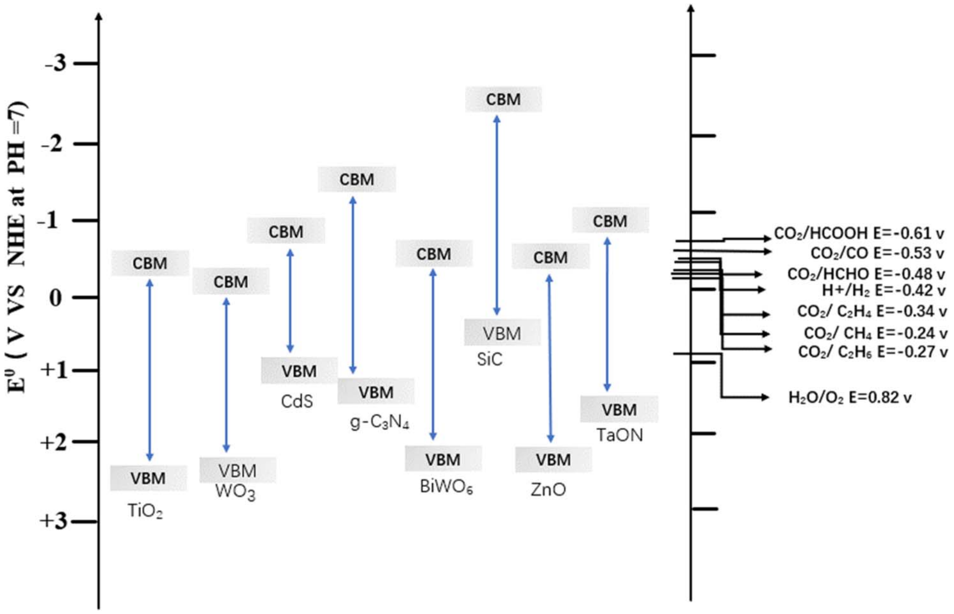

Fig. 2 Schematic of the band gap, conduction band and valence band positions of common semiconductor catalysts.

(2) Adsorption and activation of reactant molecules. The CO_2 molecule is highly inert. In the CO_2 molecule, the carbon atom forms a chemical bond with the oxygen atoms through sp hybrid orbitals, influencing the reaction selectivity within the pair of carbon atom sp hybrid orbitals combined to create two σ bonds with the orbitals from two oxygen atoms, respectively. The other two p orbitals on the carbon atom, which are not involved in hybridization, overlap shoulder-to-shoulder with the p orbitals of the oxygen atom and form two delocalized bonds with three centres and four electrons.[5,17,29,82] This structure shortens the distance between the C–O atoms and endows CO_2 molecules with certain triple bond characteristics. Hence, the C–O bond dissociation necessitates a significant energy input, making the thermodynamic activation of CO_2 molecules arduous. The key kinetic aspects for the initiation of CO_2 reduction are the absorption and activation of CO_2 molecules on the catalyst surface. In photocatalytic reduction processes, CO_2 molecule activation demands its adsorption on the catalyst surface, followed by a structural transition from a linear to bent configuration. This is followed by the transfer of electrons from the photocatalyst surface to the distorted CO_2 molecules, thus facilitating CO_2 activation.[83–86]

Consequently, the engagement of CO_2 with the catalyst surface plays a crucial role in its absorption, effectively stimulating CO_2 molecules. During the photocatalytic conversion of CO_2, the adsorption of CO_2 onto the photocatalyst surface primarily involves three types of adsorption modes including oxygen coordination, carbon coordination, and mixed coordination (Fig. 3). In this mechanism, the interplay between CO_2 and surface atoms generates partially charged $CO_2^{\delta-}$ species. The production of the characteristic activation intermediates is decisive for the reaction route, which influences the selectivity for diverse products.[29,39] Furthermore, the dynamic characteristics of the multistage surface catalytic reaction in photolytic CO_2 conversion reveal that the catalytically active sites on the surface of a photocatalyst play a role in determining the product selectivity. Consequently, diverse active sites on the catalyst surface can give rise to distinct products.[68,87–90] For example, the monodentate binding of C atoms with Lewis bases forms carboxyl radicals ($^{\bullet}$COOH) centred on the catalyst, while the bidentate binding of two O atoms tends to favour H to link the carbon of $CO_2^{\delta-}$, which causes formate anions to bind in a bidentate manner on the catalyst surface.

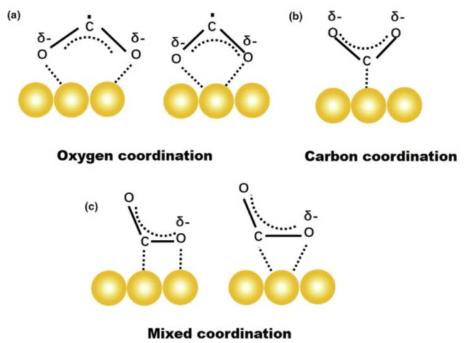

Fig. 3 Three different CO_2 adsorption modes on the photocatalyst surface: (a) oxygen coordination; (b) carbon coordination; (c) mixed coordination. Reproduced from ref. 29 with permission from [the Royal Society of Chemistry], copyright [2016].

Activated CO_2 molecules engage in a reaction with electrons that have been photo-induced and displaced towards the catalytic centre. To enhance the adsorption and activation of CO_2, photocatalysts with large surface areas or surface alkaline groups are usually used in the preparation of catalysts to provide more active sites.[91–93] The strategies employed include introducing defect vacancies,[94–96] introducing cocatalysts,[97–101] increasing the specific surface area and porosity of the catalyst,[102,103] and adjusting the acidity and alkalinity of the catalyst surface.[104,105]

In the photocatalytic process, the thermodynamics and kinetics are intertwined in the reaction, jointly determining the reaction efficiency and products. Thus, to improve the photocatalytic efficiency, it is necessary to comprehensively consider these two factors, optimizing the band structure, surface chemical properties, reaction conditions and photocatalytic system.[106–108]

Thus far, many reaction mechanisms for photocatalytic CO_2 reduction have been proposed.[109,110] The main three pathways of formaldehyde, carbene and glyoxal pathways are shown in Fig. 4. In the formaldehyde pathway, CO_2 initially undergoes electron excitation to form $CO_2^{\cdot}$. Subsequently, this species combines with a proton to yield a formic acid intermediate. This intermediate accepts additional protons to produce formic acid. Furthermore, through processes of electron coupling and proton transfer, formic acid serves as a foundation for the production of formaldehyde, methanol, and methane. This pathway can be used to explain the formation of HCOOH, HCHO and CH_4, but the production of CO cannot be explained.[111–114] In the carbene pathway, the production of CO can be explained. Activated CO_2 accepts electrons to produce CO, and CO can be used as an intermediate product for the further formation of methane or methanol. C–C bond formation depends on the stabilization of the intermediary radical to prevent its recombination with the above-mentioned hydrogen atoms. In contrast, the glyoxal pathway predominantly yields C_2 compounds, where $CO_2^{\cdot}$ combines with electrons and protons to form formic acid, resulting in free formyl radicals (CHO$^{\bullet}$) due to oxygen transfer and further electron acceptance. Eventually, the formyl groups are dimerized into glycol or evolve into other C_2 and C_3 products. The photocatalytic conversion of CO_2 involves multiple steps, intermediates, and diverse end-products, making the process of product selectivity more complicated.[54,114–116] Currently, CO_2 conversion to C_{2+} products *via* the C–C coupling process mainly include the following reaction pathways: (a) $^*CH_3$ coupling, (b) *CO hydrogenation to *CHO and further coupling of *CO and *CHO, (c) *CHO dimerization, and (d) *CO linkage to *COCO and a series of oxygen-binding intermediates,[117] where the dimerization of the C_1 intermediates on the catalyst surface to form C–C bonds is the key to the further formation of C_2 products (Fig. 5). For example, the pathway to produce ethylene or ethane involves the coupling of carbene intermediates (CH_2 and CH_3) in the carbene pathway, while the dimerization of formyl groups

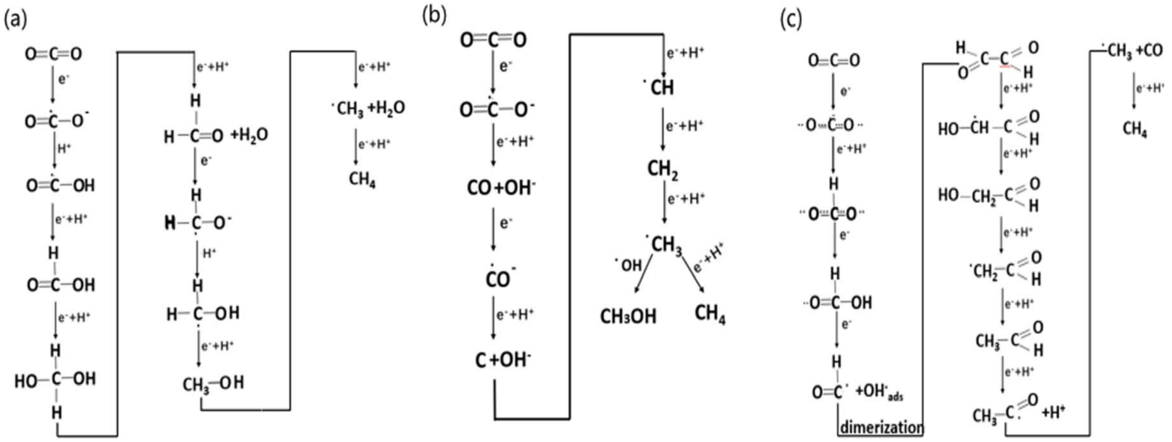

Fig. 4 Three possible paths for carbon dioxide reduction: (a) formaldehyde pathway, (b) carbene pathway and (c) glyoxal pathway.

(CHO) in the glyoxal pathway can produce multiple C_1 and C_2 products. Given that the C_2 product involves multi-electron-coupled proton transfer and C–C coupling processes, the reactions are often more challenging. The dehydration step after CO_2 receives 3 protons, forming the formyl radical (HC*O). Subsequently, the formyl radical dimerizes to form glyoxal, which is reduced to the ethylene oxy ($*CH_2$–CHO) radical. This is further converted to acetaldehyde (CH_3CHO) or C_2H_5OH, and the production of C_2H_4 can be caused by CO dimerization, which has several steps similar to the glyoxal pathway, except that the intermediate (CH_2CHO) changes from C-coordination to O-coordination.[44,118–120] To attain precise control of these products, the key aspects of the photocatalytic CO_2 reaction pathway can be manipulated, such as manipulating the energy band architecture, enhancing the charge separation efficacy, and optimizing the absorption and activation of reactants.[112–114]

3 Strategies to design photocatalysts

Numerous photocatalysts have been explored for the photocatalytic reduction of CO_2 into a value-added fuel, such as metal oxide (TiO_2, ZnO, Cu_2O, $InVO_4$, Bi_2WO_6, *etc.*), metal sulphide (CdS, Ag_2S, $ZnIn_2S_4$, *etc.*), carbon-based semiconductor (SiC, g-C_3N_4, graphene, *etc.*), MOFs, COFs and other materials.[17,23] Nonetheless, these catalysts are associated with numerous limitations, including inadequate sunlight absorption efficacy, rapid recombination of photoexcited electrons and holes, and lack of active sites on their surface. These problems eventually lead to unsatisfactory reaction efficiency and product selectivity.[55,56,121,122] Therefore, many modification strategies have been commonly used for the preparation of photocatalysts, such as cocatalyst loading, doping, defect engineering, heterojunction formation, single-atom engineering, and surface

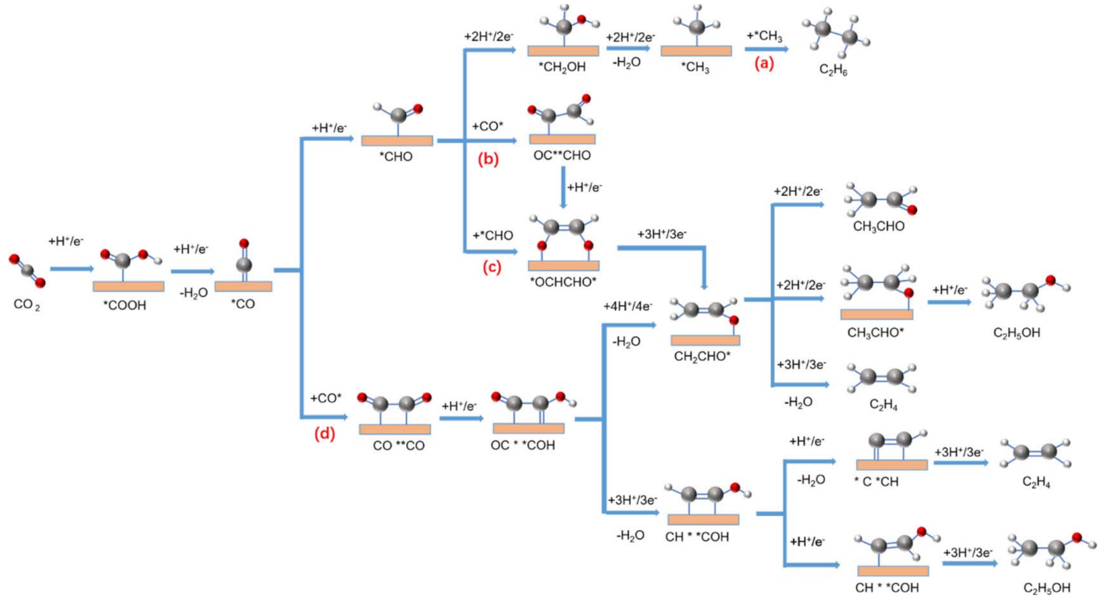

Fig. 5 Currently reported C–C coupling reaction pathways for photocatalyzed CO_2 conversion to C_{2+} products. Reproduced from ref. 117 with permission from [ACS Publications], copyright [2023].

Scheme 2 Summary of commonly used modification strategies for photocatalysts.

organometallic catalysis, as shown in Scheme 2. We attempted get inspiration from the relevant cases to provide some new insights for the design of new efficient photocatalysts.

3.1 Defect construction

The balanced coordination of charge generation and separation in photocatalysts is crucial in the photocatalytic process. It has been reported that structural defects in semiconductors can improve the mobility of carrier charges and extend their lifetime to maintain the reaction kinetics,[123] including 3D volume defects (voids and disorders).[124–126] Point defects are generated through the removal of atoms in the lattice or doping. Line defects are formed by the dislocation of atoms in the lattice. Planar defects refer to the arrangement of atoms on both sides of the crystal surface, which is characterized by the arrangement of atoms deviating from the equilibrium position in the two-dimensional direction.[25,95,96,127–129] Volume defects are caused by introducing a variety of substances into one or more crystal locations, resulting in lattice gaps or chaos. All types of defects affect the electronic structure and catalytic performance of metal oxides (MOs).[130,131]

Since Chen *et al.*[132] synthesized black TiO_2 in 2011, research has focused on oxygen vacancies (OVs). It has been reported that defects can change the surface properties to expose new active centres in MOs.[121,133] The presence of vacancies is favourable for photoinduced electrons to preferentially enter the vacancies on the catalyst surface, suppressing the recombination loss of photogenerated electron–hole pairs, facilitating charge transportation, and enhancing surface chemical reactions. In addition, the binding mode and adsorption strength of CO_2 on the surface of MOs are also related to the properties of the internal and external defects. OVs on the surface play key roles in adsorption and activation.[134] Liu[135] synthesized Cu(I)/TiO_{2-x} with surface OVs by annealing with an inert gas at 300 °C. The results showed that the catalyst with defects had a higher

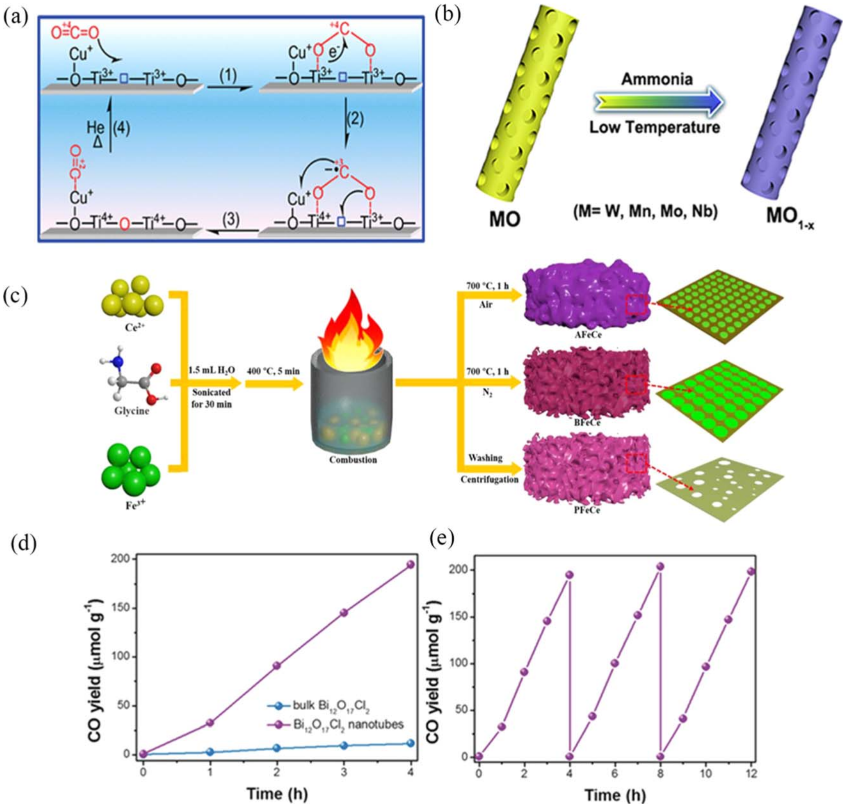

Fig. 6 (a) CO_2 adsorption mechanism diagram of TiO_2 with oxygen vacancies. (b) Low-temperature ammonium-assisted reduction of nitrogen-free doped WO_{3-x} nanorods. (c) Synthesis of CeO_2 rich in anionic defects. (d and e) Photocatalytic CO_2 reduction yield and stability of modified $Bi1_2O_{17}Cl_2$. (a) Reproduced from ref. 135 with permission from [ACS Publications], copyright [2012]. (b) Reproduced from ref. 136 with permission from [Cell], copyright [2012]. (c) Reproduced from ref. 137 with permission from [Elsevier], copyright [2022]. (d and e) Reproduced from ref. 138 with permission from [Wiley Online Library], copyright [2018].

CO yield than the catalyst without defects, which provided some active sites of Ti^{3+} for the adsorption of O atoms from CO_2 (Fig. 6a). Thus far, many effective methods have been developed to control the formation of vacancies, such as calcination, chemical reduction, ion doping and hydrothermal/solvothermal methods. High-temperature calcination is a process in which the sample is calcined at high temperature through an inert or reducing atmosphere to promote the diffusion and escape of surface lattice oxygen, and thus generate OVs. The vacancy concentration is affected by the calcination temperature and time. Generally, increasing the heating temperature and extending the calcination time can improve the vacancy concentration.[95,127,129,139] For example, Tan *et al.*[140] found that annealing $SrTiO_3$ at 375 °C had a higher OV concentration than annealing at 300 °C, and that extending the heating time by half an hour contributed to the formation of OVs. However, it tended to generate more OVs at a lower temperature under vacuum conditions.

Xing *et al.*[141] modified TiO_2 with a low-temperature vacuum activation method to obtain stable Ti^{3+} and OVs. This method can also be used to enhance the visible light response of ZnO, WO_3 and other oxides. It is worth noting that a higher vacancy concentration is not better. A too high OV concentration may introduce a new impurity band with an unlocalized molecular orbital, which can trap electrons excited from the valence band and prevent them from reaching the conduction band, thus inhibiting charge migration.[142]

In contrast to high-temperature calcination, chemical reduction can produce vacancies at low temperature. When the reducing molecules adsorb on the MO surface, electrons transfer to the surface to capture the O atoms, finally forming OVs.[136] For example, Liu *et al.*[136] synthesized WO_{3-x} nanorods *via* a low-temperature ammonium-assisted reduction method (Fig. 6b), showing an excellent photocatalytic performance in the reduction of CO_2 and H_2O to CH_4. Xu *et al.*[143] introduced OVs on the surface of $SrTiO_3$ by $NaBH_4$ treatment, and the vacancy led to the formation of intermediate gap states. Combined with the inherent energy level of $SrTiO_3$, the $SrTiO_{3-x}$ photocatalyst exhibited enhanced activity in the reduction of CO_2 to CO under visible light irradiation.

Ion doping can also create vacancies in photocatalysts. The different chemical valence ion dopants replace the metal nodes in the oxide substrate, thus destroying the lattice oxygen order, and OVs are generated to maintain the charge balance. The use of cationic defects is a common method to introduce vacancies in MOs by replacing the original cation with a lower cost state or one with a lower vacancy formation energy.[144] For example, Zhou *et al.*[145] doped Ru in TiO_2 nanocrystals by the hydrothermal method and induced the formation of OVs. Metal ions and OVs cooperated to promote the adsorption of CO_2 and the separation of photogenic carriers, thus achieving the photocatalytic conversion of CO_2 and H_2O into CH_4. Lai *et al.*[137] synthesized Fe-containing CeO_2 with an OV porous structure *via* a one-step combustion method (Fig. 6c). The porous structure was conducive to the adsorption of CO_2, and OVs promoted the activation of CO_2. In addition to the doping of cations, anion defects can be constructed on MOs by introducing anions such as N, P, S, and halogens. Zeng *et al.*[146] calcined $Co(NO_3)_2$ on an SBA-15 template and reintroduced fluorine to synthesize $Co_3O_{4-x}F_x$ with defective, fluorine substitution and three-dimensional mesoporous structure. The fluorine substitution and partial OVs altered the electronic structure to promote the ability to adsorb intermediates. This study proposed a new strategy of combining defects with fluorine chemistry, providing an idea for the design of defective fluoride oxides.

Hydrothermal/solvothermal reaction is a technique to synthesize crystalline materials by controlling the thermodynamic variables such as solvent type, additive composition, temperature and pressure, which can greatly control the morphology and structure, size and orientation of crystallinity. It is one of the best methods to prepare nanoscale materials.[147] Zhang *et al.*[148] synthesized Ti/TiO_2 interfacial photocatalysts with different concentrations of Ti^{3+} sites *via* a hydrothermal one-step method. It was found that the interfacial coordination of unsaturated defect sites can not only narrow the band gap, but also promote the transfer and separation of interfacial photogenerated vectors, thus effectively improving the photocatalytic activity.

In recent years, researchers have worked on developing bismuth oxide halide-based photocatalysts. OVs are easily introduced in BiOX nanotubes and thin nanosheets. Di *et al.*[138] constructed $Bi_{12}O_{17}Cl_2$ featuring a twin-layered ultrathin tubular architecture enriched with surface oxygen vacancies. Under the illumination of a 300 W xenon lamp, the CO production rate for this engineered catalyst averaged 16.8 times higher (48.6 μmol g^{-1} h^{-1}) than the pristine bulk $Bi_{12}O_{17}Cl_2$. Concurrently, it accomplished the conversion of H_2O to O_2, with an average O_2 yield of 23 μmol g^{-1} h^{-1}, sustaining its stability over 12 h of activity assessment (Fig. 6d and e). Wu *et al.*[149] prepared BiOBr lamellar precursors *via* the hydrothermal method, and then separated them into atomic layers by ultrasound in an ice water bath. Finally, a large number of OVs was introduced on the surface of the atomic layers after 8 h ultraviolet irradiation because BiOBr with a high oxygen atomic density exposed (001) surface easily formed OVs under the irradiation of high-energy light (Scheme 3). Owing to the augmented light absorption in the visible spectrum of the modified BiOBr atomic layers and the facilitation of CO_2 conversion into intermediary COOH* by the surrounding surface oxygen vacancies, the reduction rate witnessed a remarkable increase of 24 times compared to pristine BiOBr (yielding 87.4 μmol g^{-1} h^{-1}). These findings suggest that the introduction of defects on the catalyst surface can effectively optimize the CO_2 reduction mechanism, thereby paving the way

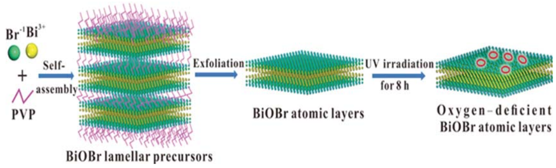

Scheme 3 Synthesis process of oxygen-deficient BiOBr photocatalysts. Reproduced from ref. 149 with permission from [Wiley Online Library], copyright [2018].

for innovative strategies in designing high-performance catalysts that operate under visible light for CO_2 reduction purposes.

In addition to oxygen vacancies, sulfur defects are very common in sulfide catalysts, and sulfur defects play an important role in photocatalytic CO_2 reduction by these catalysts. For instance, Yin *et al.*[150] created S vacancies in a thin layer of SnS_2 atoms through Ar plasma bombardment. It was found that the S vacancy could reduce the reactive energy barrier for water decomposition by constructing a specific reactive configuration. This led to a direct enhancement in water oxidation during the entire process of photocatalytic CO_2 reduction by promoting the formation of O_2 molecules. Ultimately, a substantial improvement in the performance for the photoreduction of CO_2 was achieved. The photocatalytic CO_2 reduction process exhibited a CO yield of 25.71 μmol g^{-1} h^{-1}, which was 8.2 times higher than that of the initial SnS_2 catalyst. Gao *et al.*[151] proposed the introduction of sulfur defects in an atomic layer of $AgInP_2S_6$ using an H_2O_2 etching method. Through DFT calculation and *in situ* FTIR spectroscopy, it was demonstrated that introducing a sulfur vacancy in $AgInP_2S_6$ can accumulate charge on the Ag atoms near the sulfur vacancy, allowing the exposed Ag site to effectively capture formed *CO molecules. This enrichment in key reaction intermediates on the catalyst surface reduced the C–C binding coupling barriers and promoted ethylene production with a yield selectivity of up to 73%.

3.2 Cocatalyst loading

The integration of a metal co-catalyst in a photocatalyst significantly contributes to the augmentation of its photocatalytic performance. In certain instances, the addition of a co-catalyst not only boosts the efficiency of the photocatalytic reaction but also efficaciously influences the selectivity for the resulting products. The dispersion of the cocatalyst should be controlled reasonably during the catalytic process. Excess or slight amounts of active sites are not conducive to the reaction.[97–101] Adrian Quindimil *et al.*[152] prepared Ni/Al_2O_3 and Ru/Al_2O_3 catalysts with different metal loadings. The loading of Ni and Ru provided new alkaline sites to promote the adsorption of CO_2, and the noble metal Ru on Al_2O_3 was more efficient in dissociating H_2 than the non-noble metal Ni. The conversion rate of CO_2 was the highest when the loading of Ni was 12% and the loading of Ru was 4%. In addition, the presence of H_2 adsorption/dissociation points is important for the methanation of CO_2, but pure MOs usually lack H_2 dissociation points. Thus, to solve this problem, Dreyer *et al.*[153] used flame spray pyrolysis to disperse 5% Ru on Al_2O_3, ZnO, MnO_x, and CeO_2, and found that the supported Ru nanoparticles could provide H_2 dissociation points, thus significantly improving the yield and selectivity for CH_4.

The n-type semiconductor TiO_2 is one of the most commonly used photocatalysts because of its advantages such as low price, non-toxic nature, and resistance to photocorrosion.[154] Dating back to 1978, Kraeutler and Bard first loaded Pt on TiO_2 for CO_2 reduction *via* photodeposition.[155] Subsequently, many teams were inspired to prove that the selectivity of CH_4 would be improved after loading the noble metal Pt on TiO_2. They believed that the selective conversion of the CO product to CH_4 was because the Pt loaded on the photocatalyst surface formed a Schottky junction, which could extend the photoelectron lifetime, thus lowering the reaction barrier and promoting the formation of CH_4.[156–158] Thus, to explore the reason for the selective transformation of CO_2 reduction after Pt loading, Ma *et al.*[159] loaded 1 wt% Pt on TiO_2, g-C_3N_4 and BiOBr, respectively, by photodeposition, and found that the selectivity of the three photocatalysts for CH_4 increased to nearly 100% (Fig. 7a). The gas adsorption energy and charge transfer amount for CO_2, CO, and CH_4 of Pt clusters with two configurations were calculated (Fig. 7b), and the results were attributed to the following reasons: (1) CO has strong adsorption capacity on Pt, and thus its desorption from the catalyst surface is difficult, preventing the detection of CO. (2) CO is used as an intermediate, and CO enriched on the Pt clusters is more conducive to obtaining electrons to form CH_4. However, the adsorption capacity of CH_4 on Pt is very weak, which is manifested as physical adsorption and easy desorption. Therefore, the yield and selectivity for CH_4 were improved after Pt loading. This study provided further insight into how Pt promotes the highly selective production of CH_4 from photocatalyzed CO_2, as well as a new strategy for exploring photocatalyzed CO_2 reduction to CH_4. Xiong[158] deposited Pt and Cu_2O nanoparticles together on the surface of anatase TiO_2 *via* $NaBH_4$ reduction. Compared with the experimental results for Pt or Cu_2O loaded on TiO_2, it was found that Pt promoted the formation of CH_4 and H_2, whereas Cu_2O augmented CO_2 absorption on the TiO_2 surface. It concurrently suppressed the chemical adsorption of H_2O, subsequently hindering H_2 production. The combined effect of Pt and Cu_2O facilitated the exceptionally selective conversion of CO_2 into CH_4, offering insights into the development of multifaceted photocatalysts (Fig. 7c). H_2 competition in the process of CO_2 and H_2O photocatalysis is unfavourable for CO_2 reduction, and thus the cocatalyst should be selected to enhance CO_2 adsorption and weaken H_2O adsorption simultaneously.

The modification strategy of loading metals on TiO_2 alone has been widely reported. The electronic structure and geometric configuration of two metal alloy catalysts will be changed due to their combination, making the chemical interaction between the reaction intermediates and catalyst surface different. It can not only effectively reduce the kinetic overpotential but also control the product selectivity.[161] Neaţu *et al.*[160] deposited Cu and Au nanoparticles on TiO_2 for two consecutive times and found that CO_2 was reduced to CH_4 in H_2O under visible light irradiation. On the contrary, CH_4 was not detected under ultraviolet light irradiation, but H_2 production increased significantly. The charges on TiO_2 were directly separated and electrons migrated to the alloy nanoparticles under ultraviolet irradiation. At this time, the Au–Cu alloy stored electrons and acted as a co-catalyst. Both the bare TiO_2 and Cu/TiO_2 were inactive under visible light irradiation, while Au nanoparticles acted as a light collector due to their plasma effect. During the reaction, electrons from Au were transferred to the oxidized Cu surface, and the Au atoms activated by plasma successfully were reduced.[162] The main active

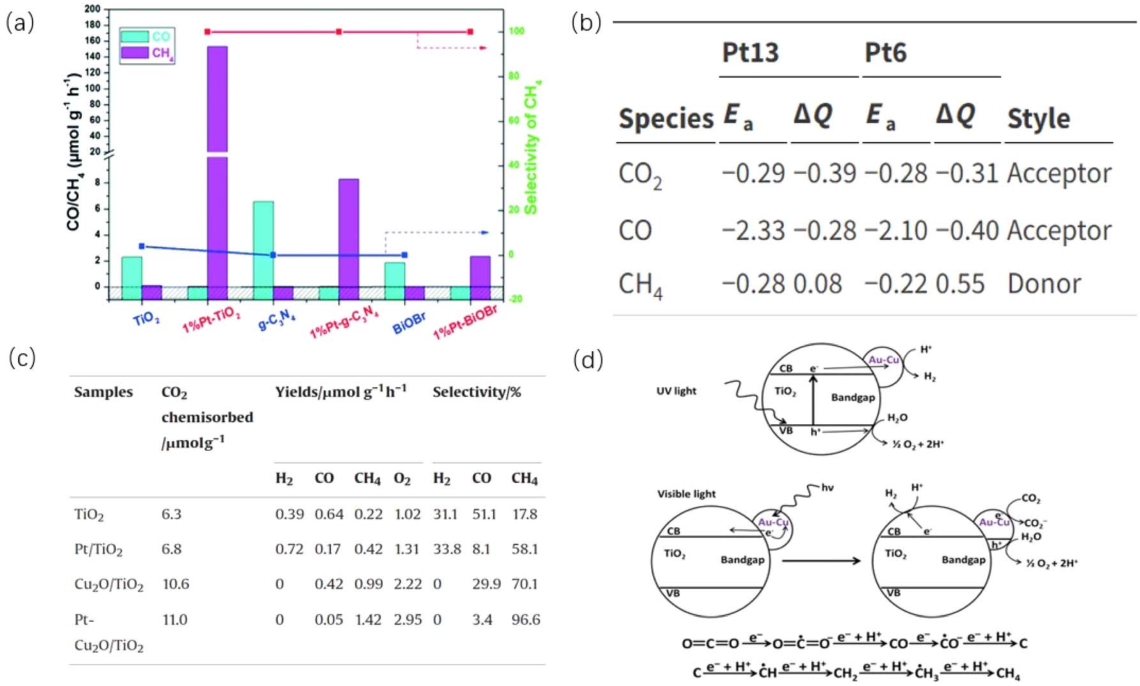

(b)

	Pt13		Pt6		
Species	E_a	ΔQ	E_a	ΔQ	Style
CO_2	−0.29	−0.39	−0.28	−0.31	Acceptor
CO	−2.33	−0.28	−2.10	−0.40	Acceptor
CH_4	−0.28	0.08	−0.22	0.55	Donor

(c)

Samples	CO_2 chemisorbed /μmolg^{-1}	Yields/μmol g^{-1}h^{-1}				Selectivity/%		
		H_2	CO	CH_4	O_2	H_2	CO	CH_4
TiO_2	6.3	0.39	0.64	0.22	1.02	31.1	51.1	17.8
Pt/TiO_2	6.8	0.72	0.17	0.42	1.31	33.8	8.1	58.1
Cu_2O/TiO_2	10.6	0	0.42	0.99	2.22	0	29.9	70.1
Pt-Cu_2O/TiO_2	11.0	0	0.05	1.42	2.95	0	3.4	96.6

Fig. 7 (a) Product selectivity of three photocatalysts: Pt/TiO_2, Pt/g-C_3N_4 and Pt/BiOBr. (b) Gas adsorption energy and charge transfer of CO_2, CO and CH_4 by two Pt clusters in the three photocatalysts. (c) CO_2 reduction yield and selectivity of TiO_2, Pt/TiO_2, Cu_2O/TiO_2 photocatalysis. (d) Schematic of the effect of different excitation wavelengths on the selectivity of TiO_2 products. (a and b) Reproduced from ref. 159 with permission from [the Royal Society of Chemistry], copyright [2018]. (c) Reproduced from ref. 158 with permission from [Elsevier], copyright [2017]. (d) Reproduced from ref. 160 with permission from [ACS Publications], copyright [2014].

sites of CO_2 existed on the surface of the reduced Cu atoms. The activation of CO_2 by a single electron followed the so called "carbine pathway" to produce CH_4, and the excess holes were used to oxidize H_2O to produce O_2 (Fig. 7d).

Enhancing the absorption and activation of CO_2 plays a pivotal role in boosting the efficiency of CO_2 reduction. Research indicates that the process of CO_2 adsorption and activation can be significantly augmented by augmenting the specific surface area of the catalyst[163,164] and multiplying the available sites for CO_2 adsorption.[165–167] Therefore, for some photocatalytic semiconductors without CO_2 adsorption and activation sites, it is necessary to fix the cocatalyst on the catalyst through doping or loading to construct active sites. Thus far, doping and loading synergistic strategies have also been widely used to improve the photocatalytic CO_2 reduction performance. Wang *et al.*[168] modified Ga_2O_3 by Zn species through impregnation and calcination to produce $ZnGa_2O_4$, and then supported a certain amount of Ag catalyst on $ZnGa_2O_4$ surface by photodeposition, and the production of the products was improved by regulating the addition amount of Zn and the loading amount of Ag. It was found that the H_2 production decreased continuously when the additive amount of Zn was in the range of 0.1 mol% to 10 mol%, while the production of CO was almost unchanged, and thus the selectivity for the CO product reached nearly 100%. In addition, Huang *et al.*[169] synthesized a Pt/CoO_x/N-TiO_2 composite photocatalyst, which was inspired by loading suitable double cocatalysts on the same catalyst. The synthesis process is shown in Scheme 4. Firstly, the layered titanite protonated precursor was prepared *via* the solvothermal method, and then the precursor was calcined for 2 h at 450 °C in an air atmosphere to obtain N-doped TiO_2 layered mesoporous spheres. The N-doping process was conducive to the introduction of OVs on the surface of TiO_2. Then, $Co(CH_3COO)_2 \cdot 4H_2O$ was used as a Co source to support CoO_x on N-doped TiO_2 *via* the *in situ* growth method. CoO_x was used as an oxidation cocatalyst for H_2O oxidation. Finally, H_2PtCl_6 was successfully reduced to Pt by photodeposition. The Pt loaded on the surface VOs of TiO_2 could capture and activate CO_2 as a reduction cocatalyst. Due to the synergistic action of VOs on the TiO_2 surface and the double cocatalyst, the yield of CO_2 conversion to CH_4 was further increased to 409.17 μmol g^{-1}. In this study, the efficiency of photocatalytic CO_2 reduction and H_2O oxidation was improved by introducing OVs to selectively deposit two cocatalysts on the surface of semiconductor materials to achieve dual active sites. However, it is worth noting that although the assumption that the entire REDOX reaction is separated into two half-reactions is conducive to the development of research, the distribution of cocatalysts on the semiconductor surface is random and uncontrollable, and there are still problems such as low yield, instability, and selectivity hurdles with co-catalysts such as sulphides. Hence, gaining profound insights into the photoexcited electron–hole transportation dynamics at the interface of co-catalyst/photocatalyst composites holds paramount importance for optimizing the cocatalyst design to enhance CO_2 photocatalysis. Advanced characterization techniques can facilitate the visualization of

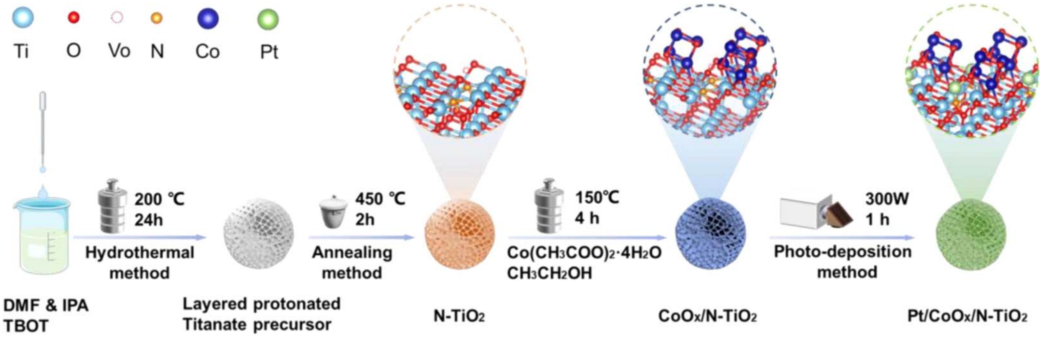

Scheme 4 Process for the synthesis of composite photocatalytic materials with Pt atoms and CoO_x dual co-catalysts. Reproduced from ref. 169 with permission from [Elsevier], copyright [2022].

electron–hole transfer, reaction intermediates, and end-products, thereby elucidating the intricacies of the reaction mechanism.

3.3 Doping

Doping different elements in a catalyst is one of the common strategies to optimize its catalytic performance, which can be divided into non-metallic doping, metal doping, and co-doping according to the type of doping elements. Graphitic carbon nitride ($g\text{-}C_3N_4$), a typical representative of carbon-based materials, has emerged as one of the highly desirable photocatalysts, owing to its responsiveness to visible light, stable physical and chemical properties, convenient preparation, and other advantages. Furthermore, the bandgap of $g\text{-}C_3N_4$ is approximately 2.7 eV, with its conduction band situated at around −1.1 eV. This negatively positioned conduction band is notably lower than the reduction potential required for converting CO_2 into CO, CH_4, CH_3OH, and various other fuel molecules.[170–176]

Regrettably, the light absorption capacity and surface area achieved through the conventional calcination of $g\text{-}C_3N_4$ remain inadequate, and the swift recombination of photoexcited electrons and holes significantly hampers the catalytic efficiency of bulk $g\text{-}C_3N_4$. Thus, researchers suggested the incorporation of distinct components into $g\text{-}C_3N_4$ to modify its crystal and electronic configuration, thereby manipulating its bandgap size, enhancing its absorption in the visible light spectrum, augmenting its specific surface area, and boosting its charge separation effectiveness.

$g\text{-}C_3N_4$ is a type of non-metallic semiconductor. If non-metals are added to it, then it can continue to maintain its non-metallic properties, such as high ionization energy and electronegativity.[177] The common non-metallic doping elements include B, P, S, O, and halogens. During the doping process, these elements easily acquire electrons to form covalent bonds with other compounds. The doping of $g\text{-}C_3N_4$ is divided into interstitial doping and substitution doping based on the distance between and within the plane of the principal lattice planes and the atomic radius of the dopant.[178] Substitution doping usually forms a more stable structure than interstitial doping.[179–181] Its dopant atoms displace the atoms in the main lattice and form chemical bonds with the surrounding atoms. For example, S atoms and N atoms have a similar atomic radius, and thus S atoms can easily replace N atoms, and eventually form an S–C bond in $g\text{-}C_3N_4$.[180] Arumugam *et al.*[182] reported the comparative effect of the incorporation of non-metals B, O, P and S into $g\text{-}C_3N_4$ for the photocatalytic reduction of CO_2 to CH_4 with H_2O. The synthesis process of the catalyst is demonstrated in Scheme 5. Sodium dihydrogen phosphate was used as the P source, boric acid as the B source, thioureone as the S source, and hydrogen peroxide as the O source. Upon thorough

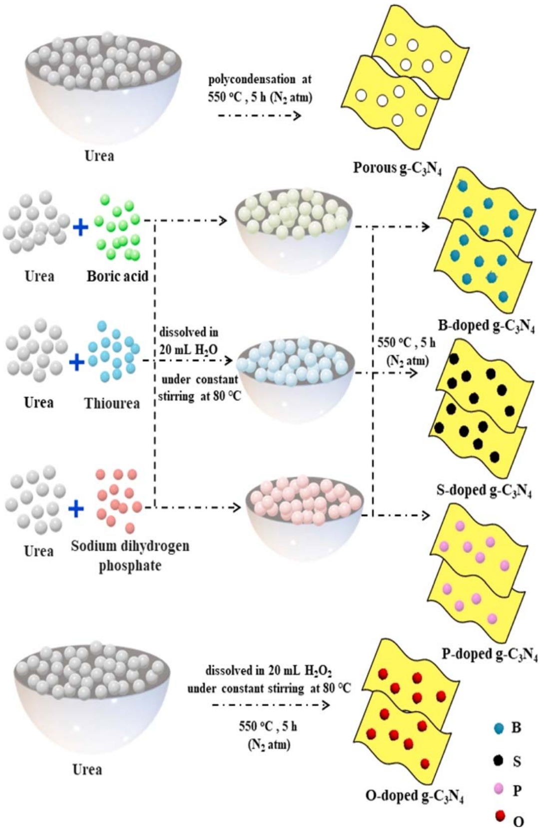

Scheme 5 Schematic of the fabrication of porous $g\text{-}C_3N_4$, B, O, P, and S-doped $g\text{-}C_3N_4$ samples. Reproduced from ref. 182 with permission from [Elsevier], copyright [2022].

blending, the catalyst was subjected to heat treatment at a temperature of 550 °C, at a gradual rate of 5 °C per minute, under an inert gas environment, and maintained for a duration of 5 h. The observations indicated an enhancement in CH_4 production when four non-metal elements were introduced in the mixture, surpassing the initial g-C_3N_4 yield. Notably, the sample doped with S demonstrated the highest methane formation rate at 7.8 mmol g^{-1} h^{-1}. Although S doping did not increase the specific surface area or boost the light absorption abilities of the catalyst, it notably facilitated the efficient separation and mobility of charges. Another type of interstitial doping refers to the mixing of atoms in the gap of the primary lattice. If elements with a large radius different from C and N atoms are added to g-C_3N_4 (such as Na, K, Br, and I), interstitial doping tends to occur.[183,184] In the study by Zhu and colleagues,[185] the impact of incorporating F, Cl, Br, and I on the catalytic properties of single-layered g-C_3N_4 was investigated through first-principles calculations. They proposed that the dual-coordinated N atoms served as the key active sites for photocatalytic reactions, but the dual-coordination N atoms were not always the most stable doping sites.[186] In the case of halogen atoms, they were preferentially doped into the interstitial space surrounded by three triazine units. The F element contributed to the VB, while other halogen atoms participated in the conduction band, reducing the band gap from 1.18 eV to 0.64–1.14 eV. It also exhibited strong light absorption in the wavelength range of 200–1000 nm.[184]

Without introducing foreign elements, g-C_3N_4 can be self-doped under certain conditions, that is, C-doped and N-doped. It has been found that the uniform substitution of N atoms by C atoms during C self-doping causes the formation of delocalized π bonds between the substituting C and the six-membered ring, which affects the band and electron structure of g-C_3N_4. This results in a decrease in its band gap, together with an elevated rate of charge-carrier migration and light absorption.[187] In the process of N self-doping, N atoms are prone to lose extra electrons and become n-type semiconductors, resulting in an intermediate energy gap state to enhance the visible light absorption, which improves the separation efficiency of electrons and holes, reduces the recombination of photogenerated carriers and prolongs the lifetime of photogenerated charges.[188] Fang *et al.*[188] calcined the precursor and nitrogen-rich additives together to prepare C_3N_{4+x}. When there were more dopants, it showed metal conductivity, which absorbed more visible light than the original g-C_3N_4 and accelerated the charge transfer. Liu *et al.*[189] calcined urea and carboxyl-functionalized polystyrene nanospheres in a furnace at 550 °C for 2 h and polymerized them into N-doped C-grafted carbon nitride (Fig. 8a). The modification led to a significant increase in the CO_2 adsorption capacity, jumping from the initial 0.04 mmol g^{-1} to 0.22 mmol g^{-1} at a temperature of 298 K. The improved performance was attributed to the heightened presence of N atoms following the N self-doping of C_3N_4, which boosted the concentration of basic sites. Operating under visible light, the N-doped C-modified carbon nitride catalyst exhibited a remarkable CO generation rate of 15.4 μmol g^{-1} h^{-1}, representing a significant sevenfold enhancement over the undoped g-C_3N_4. Introducing alkali metals into g-C_3N_4 is another facile strategy to enhance its photocatalytic efficiency. The interplay between the doped alkali metal and triazine ring in g-C_3N_4 leads to an electron shift from the nitrogen atom lone pair to the metallic atom, causing electron redistribution. This process suppresses the recombination of photogenerated carriers and strengthens the absorption of visible light. Zhang *et al.*[190] studied the effect of doping g-C_3N_4 with Li, Na, K and Rb on its photocatalytic CO_2 reduction performance. Among them, Rb-doped g-C_3N_4 showed the strongest light absorption. Rb-doped g-C_3N_4 had a thinner lamellar structure with mesopores than pure g-C_3N_4 (Fig. 8b–e). The porous structure was favourable for light absorption and CO_2 adsorption. The change in the electronic structure of all the g-C_3N_4 samples doped with different alkali metals resulted in

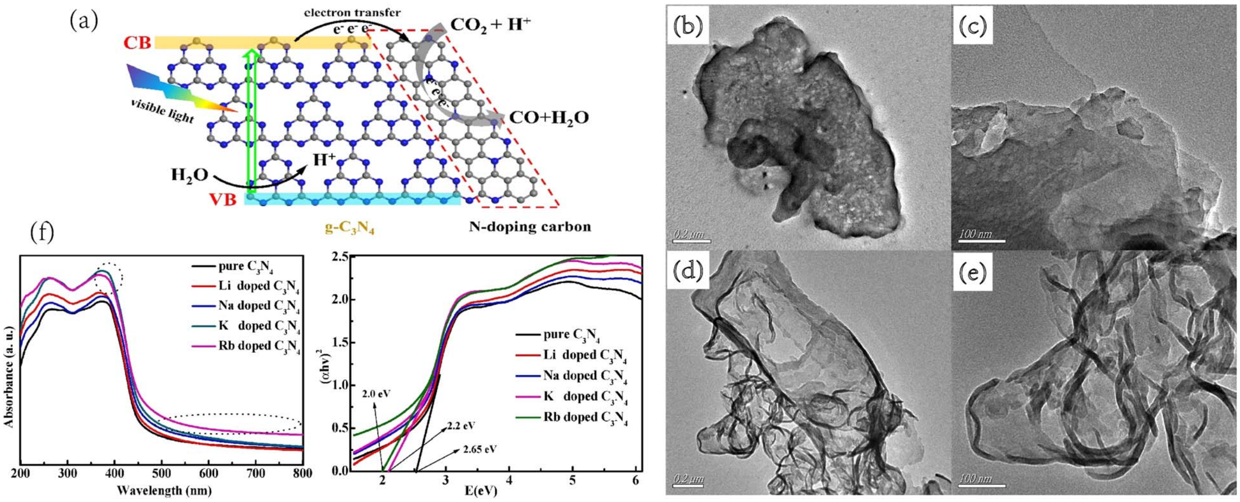

Fig. 8 (a) Diagram of N-doped C-grafted carbon nitride. (b–e) TEM images of undoped g-C_3N_4 and the g-C_3N_4 doped with Rb. (f) Change in band gap before and after doping Rb and change in optical response after doping different alkali metals. (a) Reproduced from ref. 189 with permission from [Elsevier], copyright [2021]. (b–f) Reproduced from ref. 190 with permission from [Elsevier], copyright [2020].

a redshift in its optical response. After doping Rb, the band gap of the catalyst decreased from 2.65 to 2.0 eV (Fig. 8f).

In addition to alkali metal doping, g-C_3N_4 doped by Co, Ni, Cu and other metals has also been widely studied. Wang *et al.*[191] synthesized an Mo-doped g-C_3N_4 photocatalyst with a vermicular mesoscopic structure and higher surface area by pyrolysis. After 8 h UV irradiation, g-C_3N_4 doped with 4% Mo showed the highest activity, reducing CO_2 to CO and CH_4 with yields of 887 μmol g^{-1} and 123 μmol g^{-1} (Fig. 9a and b), respectively. The introduction of Mo led to an expansion in the specific surface area, boosting the light absorption efficiency, prolonging the lifespan of photogenerated carriers, and consequently elevating the photocatalytic performance. Similarly, Dong *et al.*[194] used $MgCl_2$ as a magnesium source to add different amounts of Mg to g-C_3N_4 *via* a one-pot method. The integration of 4 wt% Mg to g-C_3N_4 led to a reduction in its bandgap from 2.70 to 2.65 eV, concurrently creating an intermediate gap. This newly formed mid-gap state functioned as an electron trap, enhancing the efficiency of electron–hole pair separation. Consequently, the 4 wt% Mg-doped g-C_3N_4 catalyst demonstrated the optimal photocatalytic performance under both ultraviolet and visible light conditions.

To overcome the different inherent shortcomings of single-element doping, researchers proposed the strategy of doping two or more elements, namely co-doping. This method takes advantage of each dopant for collaborative catalysis, and the catalytic efficiency is usually higher than that of single element doping; thus, it has been widely investigated in many fields. Babu *et al.*[192] synthesized g-C_3N_4 co-doped with B and S by placing boric acid, thiourea and melamine in a muffle furnace through one pot *in situ* calcination (Fig. 9c). The B and S elements were introduced in the lattice to enhance the light absorption, accelerate the charge separation and migration, and increase the specific surface area of g-C_3N_4. The defects generated by the dopants captured photogenerated electrons, thus inhibiting the recombination of charge carriers. Wang *et al.*[193] mixed dicyandiamide with KBH_4 and calcined it for 2 h at 550 °C. The H_2 generated by the thermal decomposition of KBH_4 created N defects. The band gap gradually narrowed with an increase in the doping concentration. The band gap of pure g-C_3N_4 is 2.74 eV, which decreased to 2.61 eV when 3% K and B elements were added. Moreover, the N defects caused by H_2 generated by the thermal decomposition of KBH_4 reduced the band gap to 2.35 eV (Fig. 9d). In this study, when N atoms and K dopants were close to each other, the electron density became enriched, and the presence of K changed the electron spatial distribution, which made K act as an electron donor and promoted the electron transfer between adjacent layers. The adjacent atoms experienced an electron-abundant state due to the incorporation of both nitrogen vacancies and boron. However, the electron enrichment resulting from nitrogen vacancies exceeded that from boron doping, leading to a higher concentration of basic sites. Consequently, the nitrogen defects exhibited a more robust CO_2 adsorption capacity than B and K doping. B maintained a high reduction potential and compensated for the adverse effect of K. The K, B and N vacancies

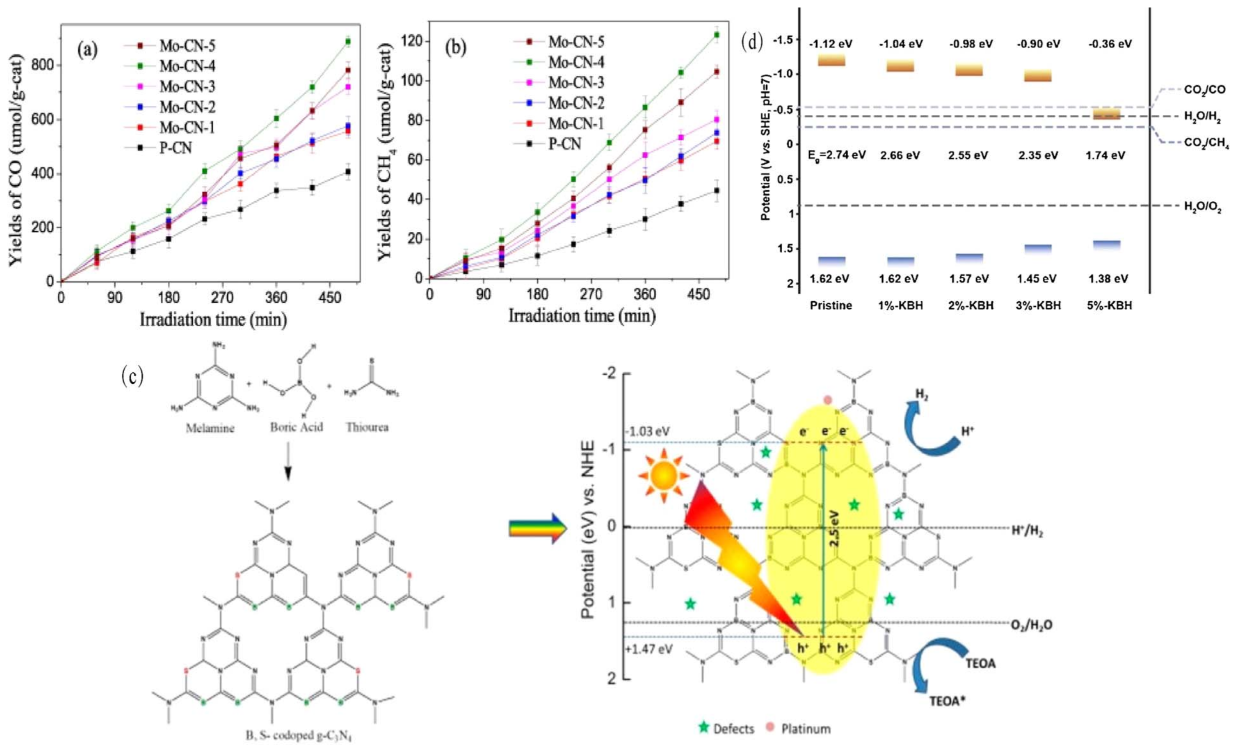

Fig. 9 (a and b) Photocatalytic CO_2 reduction yield and stability of g-C_3N_4 with different doping amounts of Mo. (c) Synthesis of B, S-co-doped g-C_3N_4 by *in situ* calcination method. (d) Comparison of the band gap of g-C_3N_4 doped with K and B. (a and b) Reproduced from ref. 191 with permission from [Elsevier], copyright [2016]. (c) Reproduced from ref. 192 with permission from [ACS Publications], copyright [2018]. (d) Reproduced from ref. 193 with permission from [Elsevier], copyright [2019].

cooperated to realize the photocatalytic reduction of CO_2 to CH_4 and CO without a sacrificial agent.

3.4 Heterojunction formation

In the conventional heterojunction framework, there are three classifications including bridging gap type (type-I), interlaced gap type (type-II), and fracture gap type (type-III).[195] As illustrated in Fig. 10, a type-I semiconductor setup exhibits a scenario where the conduction band (CB) of semiconductor A resides higher than that of semiconductor B; conversely, the valence band (VB) of semiconductor A is situated beneath that of semiconductor B. Electrons and holes shift collaboratively towards semiconductor B. This movement leads to a decline in the effectiveness of charge separation, subsequently reducing the redox potential of the reaction at lower levels. In the context of type-II semiconductors, A possesses a higher CB and VB. Here, electrons transit from the CB to B, while holes move from the VB to A, enabling the efficient separation of electron–hole pairs. However, the redox ability is still weak. In the case of type-III, the band gaps do not overlap and electron–hole pairs cannot transfer. Therefore, researchers need to develop other types of heterojunctions to overcome the limitation of traditional heterojunctions.[196,197]

Exploring the charge migration dynamics in Z-scheme heterojunctions, researchers have categorized this phenomenon into three distinct classifications (Fig. 11) including the conventional Z-scheme heterojunction, all-solid-state Z-scheme heterojunction, and direct Z-scheme heterojunction.[198] The traditional Z-scheme heterojunction was first proposed by Bard in simulating the direction of charge transfer in natural photosynthesis.[199] The traditional Z-scheme photocatalytic system consists of two different semiconductors (S1 and S2) and a receptor/donor (A/D) pair. During the photocatalytic reaction, the electrons generated by S2 will react with A to give electrons to D, and the holes in S1 will react with D to give electrons to A. Thus, this structure can effectively realize the separation of electron–hole pairs and has strong redox ability. However, this type of heterojunction is limited to the solution phase, resulting in difficult charge transfer and narrow application range. In 2006, Tada *et al.*[200] introduced the all-solid-state Z-scheme heterojunction design to facilitate targeted charge migration and broaden its applicability. The photocatalytic system was comprised of a duo of dissimilar semiconductors with noble metal nanoparticles functioning as the electronic mediator. This system has seen substantial endorsement. However, the reliance on scarce and costly noble metal nanoparticles as the electron medium in this solid-state Z-scheme system hinders its wide application. Consequently, researchers have increasingly directed their focus towards investigating direct Z-heterojunctions. In 2013, Yu *et al.*[201] created a direct Z-type heterojunction comprised of g-C_3N_4/TiO_2. In 2016,[202] they conducted an investigation into the electron transportation dynamics within the g-C_3N_4/TiO_2 heterostructure. Our research group used a self-assembly method to vertically fix one edge of a single layer of MoS_2 nanosheets on the surface of SiC nanoparticles to form a marigold-like heterojunction, SiC@MoS_2.[203] This Z-scheme structure could expose the surface of the photocatalyst to the maximum extent to fully contact with the reactants. The high selectivity for the CH_4 product was attributed to the rapid reduction of CO_2 on the surface of SiC by high electron mobility, and the production of O_2 was produced by the rapid oxidation of H_2O on the surface of MoS_2 by high hole mobility. Upon optimization, the catalyst with a 60% MoS_2 composition was determined to be the most favourable blend. It exhibited the CH_4 generation rate of 323 $\mu L\ g^{-1}\ h^{-1}$ and an O_2 production rate of 620 $\mu L\ g^{-1}\ h^{-1}$. These findings indicated that the molar proportion of CH_4 to O_2 approached a 1 : 2 ratio, aligning with the chemical equilibrium of the $CO_2(g) + 2H_2O(g) = CH_4(g) + 2O_2(g)$ reaction.

To a certain extent, the low efficiency of photocatalytic reactions can be attributed in part to the significant disparity in the electron and hole migration rates within semiconductor catalysts, resulting in the accumulation of internal photogenerated holes, which subsequently hinder the production of photogenerated electrons, thereby shortening the lifetime of photogenerated carriers. Based on this, we constructed a direct and indirect Z-type heterostructure coupled photocatalytic system.[204] As shown in Scheme 6, firstly, Pt nanoparticles were loaded on SiC by photodeposition, and then dispersed in an aqueous solution containing Cu^{2+} and $IrCl_6^{3-}$. Under ultraviolet irradiation, Cu^{2+} was reduced to Cu_2O, and $IrCl_6^{3-}$ was oxidized to IrO_x. Finally, the Cu_2O–Pt/SiC/IrO_x composite catalyst was obtained. This catalyst exhibited improved photocatalytic efficiency by constructing a multi-photocatalyst integrated system to enhance the lifetime of the photogenerated carriers and redox ability. Regarding the photo-catalytic conversion of CO_2 and H_2O into HCOOH and O_2, the respective production rates were 896.7 $\mu mol\ g^{-1}\ h^{-1}$ for HCOOH and 440.7 $\mu mol\ g^{-1}\ h^{-1}$ for O_2.

In 2019 and 2020, Yu proposed the S-scheme heterojunction to improve the electron transfer problem of the type-II and Z-scheme heterojunctions.[205,206] The S-scheme heterojunction is a composition involving a reduction photocatalyst (RP) and an oxidation photocatalyst (OP). As depicted in Fig. 12a, the conduction band (CB), valence band (VB), and Fermi energy

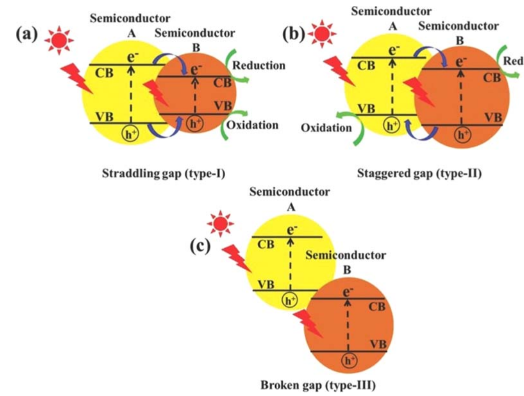

Fig. 10 Three types of traditional heterojunction: (a) bridging gap type (type-I), (b) interlaced gap type (type-II) and (c) fracture gap type (type-III). Reproduced from ref. 195 with permission from [Wiley Online Library], copyright [2017].

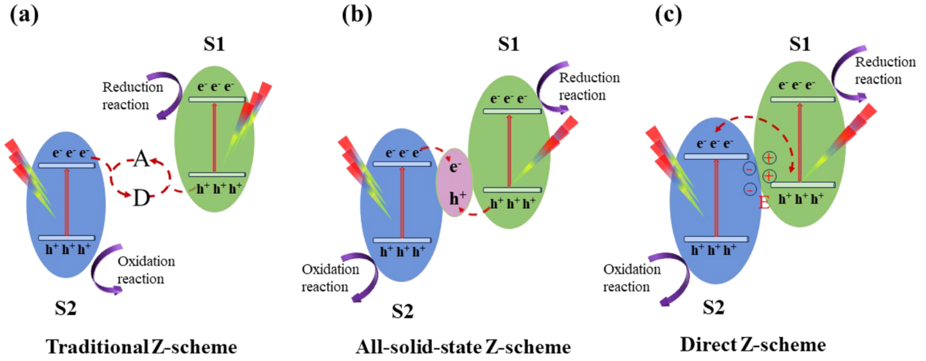

Fig. 11 Three types of Z-scheme heterojunctions: (a) traditional Z-scheme, (b) all-solid-state Z-scheme, and (c) direct Z-scheme.

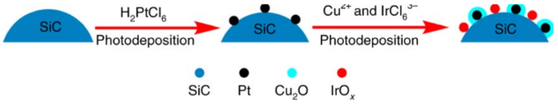

Scheme 6 Process for the formation of Cu_2O–Pt/SiC/IrO_x by photodeposition. Reproduced from ref. 204 with permission from [Nature Publishing Group], copyright [2020].

levels of the RP are positioned above that of the OP to attain equilibrium in the Fermi energy levels at the interface, where the electrons from the RP will naturally transition to the OP. During the electron transfer process, the RP side retains a positive charge and the OP side retains a negative charge, resulting in the formation of an internal electric field at the interface from RP to OP (Fig. 12b). Electrons in both RP and OP are transferred from VB to CB under photoexcitation (Fig. 12c), and the system has the maximum reduction and oxidation capacity.[55] Accordingly, many researchers began to study this emerging topic to reduce CO_2 to hydrocarbon fuel. However, the selection of OP and RP is crucial, which requires that their band structure matches and they have characteristics conducive to CO_2 adsorption and activation. Yang *et al.*[207] synthesized the S-scheme heterojunction g-C_3N_4/TiO_2/C with a thickness of about 5 nm using electrostatic self-assembly and calcination methods. As shown in Scheme 7, firstly, a certain amount of urea was calcined at 550 °C to condense into g-C_3N_4 with layers of stacked flower structure. The pH of the suspension was adjusted to 4 with 0.5 M HCl and deionized water to bring H^+ to the surface. This protonation process was conducive to the stripping of g-C_3N_4 into layers. Then, the prepared $Ti_3C_2T_x$ monolayer with an area greater than 5 μm × 5 μm was added to the suspension as the base plane to obtain g-C_3N_4 with a stretched fold layer. The monolayer was calcined at 400 °C, where the Ti layers were converted into TiO_2 nanoparticles and fixed on the graphite layer to form a rough surface. The g-C_3N_4 with a stretched fold layer was tightly attached to the TiO_2 layer to prevent g-C_3N_4 from agglomerating. Under Xe lamp irradiation for 3 h, the catalyst reduced CO_2 to CH_4 and CO with yields of 3.7 μmol g^{-1} h^{-1} and 25.96 μmol g^{-1} h^{-1}, respectively. The improved performance of the catalyst was attributed to the formation of an S-scheme heterojunction between the two semiconductors, and its layer-to-layer structure could expose the maximum optical absorption area, which provided an effective channel for photogenerated carrier migration. These design schemes provided a new idea for the preparation of multi-junction photocatalysts, which are expected to be extended to other semiconductor catalysts.

Although type-II, Z-scheme and S-scheme heterojunctions all have staggered energy band structures, type-II and Z-scheme

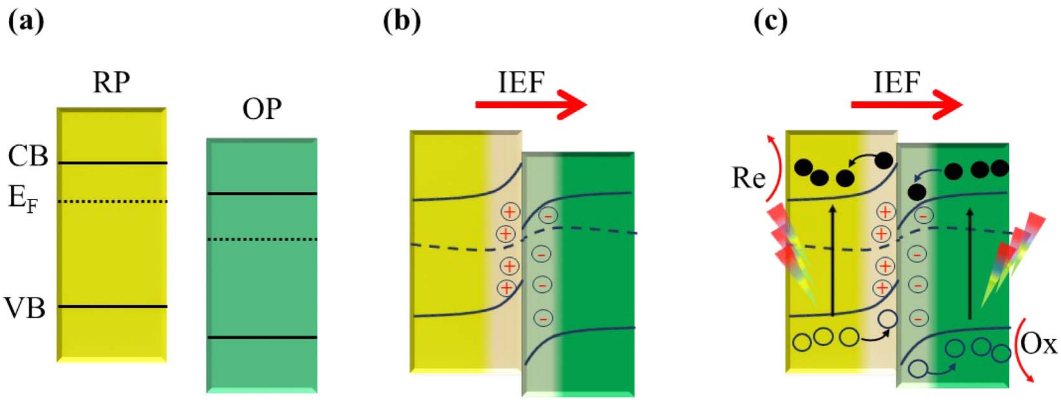

Fig. 12 Carrier transfer mechanism of S-type heterojunctions: (a) band structure of RP and OP, (b) formation of IEF after RP and OP coupling, (c) photogenic carrier transfer and separation under light irradiation.

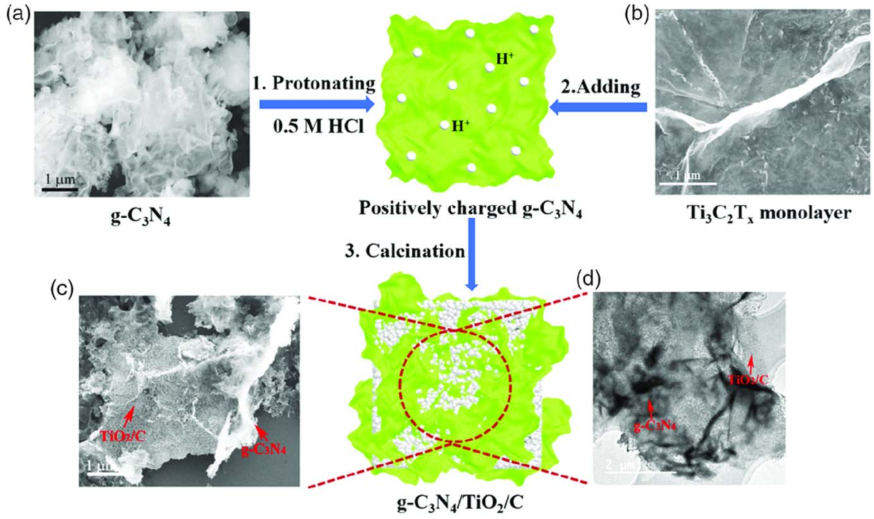

Scheme 7 Process for the preparation of g-$C_3N_4/TiO_2/C$. Reproduced from ref. 207 with permission from [Wiley Online Library], copyright [2021].

heterojunctions present challenges in terms of thermodynamics, photogenerated carrier transfer kinetics and energy utilization. Alternatively, the S-scheme heterojunction, as a new strategy to increase the separation and migration rate of photogenerated carriers under the influence of an internal electric field, has largely eliminated many of the inherent defects of the traditional Z-type heterojunction and other heterojunctions, and therefore has become a research hotspot in the field of photocatalytic energy and environmental applications. Deng *et al.*[208] synthesized an In_2O_3/Nb_2O_5 S-scheme heterojunction by mixing Nb_2O_5 and In_2O_3 in the same electrospinning solution and roasting at high temperature. The heterojunction synthesized by this method exhibited close interface contact and promoted ultra-fast (<10 ps) electron transfer at the interface. The optimized In_2O_3/Nb_2O_5 nanofibers extended the lifetime of the catalyst and improved the CO_2 reduction performance due to the rapid interfacial charge transfer and effective CO_2 activation on the catalyst. The CO yield was as high as 0.21 mmol g^{-1} h^{-1}. Combined with FSTAS analysis, it was shown that the photoelectron transfer on the CB of In_2O_3 to VB of Nb_2O_5 inhibits the self-carrier recombination, effectively separates the electrons in the CB of Nb_2O_5 and the holes in the VB of In_2O_3, prolongs the life of the nano-hybrid materials, and proves the potential of the S-type heterojunction interface in ultrafast charge transfer. In addition, Sun *et al.*[209] synthesized a novel S-type heterojunction Ga_2S_3/CuS catalyst using a simple two-step hydrothermal method. A series of characterization analyses of PL and time-resolved PL showed that the S-type heterostructure is advantageous for the improvement of the photogenerated electron–hole separation efficiency. Density functional theory also proved that the Ga_2S_3/CuS interfacial electric field can promote the adsorption of CO_2 and intermediate products. *In situ* KPFM indicated the transfer of photogenerated electrons from Ga_2S_3 to CuS under light conditions. This study elucidated the action mechanism of the intrinsic electric field at the S-type heterojunction interface and provides a new way to improve the selectivity of CO_2 reduction to CH_4 in photocatalysis.

3.5 Single-atom engineering

In 2011, Zhang *et al.*[210] constructed a Pt–O–Fe structure and successfully fixed a Pt atom to FeO_x and proposed the term single-atom catalysts (SACs), which advanced the process of elucidating the catalytic active site at the atomic level. In 2014, in the work by Yang *et al.*,[211] a groundbreaking one-step approach was employed to fix individual metal atoms (including Pt, Pd, Rh, and Ru) on the surface of TiO_2, revealing that these single-atom catalysts exhibited a superior photocatalytic H_2 generation performance compared to TiO_2-supported metal clusters. After that, the field of photocatalysis opened the door to SACs. It was also realized that as the size of metal nanoparticles was gradually reduced to a single atom, the individual atoms embedded in the carrier could regulate the energy band and electronic structure and change the surface structure of the catalyst through the overlap of electron orbitals and interaction with the carrier ligand.[212] The support of SACs usually acts as a light collection unit. As the first step of photocatalysis, light collection is also a necessary step to achieve visible light absorption, which can provide sufficient electron–hole pairs for subsequent catalytic reactions. The catalytic activity and selectivity are fundamentally shaped by the metallic single atoms functioning as active centres. Excited electron transfer from these metal atoms to the support leads to a reshuffle of charge distribution between the individual metal atoms and the support. Consequently, this alteration in local electronic properties influences the photocatalytic performance.[210,213,214] If these three parts are properly optimized, the final atomic utilization rate will reach nearly 100%. Based on this, researchers began to design various single-atom construction methods, and this modification strategy has become one of the most promising research directions in the field of photocatalysis.[215–227]

Wet chemistry is a common and simple traditional method for preparing supported monatomic catalysts because it can be done in ordinary laboratory operations. It includes the co-deposition method,[210,213] sol–gel method,[228,229] impregnation method,[230,231] depositional precipitation method[232,233] and strong electrostatic adsorption method.[234] Among them, the metal atoms prepared by the co-deposition method and sol–gel method may be buried in the support, leading to a decrease in atomic utilization. The metal atoms prepared by the impregnation method can be directly anchored on the surface of the support to avoid the above-mentioned problems, but there is a problem of uneven dispersion. The final crystal size of the sedimentation-precipitation method depends on the nucleation and growth rate during the precipitation process, which is difficult to control. When the metal load is high, the particle size and dispersion are uneven, and thus the dispersion can only be maintained evenly under a low load. In the process for the creation of strong electrostatic adsorption, the conditions are not controllable and the surface active sites are not uniform. It can be seen that wet chemical synthesis methods are simple and direct, but they lack precise control of the size and dispersion of sites, structure and composition of the active units of the catalyst.[235] Single metal atoms have a higher surface energy than nanoclusters and nanoparticles, resulting in their easier migration and aggregation during preparation.[236] It has been reported that when the support is doped with heteroatoms,[24,94–97] vacancies,[237–240] surface groups[102,103] and single-atom step edges,[25,79,104] the defects formed by the introduction of surface groups can be used as anchoring sites of metal single atoms to prevent the agglomeration of the atoms. When designing catalysts, the stability of single metal atoms is a crucial factor. One approach involves attaching single metal atoms directly to light-absorbing substances, necessitating an abundance of anchoring sites and reaction sites across the support surface. Some traditional semiconductors, such as TiO_2,[75,100,105,106] CeO_2,[215,229,232,233,241,242] and FeO_x,[210,213,243] can be replaced by a single atom because of their surface metal cations and can interact with oxygen anions to achieve the anchoring of single metal atoms.

Although many MOs are regarded as effective carriers of SACs, the single-atom load is still unsatisfactory due to the limited number of constructed sites, and their structure and properties are difficult to adjust at the molecular level, and thus researchers are urgently searching for ideal materials that can increase the load by orders of magnitude.[96,244–250] In this case, organic polymers can satisfy these requirements.

g-C_3N_4 is also a popular photocatalyst for anchoring single metal atoms. The unique cavity in its structure has six N atoms, which are suitable as anchoring sites and their lone pair electrons can combine with single metal atoms with empty or partially empty orbitals, breaking the limitations of anchoring traditional materials and insufficient reaction sites, and significantly improving the load content of single metal atoms.[251–253] Theoretically, the ultimate load content depends on the maximum number of matches between the metal atoms

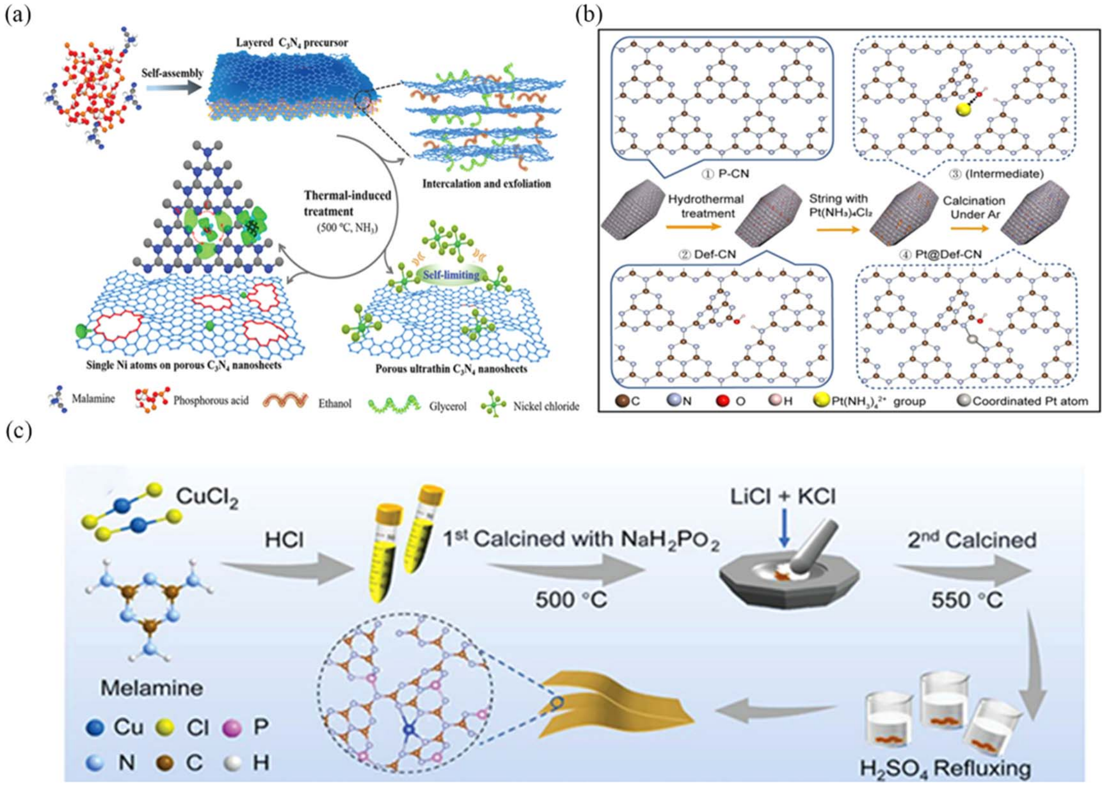

Fig. 13 (a) Schematic of the introduction of defects in g-C_3N_4 by Pt cationic groups and oxygen-containing functional groups. (b) Diagram of Ni confinement in g-C_3N_4 vacancy ligands with fewer porous layers. (c) Anchoring site synthesis diagram of Cu–N_4 in P-doped g-C_3N_4. (a) Reproduced from ref. 254 with permission from [Wiley Online Library], copyright [2020]. (b) Reproduced from ref. 255 with permission from [Wiley Online Library], copyright [2022]. (c) Reproduced from ref. 256 with permission from [Wiley Online Library], copyright [2023].

separated by the target and the anchoring sites. Cheng *et al.*[254] increased the density of monatomic active sites by using a self-limiting method to confine Ni to the g-C_3N_4 vacancy ligand with fewer porous layers by using an unsaturated edge (Fig. 13a). Shi *et al.*[255] introduced Pt cationic groups and oxygen-containing functional groups into the defect edge of defective g-C_3N_4 to form intermediates, and low-temperature calcination could make the Pt atoms closely connected with it without affecting the structure of the support (Fig. 13b). Xie *et al.*[256] designed Cu–N_4 anchoring sites in P-doped g-C_3N_4 to promote the formation of C–C coupled intermediates and adjusted the intermediate energy level of the reaction path of the target product to increase the selectivity for the high value-added product C_2H_4, reaching 53.2% (Fig. 13c). To increase the single atom load, Ma *et al.*[257] prepared Co/g-C_3N_4 *via* a two-step calcination process, where the load of Co restricts the potential for efficient photocatalytic CO_2 reduction, thereby hindering the conversion of CO_2 into valuable products. This research introduces an innovative approach for the development of SACs with a high loading and superior dispersion.

At present, the commonly used method for the synthesis of SACs with an M–N–C structure is high-temperature pyrolysis, but the coordination environment of M–N_x in the catalyst is uncertain.[258] Compared with the SACs obtained by pyrolysis, the structure of the molecular catalyst is controllable, which is helpful for the study of the mechanism of single active sites.[259,260] Determining the consistency of the surface active sites is a future research focus in the field of SACs, which is conducive to improving the selectivity for CO_2 reduction products. The loading of Co atoms on the surface was up to 24.6 wt%, which achieved the reduction of CO_2 to CH_3OH (941.9 μmol g^{-1}) under 300 W Xe lamp irradiation for 4 h without adding sacrificial and photosensitizing agents. The key points of this experiment are shown in Scheme 8. (1) The massive g-C_3N_4 formed porous sheets with a high specific surface area after being treated with concentrated H_2SO_4, which could provide enough coordination sites for anchoring Co atoms to inhibit atomic aggregation. (2) The synthesis adopted two calcination steps. In the first stage, it was maintained at 130 °C for 9 h to ensure that the H_2O adsorbed in the mixture of g-C_3N_4 and $Co(NO_3)_2\cdot 6H_2O$ was removed cleanly. In the second stage, the temperature was increased to 550 °C to vaporize the Co atoms not fixed on the surface. When the g-C_3N_4 bulk and cobalt nitrate were subjected to direct calcination in one step, the tendency for aggregation on the surface led to the formation of CoO_x. This is the reason for the lack of active sites in low-loading single-atom catalysts (SACs).

3.6 Surface organometallic catalysis

Surface organometallic catalysis (SOMC)[261–263] is the rational bonding of molecular precursors (organometallic or coordinate compounds) to the surface of a carrier (such as oxides, metal nanoparticles, and carbon materials) according to the rules of coordination chemistry. The carrier surface controls the reactivity of the molecular precursors, and the grafted molecular complexes can directly act as active centres or be modified after heat treatment under vacuum, inert gas or reactive gas before participating in catalytic reactions.[264] The life of some organometallic compounds sensitive to oxygen, water and temperature can be extended after grafting to a support, which is new molecular technology for the synthesis of single active site, homogeneous functional heterogeneous catalysts. Different from SACs, organometallic compounds retain their partial distribution after grafting, which is a special case of SACs. Abundant –OH groups are present on the oxide surface at 700 °C,[265] and thus organometallic compounds are usually connected to the isolated hydroxyl groups on the surface of the oxide to form M–O bonds. Given that oxides have been the most widely used graft support, we focus on describing the design strategies of SOMC supported by solid oxides. Molecular-level synthesis provides great help in improving the structural uniformity of catalysts.

The synthesis of heterogeneous catalysts using molecular strategies requires understanding the controlled structure and catalytic behaviour of surface species to establish structure–activity relationships. Specific organometallic species have active sites similar to that of supported MOs, and they usually possess a larger fraction of active sites, making structure–activity relationships possible. There are many –OH present on the surface of MOs and they are directly related to the density and coordination surroundings of the metal sites; thus, they are often considered the grafting sites.[265] Accordingly, controlling the number of –OH groups on the surface of the oxide support becomes the key to the successful synthesis of SOMC. The type and density of the surface groups (MOs–OH, MOs–O–Ms or MOs–OH_2) of the oxide carriers can be changed by certain treatment. As shown in Scheme 9, heat treatment under vacuum can remove the adsorbed H_2O and condense the nearby MOs–OH sites, leaving more MOs–O–MOs between the metal complex and the oxide, and this process reduces the density of

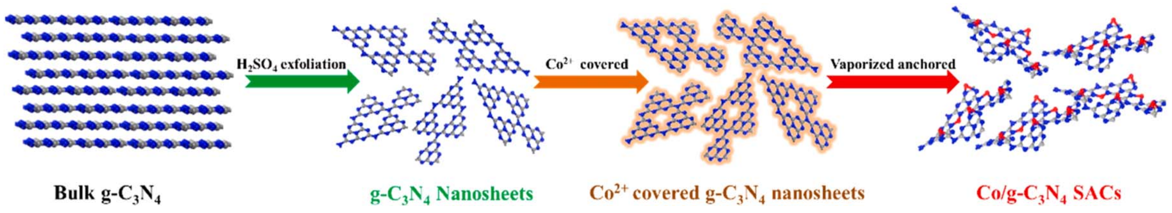

Scheme 8 Schematic representation of Co/g-C_3N_4 by a two-step calcination method (blue: N atoms; grey: C atoms; and red: Co atoms). Reproduced from ref. 260 with permission from [Wiley Online Library], copyright [2022].

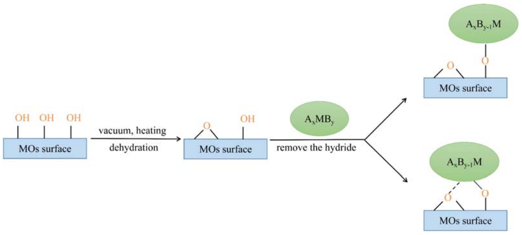

Scheme 9 Process of dehydroxylation and grafting of MOs. Reproduced from ref. 265 with permission from [Elsevier], copyright [1998].

functional MOs–OH on the oxide surface. When the active B^- ligand is attacked by unstable protons, the site-isolated MOs–OH reacts with the molecular precursor A_xMB_y to form well-defined surface species as single-site MOs–O–MA_xB_{y-1}, which can also interact with neighbouring MOs–O–MOs.[264]

Evaluating the structure of the grafted complex at the molecular and atomic levels is a key step in understanding its stability and reactivity, and thus it is necessary to determine the structure of the carrier prior to the preparation of SOMCs. In general, carriers with a high surface area and a certain number of hydroxyl groups on their surface (such as TiO_2, SiO_2, Al_2O_3, and ZrO_2) are we preferred, but we need to consider that some oxides tend to undergo phase transitions or sintering when heated in the presence of H_2O. One way to ameliorate this dilemma is to moisten MO powder with H_2O, and then slowly evaporate it in a drying oven. The fine powder is condensed into larger, more easily filtered particles, and then the carrier is calcined at a temperature lower than dehydroxylation to remove organic impurities.

In the case of the metal precursors, researchers usually choose hydrocarbons, amides, pyridines, porphyrins, and siloxane, sometimes grafted in organic solvents to avoid surface chemical reactions that dissolve or reprecipitate the oxide support in H_2O, making the preparation process more complex.[266–271]

The graft of organometallic compounds can be anchored by organometallic fixation[272,273] or ALD,[274,275] which takes advantage of the homogeneity of the molecular precursors. Both methods enable a level of control and flexibility that contributes to the clarification of structure and mechanism, compared with traditional catalyst synthesis techniques, advanced molecular-level preparation provides a way for rational catalyst design. The specific grafting process is as follows: firstly, the carrier is placed in a vacuum infrared tube for dehydroxylation.[276] The reactor in the infrared tube can slide up and down and its head contains infrared transparent windows (CaF_2, KBr, *etc.*) to obtain a spectrum and facilitate the monitoring of the consumption of hydroxyl groups on the surface through infrared spectroscopy during the experiment. Subsequently, the volatile metal precursor can be grafted in the gas phase by sublimating the compound to a carrier using a vacuum tube attached to the reactor. It is important to note that the grafting of the molecular precursors to the oxide carrier requires strict anhydrous and anaerobic conditions because most organics decompose easily in H_2O and O_2. SOMCs form isolated sites more selectively than impregnation, which facilitates the binding of metal sites into the carrier.

Compared with single-metal catalysts, bimetal catalysts have double active sites, and the synergistic effect of the two metals leads to an improvement in their stability, activity and reaction selectivity.[277–279] However, it is more difficult to control the uniform reaction sites on the carrier surface, which is affected by many factors, such as temperature, metal type, dispersion, particle size, and precursor metal feed ratio. Thus far, this has been a serious challenge. In the work by Lian,[280] the concept of a “dual surface organometallic complex” was introduced through the hydrogenation of supported bimetallic cluster catalysts, drawing from the principles of surface organometallic chemistry. This innovative idea served as a foundational approach for the development of multifaceted metal catalysts, featuring numerous active sites, which could be anchored to a variety of supports.

4 Reaction efficiency and product selectivity of photocatalysis CO_2 with H_2O

At present, the utilization of diverse semiconductor materials in photocatalytic CO_2 conversion encounters challenges of low efficacy and unsatisfactory product selectivity. Various approaches to boost the efficiency of CO_2 reduction have been compiled. Focusing on improving the selectivity of the process towards economically viable and sustainable fuel production, we review the progress in manipulating the product selectivity in photocatalytic CO_2 reduction reactions. Additionally, we classify the prospective photocatalytic products together with recent photocatalysts, aiming to offer ideas for the development of efficient photocatalysts. In 2012, Kuhl *et al.*[281] found that CO_2 could be reduced to 16 different products. If more than two electrons and protons are transferred, CH_4, CH_3OH, C_2H_5OH, C_2H_4, and other products may be formed. The product selectivity is primarily influenced by both the dynamics and thermodynamics (Fig. 14). The dynamic factors include the separation efficiency of photogenerated electrons–holes, distinct active sites, and gaseous and liquid products. For example, when two electrons and protons are transferred, CO

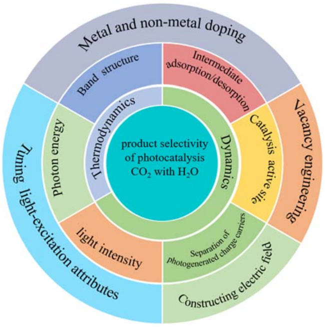

Fig. 14 Diverse elements influencing the selectivity of photocatalytic CO_2 conversion and prospective enhancement approaches.

and HCOOH may be formed. Also, the adsorption/desorption characteristics of reactants/intermediates, *etc.* Regarding thermodynamics, by optimizing the band structure to elevate the CB position, certain semiconductor materials can facilitate the production of compounds that are thermodynamically unfavorable, thereby influencing the product selectivity. Hence, we can explore these two aspects and employ suitable strategies for catalyst modification to enhance the product selectivity.

When the adsorbed H_2O molecules undergo an oxidation reaction by the photogenerated hole, oxygen and H^+ ions are produced on the semiconductor surface. Electrons with reducing power also reduce H^+ to hydrogen. Moreover, when the pH of the reaction solution is low, the rate of HER increases to produce hydrogen gas. Thus, hydrogen evolution is the competitive reaction to affect the efficiency of photocatalytic activity and the product selectivity of CO_2 reduction. In this case, suppressing H_2 generation and improving the CO_2 reduction efficiency are important considerations in CO_2 reduction with H_2O. Surface engineering of catalysts and controlling the reaction system are often considered for suppressing H_2 generation. Selecting catalysts with a higher affinity for CO_2 than for protons is favourable to suppress HER. For example, metal catalysts such as copper, silver, and gold have shown good selectivity for CO_2 reduction.[282–284] In addition, the construction of alkaline sites on the surface of the photocatalyst can enhance the CO_2 adsorption capacity. Meanwhile, increasing the hydrophobicity of the catalyst surface can inhibit proton reduction.[91–93] The reaction system operating in near-neutral or weakly alkaline electrolyte can reduce the availability of protons, thereby inhibiting HER. This can be achieved by using buffers or adjusting the electrolyte composition. Moreover, some electrolyte ions also affect the adsorption of CO_2 and protons on the catalyst surface. For example, bicarbonate ions can promote CO_2 reduction. Therefore, we can also inhibit HER by adjusting the ionic strength and composition of the reaction system. Implementing a flow cell reactor improves the mass transport and increases CO_2 concentration at the electrode surface, thereby reducing the competition from HER.[285,286] By integrating these strategies, the selectivity and efficiency of the p-CO_2R process can be improved, while minimizing the competing HER.

In the photocatalytic CO_2 reduction system, using electrolytes of primarily salts also has an important influence in the activity and selectivity of the reduced products. Research has indicated that the adsorption of sulfites, K_2SO_4, NaCl, $NaHCO_3$, *etc.*, and alkalis such as NaOH on the surface of the photocatalyst induces alterations in its surface properties, which can hinder CO_2 reduction and inter-particle contact between the photocatalytic particles and reduce the electron transport efficiency between the photocatalyst particles.[287] Furthermore, adding alkaline salt to the reaction solution can facilitate the production of CO and enhance its selectivity. This heightened CO_2 reduction activity can be attributed to favorable pH conditions and effective provision of hydrated CO_2 molecules by adding alkaline salt to supply reactants. Simultaneously, an appropriate concentration of alkaline additives will also aid in stabilizing certain photo-corrosive metal sulfide materials during CO_2 reduction.[285] Additionally, Das *et al.*[288] examined how varying the NaOH concentration affects the catalytic activity by adjusting the solution pH. Their research revealed that methane production increases with an increase in the pH level due to the increased solubility of carbon dioxide in the reaction medium at higher pH values, leading to a greater concentration of CO_2 near the catalyst surface, which is conducive for carbon dioxide reduction. However, when reaching a certain threshold level of pH value, insufficient proton supply on the adsorbed CO_2 surfaces becomes detrimental for photocatalytic CO_2 reduction. Therefore, we believe that adjusting the type of reaction solution can enhance and stabilize the photocatalytic performance for CO_2.

4.1 C1 products

Although various C_1, C_2 and C_{2+} products are produced from CO_2 reduction, the majority of current research on photocatalytic CO_2 reduction is focused on the generation of C_1 products, such as CO, CH_4, CH_3OH, and HCOOH. These C_1 products can be used directly as an energy source or serve as a cost-effective carbon source. The conversion of CO_2 into low-cost C_1 products using solar energy through environmentally friendly methods holds significant importance and plays a pivotal role in meeting the present energy and chemical requirements.[78,121,122]

4.1.1 CO and CH_4. CO and CH_4 are the most common products in the photocatalytic reduction CO_2 with H_2O. There have been many reports on the development of novel photocatalysts for CO and CH_4 production. The adsorption and desorption characteristics of CO on the surface of the photocatalyst greatly influence the product selectivity during photocatalyzed CO_2 reduction.[13,55,120,289] Due to its suitable reduction potential and two-electron reduction process, CO is readily obtained as the primary product. Tables 1 and 2 list the recent advances in the photocatalytic reduction of CO_2 with H_2O to produce CO and CH_4.

According to Table 1, it can be seen that great progress has been made in the work on the reduction of CO_2 emissions *via* CO_2 conversion to CO. Without the need for a sacrificial agent, the highest activity recorded was 608 μmol g^{-1} h^{-1},[290] and the selectivity reached almost 100%.[291] To achieve the optimal activity and selectivity, compared with traditional oxide photocatalysts, researchers are more inclined to modify Bi-based photocatalysts due to their unique layered structure. The layered structure of Bi-based photocatalysts facilitates electron–hole pair separation when the Br_{4p} electrons transition to the Bi_{6p} orbitals, resulting in an internal electric field between the $[Bi_2O_2]^{2+}$ layers and X^- layers. This prolongs the photogenerated charge carrier lifetimes, thereby improving the photocatalytic performance.[310–312] However, compared with CO, obtaining high-added value products such as CH_4 is imperative but very difficult. Currently, the photocatalytic CO_2 conversion to CH_4 reported under the condition of no sacrificial agent has the highest activity of 1640 μmol g^{-1} h^{-1},[298] and selectivity of 100%,[159] but it cannot have the two advantages of high activity and selectivity simultaneously. This because it requires the

Table 1 Summary of the photocatalytic systems for CO_2 reduction with H_2O to product CO

Catalyst	Light source	Production/μmol g^{-1} h^{-1}	Selectivity	Reference
Ag_1@PCN	300 W Xe lamp	160	94%	70
AgBr/BiOBr(OVs)	300 W Xe lamp	212.6	90.3%	133
Cu SAs/TiO_2	300 W Xe lamp	65.8	100%	249
Ag–Cu_2O/TiO_2	300 W Xe lamp	13.19	73.7%	282
BiOBr/Bi_2S_3(OVs)	300 W Xe lamp	100.8	74.8%	283
Au nanoparticle-loaded TiO_2	300 W Xe lamp	608	99%	290
Mn_1Co_1–CN	300 W Xe lamp	47	∼100%	291
Ag-loaded Ga_2O_3/$ZnGa_2O_4$	400 W Hg lamp	—	∼100%	289
NiAl-LDH/Ti_3C_2	300 W Xe lamp	11.82	92%	292
Defective CeO_2	300 W Xe lamp	7	∼100%	293
Ultrathin $Bi_4O_5Br_2$	300 W Xe lamp	31.57	99.5%	294
g-C_3N_4/$FeWO_4$	Visible light (λ > 420 nm)	6	99%	295
TiO_2/$BiVO_4$-4	300 W Xe lamp	17.33	100%	296
Bi–$Bi_2Sn_2O_7$	300 W Xe lamp	114.1	100%	297

Table 2 Summary of the photocatalytic systems for CO_2 reduction with H_2O to produce CH_4

Catalyst	Light source	Production/μmol g^{-1} h^{-1}	Selectivity	Reference
$V_{O,N}$-NBCN	300 W Xe lamp	5.90	—	79
Fe/SiC	300 W Xe lamp	30.0	94.3%	101
Pt@Ag–TiO_2	350 W Xe lamp	160.3	87.9%	131
Pt/TiO_2	300 W Xe lamp	150.04	∼100%	159
WO_{3-x}	300 W Xe lamp	1640	95%	298
Pt@h-BN	300 W Xe lamp	184.7	99.1%	299
Pt/SiC nanosheets	300 W Xe lamp	13.6	96.79%	300
Bi_2WO_6–Cl nanosheets	300 W Xe lamp	1.66	94.98%	301
CNBr	300 W Xe lamp	16.68	70.27%	302
Pt@Def-CN	300 W Xe lamp	6.3	97%	303
Au@Pd–TiO_2	300 W Xe lamp	26.32	99.7%	304
HAP/TiO_2	300 W Xe lamp	4.64	99.1%	305
N-doped C dot/CoAl-LDH/g-C_3N_4	300 W Xe lamp	5.69	99%	306
Bi_2MoO_6/Co_3O_4	300 W Xe lamp	28.5	100%	307
V_O-Nb_2O_5	300 W Xe lamp	19.14	94.1%	308
(Pt/TiO_2)@rGO	300 W Xe lamp	41.3	99.1%	309

active site on the catalyst surface to enrich more electrons during the reaction to complete the eight-electron conversion process. Among the many strategies to improve the performance of photocatalysts, designing heterojunctions is one of the most convenient ways in terms of current technology and research. In this way, the combination of two catalysts with disparate band gaps can effectively enhance the separation efficiency of photoelectrons and holes, thereby improving the overall performance. In the work by Wang *et al.*,[133] they integrated BiOBr with other semiconductor materials to create a heterojunction system. As depicted in Fig. 15a, within the BiOBr/AgBr heterojunction, the electrons gathered in the conduction band (CB) of AgBr were prompted to recombine with holes present in the valence band (VB) of BiOBr due to the influence of Coulomb interaction and an internal electric field (IEF). This unique S-type band alignment promoted the highly effective spatial separation of photogenerated electron–hole pairs. As a direct consequence, this led to a remarkable improvement in both the CO generation rate and selectivity compared to the untreated BiOBr. The yield of CO and CH_4 amounted to 212.6 μmol g^{-1} h^{-1} and 5.7 μmol g^{-1} h^{-1}, respectively, demonstrating an approximate increase of 9.2-fold and 5.2-fold over pristine BiOBr. Remarkably, the CO selectivity attained an outstanding percentage of 90.31%. Wang *et al.*[282] constructed Ag, CuO, and TiO_2 into a ternary Z-scheme heterojunction catalyst *via* a one-step reduction method. The Z-scheme heterojunction formed by P25 and CuO improved the separation efficiency of photogenerated electrons and holes. Alternatively, Ag nanoparticles further improved the electron transport efficiency and promoted the absorption of visible light, preventing the self-reduction of CuO. Compared with P25 and the binary heterojunction formed by Ag or CuO and TiO_2 alone, the constructed ternary Z-scheme heterojunction catalyst greatly increased the yield of CO, and the selectivity reached 73.74%.

However, traditional heterojunctions still exhibit deficiencies such as poor interface contact and low active site density. Through morphology regulation, 2D/2D

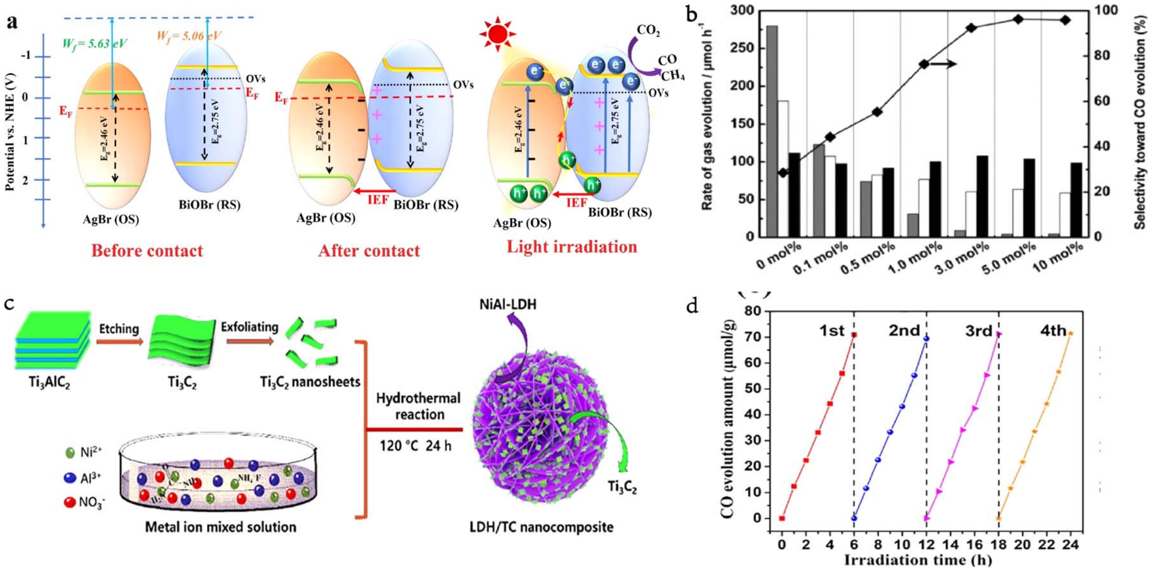

Fig. 15 (a) Electron transfer mechanism of BiOBr and AgBr before and after illumination. (b) Schematic of 3D layered nanocomposite LDH/Ti_3C_2 with high specific surface area by *in situ* hydrothermal method. (c and d) $Ga_2O_3/ZnGa_2O_4$ photocatalytic performance test: yield, selectivity and stability. (a) Reproduced from ref. 113 with permission from [Elsevier], copyright [2022]. (b) Reproduced from ref. 292 with permission from [Elsevier], copyright [2021]. (c and d) Reproduced from ref. 289 with permission from [Nature Publishing Group], copyright [2020].

heterojunctions are constructed to achieve good contact between two-dimensional materials, thereby effectively enhancing the migration rate of photogenerated charge carriers and accelerating surface reactions. This approach improves the adsorption and transport of CO_2, ultimately enhancing both the selectivity and activity, such as LDH/Ti_3C_2,[292] and Ga_2O_3/$ZnGa_2O_4$.[289] Shi proposed the construction of a 3D layered nanocomposite, LDH/Ti_3C_2, with a high specific surface area *via* an *in situ* hydrothermal approach, as depicted in Fig. 15b. The resulting 2D/2D LDH/Ti_3C_2 established a close contact interface, effectively promoting the separation of photoelectron–hole pairs in NiAl-LDH. Additionally, it offered abundant REDOX active sites with enhanced exposure, leading to improved CO_2 absorption and activation. Photocatalysis reduced CO_2 to CO with a selectivity of up to 92% and excellent stability. Also, the selective enhancement of CO was observed in the Ga_2O_3/$ZnGa_2O_4$ heterojunction catalyst. H_2 generation was significantly inhibited when the concentration of $ZnGa_2O_4$ increased from 0.1 mol% to 10.0 mol%. Finally, the $Ga_2O_3/ZnGa_2O_4$ heterostructure achieved nearly 100% selectivity towards CO generation, as illustrated in Fig. 15c and d. The investigation revealed that the heterojunction effectively facilitated the segregation of photogenerated electron–hole pairs; however, it lacked adequate electron enrichment capacity. Thus, to compensate for this, dual cocatalysts with contrasting attributes are strategically engineered on the photocatalyst surface to govern the migration of electrons and holes. Metal atoms can be used as CO_2 adsorption activation and reduction sites.[249,289,313] Fig. 16 depicts the process in which Long *et al.*[290] implemented a phase doping approach to integrate conventional face-centred cubic (fcc) phase Au nanoparticles onto TiO_2. They accomplished photoreduction by altering the chemical composition of the fcc phase Au NP surface. The resulting gold nanoparticles (T–Au NPs) successfully solved the thermodynamic bottleneck of CO_2 conversion to CO, and the 5-T–Au/TiO_2 composite exhibited the maximum CO production rate at 609 μmol g^{-1} h^{-1}. The T–Au nanocomposites played a dual role, functioning both as an electron storage medium to enhance the electron withdrawal from TiO_2 and as an active centre for CO_2 conversion reactions. The exceptional CO selectivity exhibited by T–Au/TiO_2 may stem from the lowered energy threshold for CO formation due to the presence of dual Au NPs, combined with easier desorption on the catalyst surface. Nonetheless, the

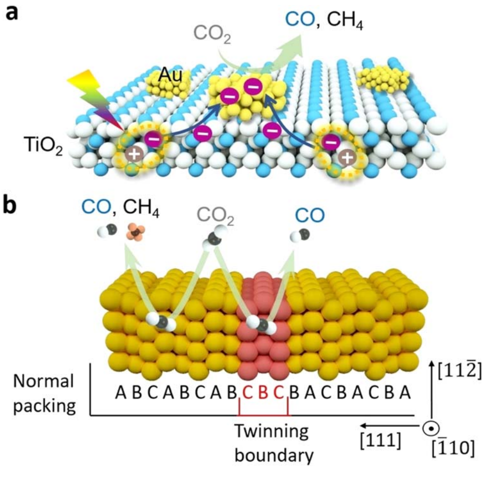

Fig. 16 (a) Schematic of CO_2 photoreduction on gold nanoparticles loaded on TiO_2 photocatalyst. (b) Schematic representation of twin stacking fault in Au crystal viewed along the [110] zone axis. Reproduced from ref. 290 with permission from [Wiley Online Library], copyright [2022].

restricted affordability and scarcity of noble metals limit their broad application as ancillary catalysts in photocatalytic processes. Consequently, numerous researchers have been actively seeking viable alternatives to noble metal co-catalysts. However, in comparison with noble metal co-catalysts, the progress in developing non-noble metal counterparts has been relatively sluggish.

In recent years, single-atom catalysts (SACs) have attracted significant interest from researchers due to their active site specificity, and have become one of the frontiers of contemporary catalysis research. Li *et al.*[291] loaded bimetallic single atoms onto CN to form double active sites. When Mn was combined with Fe, Co, Ni, and Cu, the CO formation rate of the Mn_1Co_1–CN catalyst was the highest, reaching 47 μmol g^{-1} h^{-1} (Fig. 17a), and the CO selectivity was almost 100%. In the photocatalytic CO_2 conversion reaction, the Mn single atom as the active centre was conducive to the accumulation of holes and accelerating the oxidation of H_2O (Fig. 17b). Simultaneously, the Co single atom was conducive to the adsorption of CO_2, thereby accelerating the reduction of CO_2 to CO by electrons (Fig. 17c). To enhance our understanding of SAC mechanisms, density functional theory (DFT) simulations can be advantageous. Nevertheless, if the active centre of the catalyst does not align with the actual active centre, theoretical applications become limited.[78,80,299] Therefore, it is crucial to further investigate *in situ* characterization methods for SACs and achieve their controllable preparation, particularly double or multiple single-atom photocatalysts, to advance sustainable development.

The formation of the high-value-added product CH_4 typically involves a multi-electron reaction. To facilitate the production of the desired product through this multi-electron reaction, it is essential to accumulate a sufficient number of photogenerated electrons at the reactive site. Noble metals, non-metallic impurities, and vacancy defects in photocatalysts can serve as electron sinks to provide an ample supply of electrons for selective product generation.[79,81,314] For example, Wang *et al.*[300] loaded ultrafine Pt nanoparticles on SiC nanosheets, and found that the ultrafine Pt nanoparticles (∼1.8 nm) captured (Fig. 18a–d) and accumulated photogenerated electrons in SiC nanoparticles to promote the 8-electron reaction to produce CH_4. Simultaneously, the CO produced by the 2-electron reaction was chemically absorbed by Pt NPs, and the high-energy electron SiC NSs provided by Pt NPs triggered further CH_4 generation from Pt–CO (Fig. 18e). The CH_4 selectivity of the designed 2 wt% Pt/SiC NSs reached 96.79%. In addition, this study also found that the proton provided by the H_2O oxidation half-reaction played a role in the formation of CH_4, and the surface modification increased the CO_2 adsorption and activation sites, enhanced the light absorption, and accelerated the charge separation. Li *et al.*[301] designed a series of chlorine-modified Bi_2WO_6 nanosheets to study the effect of protons produced by H_2O oxidation on CH_4 generation. The results showed that the selectivity for CH_4 was regulated by the chloride loading and reached up to 94.98% at the optimum loading. Further intermediate product studies and density functional theory calculations also confirmed that the Cl^- on Bi_2WO_6 nanosheets not only promoted the oxidation of H_2O but also reduced the energy barrier generated by the intermediate *CHO, thus promoting the formation of CH_4 (Fig. 18f and g). Xu *et al.*[302] studied carbon nitrogen bromide (CNBr) (Fig. 19a). They found that it could stably and efficiently photocatalyze the reduction of CO_2 to CH_4 with a selectivity of 70.27%. In their synthesized catalysts, the Br

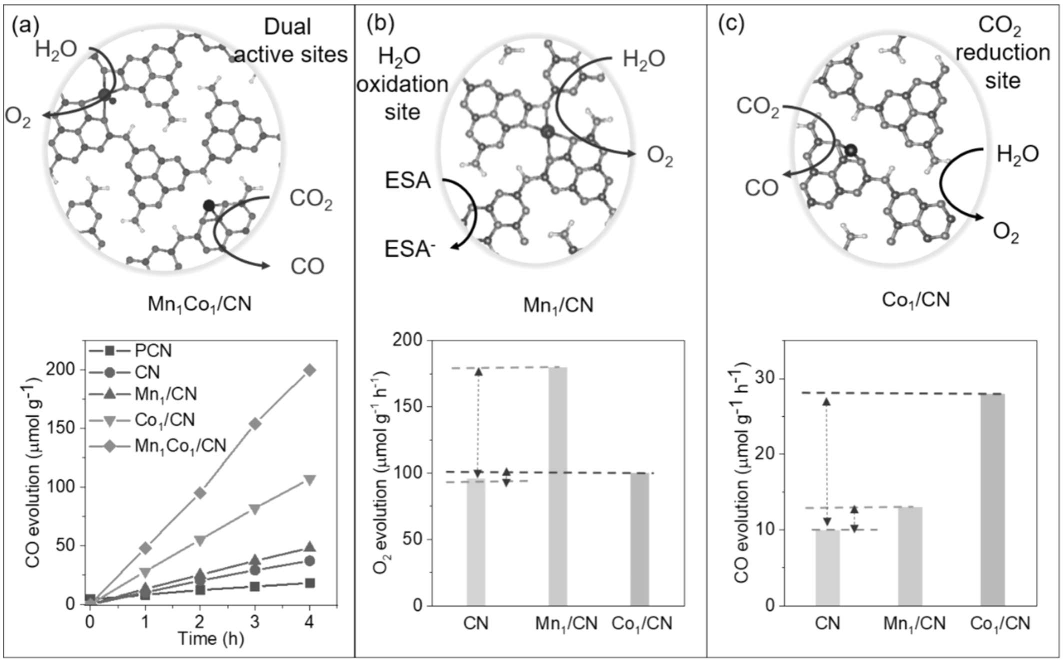

Fig. 17 (a) Photocatalytic CO yield diagram of bimetallic single-atom Mn and CO on CN. (b) Effects of single atoms of Mn and CO on CN in the photocatalytic oxidation of H_2O. (c) Effects of single atoms of Mn and CO on CN in photocatalytic CO_2 reduction. Reproduced from ref. 291 with permission from [Wiley Online Library], copyright [2022].

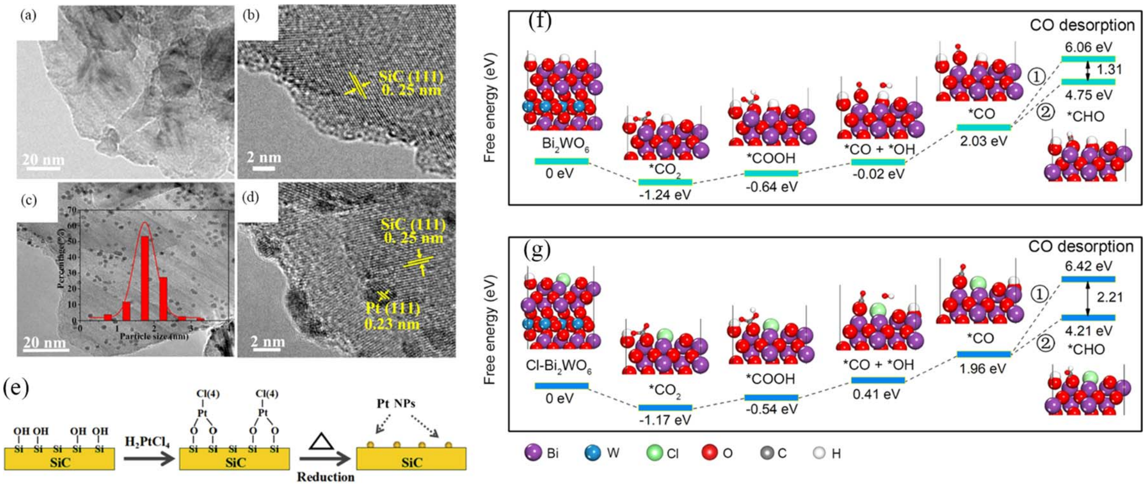

Fig. 18 (a–d) TEM images of ultrafine SiC nanoparticles. (e) Diagram of loading Pt nanoparticles on SiC nanosheets. (f and g) DFT calculation, free energy diagrams for Bi_2WO_6 and Cl–Bi_2WO_6, respectively. (a–e) Reproduced from ref. 300 with permission from [Elsevier], copyright [2020]. (f and g) Reproduced from ref. 301 with permission from [ACS Publications], copyright [2020].

atom supplanted the N atom within the tri-*s*-triazine units, thereby enhancing the local charge separation. The presence of Br acted as an active site, drawing CO_2 to the surface of the catalyst. This facilitated the activation of adsorbed CO_2 by the locally generated photoelectrons, ultimately leading to CH_4 production through hydrogenation. Employing density functional theory (DFT) simulations, it was uncovered that the introduction of Br doping effectively diminished the energy barrier associated with the rate-determining step, thus accelerating the reaction dynamics. This led to an increase in the generation of *CHO species, subsequently boosting the selectivity for CH_4 production. Xiong *et al.*[303] designed defects by the hydrothermal treatment of CN, and then introduced Pt single atoms in the defect centre to improve the catalytic efficiency. The CH_4 formation rate of the Pt@Def-CN catalyst was 6.3 μmol g^{-1} h^{-1}, and the selectivity reached 97%. In contrast, the CH_4 formation rate of pure CN was only 0.3 μmol g^{-1} h^{-1} (Fig. 19b).

Feng *et al.*[304] used a surfactant-free sedimentary reduction method to deposit both Au and Pd metals on OV-rich TiO_2 (Fig. 19c), and they uncovered the significance of metal sites and semiconductor charge carriers in the integrated process of CO_2 reduction and H_2O oxidation. In particular, TiO_2 with an abundance of OVs enhanced water oxidation by supplying more protons. Subsequently, CO_2 and protons were activated at the Au@Pd interface, leading to the formation of surface-attached Au@Pd–$CO_2^{\bullet-}$ and Au@Pd–H intermediates. By regulating the proportion of Au@Pd–$CO_2^{\bullet-}$/Au@Pd–H through the modification of the Au@Pd nanoparticle ratio and OV concentration, the efficiency of the catalyst was optimized for oxygen and methane generation, achieving a remarkable CH_4 selectivity of 96%.

Our previous examples consistently demonstrate that the photocatalytic performance can be effectively enhanced through the precise regulation of the heterostructure. However, despite observing a significant increase in activity in all cases, no corresponding improvement in selectivity was observed. Unlike cocatalysts and dopants, it remains unclear whether manipulating the heterostructure can enhance the methane selectivity. This is because the study of photocatalytic materials containing heterojunctions is limited by the difficulty of accurately dealing with the complexity of the interface. Simultaneously, considering the complexity of the synthesis process, how to improve the stability of the reaction process is still

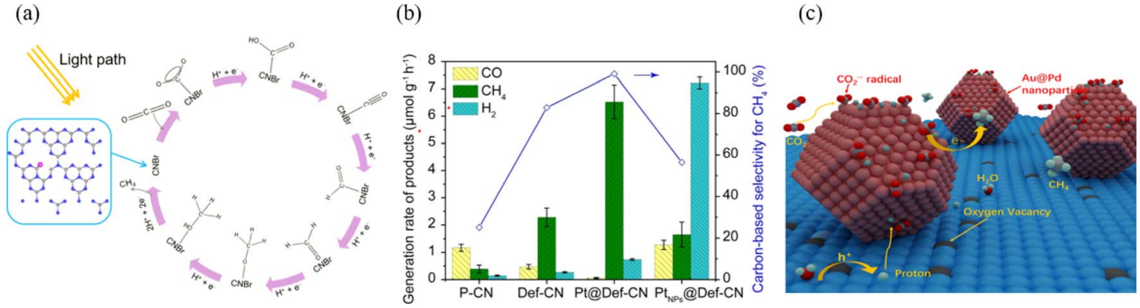

Fig. 19 (a) Reaction pathways of CO_2 photocatalyzed by CNBr. (b) Performance test of Pt@Def-CN catalyst. (c) Schematic diagram of Au and Pd deposition on OV-rich TiO_2 by deposition reduction method. (a) Reproduced from ref. 302 with permission from [Elsevier], copyright [2023]. (b) Reproduced from ref. 303 with permission from [Wiley Online Library], copyright [2022]. (c) Reproduced from ref. 304 with permission from [Elsevier], copyright [2019].

a difficult problem to solve. Therefore, other modification strategies can also be chosen, such as the construction of metal active sites, which is more advantageous than non-metal active sites, while dual or multiple active sites are more conducive to the reaction. In addition, the construction of surface defects may also have the corresponding acceleration effect on the adsorption of CO_2.[121]

4.1.2 CH_3OH.

CH_3OH is one of the most promising liquid products for CO_2 reduction, which facilitates fuel cell storage and transportation. Compared with CH_4, CH_3OH has higher added value and wider application and is a more ideal product of CO_2 reduction.[79,82,315] For example, CH_3OH is a precursor to many essential chemicals (aromatics, methane, methyl methacrylate, and fatty acid methyl esters).[316,317] Current studies have found that many catalysts can produce CH_3OH. However, the generation of CH_3OH involves a 6-electron process, thus necessitating an exceptionally prolonged carrier lifetime to facilitate electron accumulation for achieving selectivity. Table 3 lists the recent advances in the photocatalytic reduction of CO_2 with H_2O to produce CH_3OH. According to the reports in the literature, the highest activity for photocatalytic CO_2 reduction to produce CH_3OH in pure water systems reached 511.1 μmol g^{-1} h^{-1},[318] and the selectivity was close to 100%.[319] However, the inherent defects of a single photocatalytic material limit its full potential in photocatalytic activity. As shown in Table 3, researchers have explored various strategies such as ion doping, micro-morphology design, and defect regulation to optimize photocatalysts. Among the materials, carbon-based non-metallic materials such as graphene show great promise in the field of photocatalytic CO_2 reduction for methanol production. With unique surface properties and a textured structure, carbon-based non-metallic materials not only demonstrate excellent photocatalytic activity but can also be used as a cocatalyst for combination with other semiconductors to improve their overall performance. Additionally, carbon-based non-metallic materials offer advantages over semiconductors due to their cost-effectiveness and ease of preparation.

Most work still begins with the design of heterojunctions for the improvement of methanol production. For example, in the work by Ding *et al.*,[320] a composite catalyst was synthesized by integrating the conventional α-Fe_2O_3 with g-C_3N_4, aiming to establish a Z-scheme heterojunction. This integration facilitated the separation of photogenerated electrons and holes, thereby enhancing the efficiency of the catalyst. At a specific ratio of α-Fe_2O_3 to g-C_3N_4 of 4 : 6, the designed catalyst demonstrated a peak CH_3OH generation rate of 5.63 μmol g^{-1} h^{-1}, with a near-perfect selectivity of nearly 100% (Fig. 20a). Wang *et al.*[321] combined two different Bi-based catalysts, $BiVO_4$ and $Bi_4Ti_3O_{12}$, to form a heterojunction, enhancing the capability of electron–hole pair separation, significantly boosting the photocatalytic efficiency for CO_2 reduction with H_2O to produce CH_3OH and CO. Specifically, the catalyst performance was optimal when 10% $Bi_4Ti_3O_{12}$ was incorporated, yielding CH_3OH and CO at 16.6 μmol g^{-1} h^{-1} and 13.29 μmol g^{-1} h^{-1}, and these figures represented a 12.39-fold and 5.68-fold increase compared to pristine $BiVO_4$, and a 9.88-fold and 2.8-fold improvement over pure $Bi_4Ti_3O_{12}$, respectively (Fig. 20b).

Zhou *et al.*[322] proposed a new concept of providing sufficient protons for activated H_2O without producing strong oxidizing radicals to achieve the highly selective photocatalytic reduction of CO_2 and H_2O to CH_3OH. They loaded cobalt sulphide on carbon nitride and found that cobalt sulphide significantly weakened the overpotential of H_2O oxidation and promoted the formation of protons without forming strong oxidation radicals such as $^{\bullet}OH$ and $^{\bullet}O_2^-$. Thus, the directed activation of H_2O promoted the sequential coupling of multiple protons/electrons with CO_2 to form the vital intermediates CHO^* and CH_3O^*, and finally increased the rate of CH_3OH formation to 97.3 μmol g^{-1} h^{-1} and the selectivity reached 87.2%.

Although the construction of heterojunctions can achieve the reduction of CO_2 to CH_3OH, their selectivity is unsatisfactory, possibly because electrons are not transferred quickly enough to the key intermediates CHO^* and CH_3O^* to participate in the reaction. Based on this, many researchers began to investigate metal doping. Hou *et al.*[323] developed a new flower-

Table 3 Summary of the photocatalytic systems for CO_2 reduction with H_2O to produce CH_3OH

Catalyst	Light source	Production/μmol g^{-1} h^{-1}	Selectivity	Reference
Co/g-C_3N_4 SAC	300 W Xe lamp	235.5	96.2%	257
2Re–In_2O_3	300 W Xe lamp	265.5	100%	317
Pr_1–N_4O_2/CN	300 W Xe lamp	511.1	92.4%	318
$Cu_xIn_5S_8$–Cu_ySe	300 W Xe lamp	5.25	∼100%	319
α-Fe_2O_3/g-C_3N_4	300 W Xe lamp	5.63	∼100%	320
$BiVO_4$/$Bi_4Ti_3O_{12}$	300 W Xe lamp	16.6	78.9%	321
C_3N_4–CoS	300 W Xe lamp	97.3	87.2%	322
BiOBr/La	300 W Xe lamp	63.12	92.4%	323
Ti-WO_3	300 W Xe lamp	16.8	88.9%	324
o-$BiVO_4$	300 W Xe lamp	398.3	∼100%	325
^{m}CD/CN	300 W Xe lamp	13.9	99.6%	326
CdS/Al_2O_3	10 W LED lamp	144.5	—	327
Bi_2S_3/CeO_2	300 W Xe lamp	168.35	—	328
Fe_3O_4@ZrO_2@TiO_2	400 W Xe lamp	301.29	—	329
Fe@TiO_2/$SrTiO_3$	300 W Xe lamp	154.20	98.9%	330
In_2O_3–WO_3	355 nm laser beam	496	—	331

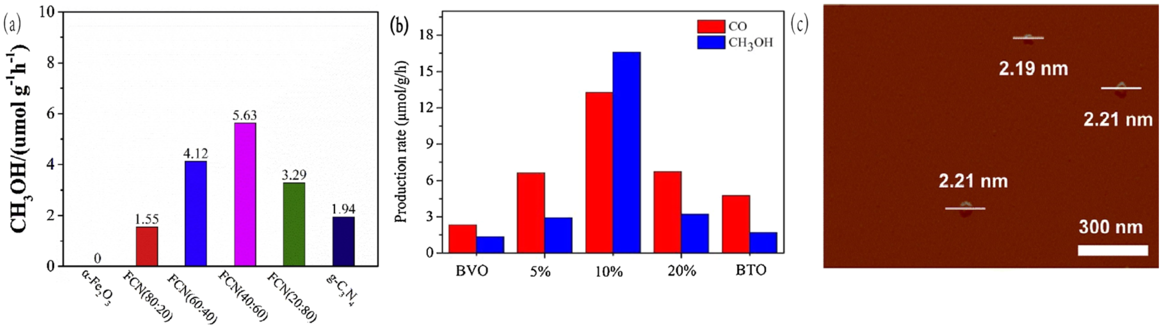

Fig. 20 (a) Photocatalytic CO_2 reduction activity of α-Fe_2O_3/g-C_3N_4 heterojunction. (b) Measurement of CO_2 reduction yield by photocatalysis with different ratios of $BiVO_4/Bi_4Ti_3O_{12}$ heterojunction. (c) AFM of Ti-doped WO_3 ultra-thin nanosheets. (a) Reproduced from ref. 320 with permission from [Elsevier], copyright [2019]. (b) Reproduced from ref. 321 with permission from [Elsevier], copyright [2020]. (c) Reproduced from ref. 324 with permission from [the Royal Society of Chemistry], copyright [2022].

like catalyst, La/BiOBr, by doping La into BiOBr and adjusting its morphology. This modification expanded the photoresponse range of the original BiOBr and diminished the recombination of photogenerated electron–hole pairs. The introduction of La^{3+} ions facilitated the migration of electrons residing in the conduction band of BiOBr to La^{3+}, enhancing their lifetime and reducing the charge recombination rate, ultimately boosting the production of CH_3OH. The reported yield of CH_3OH in this investigation was 63.12 μmol g^{-1} h^{-1}, accompanied by a selectivity of 88.9%. In the work by Xie *et al.*,[324] an innovative approach was employed to synthesize ultrathin nanosheets with the integration of Ti atoms in the WO_3 structure (Fig. 20c). The reported methanol formation rate for this composite was 16.8 μmol g^{-1} h^{-1}, a significant enhancement of 3.3 times compared to the undoped WO_3 nanosheets. Impressively, the selectivity towards methanol achieved an outstanding 88.9%. Besides, Xie *et al.*[325] used hexadecyl trimethyl ammonium bromide to construct vanadium vacancies on $BiVO_4$ and synthesized Vv-rich and Vv-poor with the one-unit-cell thickness *o*-$BiVO_4$ atomic layers (Fig. 21a). The improvement in light absorption capacity was due to the construction of new defects and the increase in vacancy concentration. The one-unit-cell *o*-$BiVO_4$ layer with abundant vanadium vacancies had a high surface photovoltage intensity,

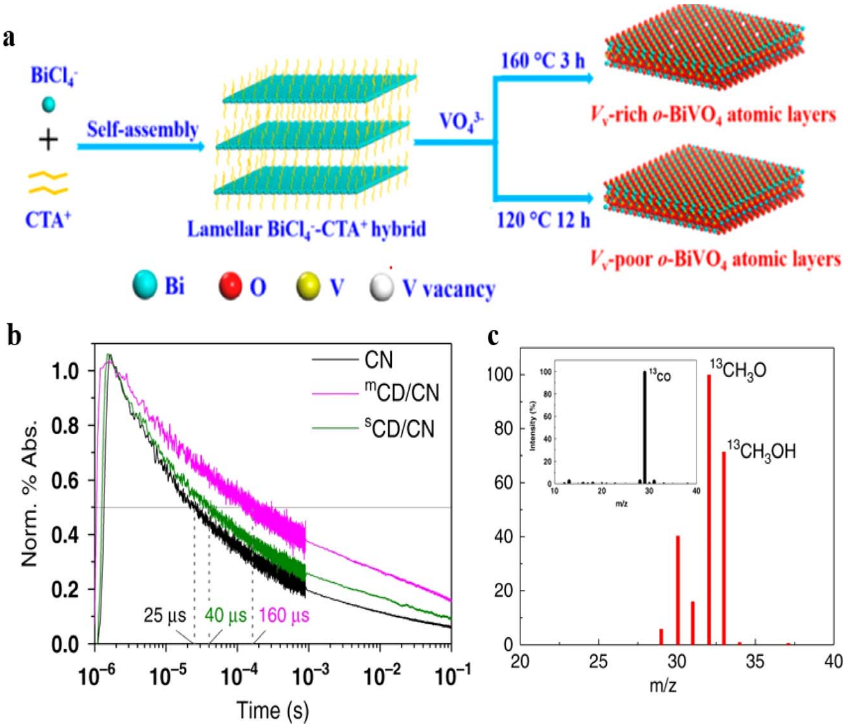

Fig. 21 (a) Schematic of the synthesis of a Vv-rich and Vv-poor *o*-$BiVO_4$ atomic layer with a single cell thickness. (b) Comparison of electron lifetime of CN ^{m}CD/CN and sCD/CN. (c) Mass spectra of the products after $^{13}CO_2$ photoreduction. (a) Reproduced from ref. 325 with permission from [ACS Publications], copyright [2017]. (b and c) Reproduced from ref. 326 with permission from [Nature Publishing Group], copyright [2020].

which ensured its high carrier separation efficiency, and thus increased the CH_3OH generation rate to 398.3 μmol g^{-1} h^{-1}. To further enhance the selectivity for methanol, Tang *et al.*[326] employed a microwave method for synthesizing carbon nitride (CN) modified with carbon dots (^{m}CD). This ^{m}CD possessed unique hole-accepting properties, which could prolong the electron lifetime of CN by six times, thereby facilitating the generation of the $6e^-$ product CH_3OH in the CO_2 reduction reaction (Fig. 21b). The CH_3OH selectivity approached 100%, and the internal quantum efficiency in the visible light region reached 2.1%, as evidenced by the transient absorption spectrum and isotope labelling, as shown in Fig. 21c. These ^{m}CD could rapidly extract holes from CN, preventing the surface adsorption of methanol and promoting water oxidation on methanol, thus enhancing the selectivity of CO_2 reduction to alcohol. This study presented a novel strategy for efficiently and selectively reducing carbon dioxide into high value-added chemicals using water.

At present, SACs have become a popular modification strategy because of their high atomic utilization. Thus, Zhou *et al.*[332] prepared Co/g-C_3N_4 SACs *via* pyrolysis, and the load of Co atoms on their surface was as high as 24.6 wt%. The CH_3OH generation rate was increased to 235.5 μmol g^{-1} h^{-1} with a selectivity of 96.2%. Their discovery revealed that an extraordinarily high concentration of individual cobalt atoms was firmly situated on the surface of g-C_3N_4, forming a Co–N_2C configuration, where each Co atom was bonded with two nitrogen atoms and one carbon atom. These evenly dispersed Co–N_2C sites had dual functions, serving both as electron accumulation hubs and as locations for CO_2 absorption and activation. Compared with other catalyst modification measures, SACs still have a great advantage in the photocatalytic CO_2 reduction to CH_3OH. It can be seen that the design on the molecular or atomic scale of catalyst modification is more favourable for improving the photocatalytic performance.

4.1.3 HCOOH. In the process of CO_2 reduction, HCOOH is one of the important intermediates, and most of the products from CO_2 reduction need to go through the HCOOH intermediate. HCOOH is also an important chemical raw material, which can be used as a hydrogen storage material. On an industrial scale, HCOOH is mainly produced from methyl formate, which is synthesized from CH_3OH and CO in the presence of strong salts and bases. Therefore, it is highly desirable to develop environmentally friendly and sustainable processes for HCOOH production through CO_2 conversion using solar, wind, and/or hydroelectric power sources.[333]

Although photocatalytic CO_2 reduction to HCOOH is a dynamic favourable process with double electron transfer, the efficiency and selectivity of the photocatalyzed CO_2 to HCOOH are not high at present. Most catalysts need to reduce CO_2 to HCOOH under certain conditions, and pure CO_2 is not suitable as a good carbon source. Typically, bicarbonate is used as a carbon source and a sacrificial agent is added to convert it into HCOOH. Therefore, how to efficiently convert CO_2 into HCOOH is a major challenge at present. Table 4 lists the recent advances in the photocatalytic reduction of CO_2 with H_2O to HCOOH product.

As can be seen in Table 4, although many modification strategies have been employed to expand the light absorption, accelerate the charge carrier separation, and promote CO_2 adsorption and activation, without the addition of a sacrificial agent or photosensitizer, only low-value gas products have been produced. At present, the highest activity reported for the photocatalytic CO_2-induced HCOOH production is 896.7 μmol g^{-1} h^{-1}.[334] In recent years, metal oxides, graphene, sulphides, *etc.* have been widely explored to promote charge separation by forming Schottky or Z-scheme heterojunctions to improve the CO_2 reduction reaction performance. However, the photocatalytic activity for HCOOH production is not ideal. An increasing number of researchers have begun to look at MOF photocatalysts to improve the photocatalytic performance, because MOFs can be endowed with clear and isolated sites to anchor the catalytic substance compared to other solid carriers with non-uniformly dispersed sites. Zhang *et al.*[335] developed a CuO/Ag/UiO-66 Z-type heterojunction composite catalyst and investigated the impact of Ag additive on enhancing the selectivity for CO_2 reduction. Comparative studies were conducted on CuO, CuO/UiO-66, and CuO/Ag/UiO-66. Pure CuO primarily produced CH_3OH. Upon the formation of the CuO/UiO-66 heterostructure, HCOOH was observed as the main product. However, with the addition of Ag, the selectivity significantly increased from 63% to 95.9% (Fig. 22a). This is probably the highest selectivity achieved without the use of sacrificial agents in liquid-phase photocatalytic CO_2 reduction. This enhancement was attributed to the highly dispersed Ag acting as an electron transport medium in the CuO/Ag/UiO-66 Z-type

Table 4 Summary of the photocatalytic systems for CO_2 reduction to produce HCOOH

Catalyst	Light source	Production/μmol g^{-1} h^{-1}	Selectivity	Reference
CuZn/$SrTiO_3$	Hg Xe lamp (240–300 nm)	8	75%	333
Cu_2O–Pt/SiC/IrO_x	300 W Xe lamp	896.7	—	334
CuO/Ag/UiO-66	300 W Xe lamp	63	95.9%	335
NH_2–C@Cu_2O	Al Kα (1486.6 eV, 250 W)	138.65	92%	336
Pt/In_2O_3/g-C_3N_4	3 W LED light (420 nm)	63.1	90.1%	337
g-C_3N_4/Cu–TiO_2	Visible light	2534.5	—	338
Cu@Cu_2O/C-350	300 W Xe lamp	81.58	—	339
PCN-222/$CsPbBr_3$ QDs	300 W Xe lamp (420 nm)	189.9	~100%	340
Ir SACs/NH_2-UiO-66	300 W Xe lamp	3.38	96.3	341

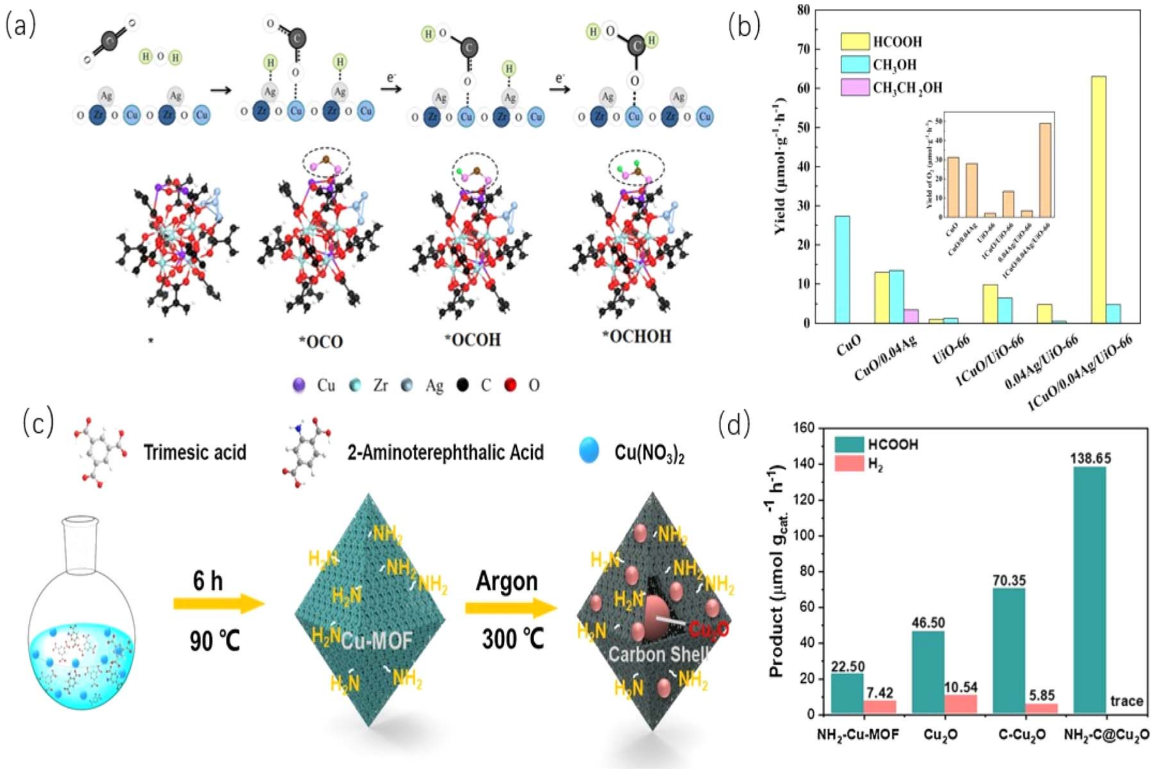

Fig. 22 (a) Adsorption model of CO_2 on CuO/Ag/UiO-66 catalyst. (b) Activities of pure CuO, UiO-66, CuO/UiO-66 and heterojunction CuO/Ag/UiO-66. (c) Schematic diagram of the preparation of NH_2–C@Cu_2O photocatalyst by low temperature carbonization method. (d) Yield test diagram of NH_2–C@Cu_2O photocatalytic CO_2 reduction. (a and b) Reproduced from ref. 335 with permission from [Elsevier], copyright [2022]. Reproduced from ref. 336 with permission from [the Royal Society of Chemistry], copyright [2023].

heterojunction to facilitate the efficient transport and separation of photogenerated electrons. Simultaneously, the *in situ* infrared characterization and theoretical calculations also demonstrated that Ag exhibits strong adsorption capacity for *H protons, favouring their combination with the CO_2 primary activation intermediate *OCO through oxygen coordination at nearby sites (Fig. 22b). This led to the generation of the formic acid intermediate *OCOH, and ultimately resulted in highly selective formic acid products. These findings highlight how Ag effectively modulates the CO_2 reduction pathway by regulating the reactive intermediate species.

Li *et al.*[336] synthesized a metal–organic skeleton (MOF) precursor material (–NH_2–Cu-MOF) to enhance the CO_2 adsorption and improve the long-term stability of the catalyst (Fig. 22c). The method adopted a low-temperature carbonization process (300 °C) to synthesize the –NH_2 carbon skeleton-modified Cu_2O photocatalyst. In this study, acid–base neutralization was utilized to enhance the adsorption of –NH_2 on the acidic CO_2, thereby activating –NH_2 as the active centre. Moreover, the introduction of amino functional groups served as an electron-withdrawing agent, thereby significantly inhibiting carrier recombination. Simultaneously, the unordered *in situ* carbon network originating from the organic ligands played a protective role in preventing Cu_2O from photo-corrosion. Consequently, this led to improved selectivity and productivity in the conversion of CO_2 to HCOOH. The achieved formic acid yield increased to 138.65 $\mu mol\ g^{-1}\ h^{-1}$ (Fig. 22d), which was three-times higher than that achieved with pure Cu_2O. These findings demonstrated that modifying Cu_2O with an –NH_2-modified carbon skeleton offers a novel approach for designing efficient and stable photocatalysts. Li *et al.*[337] developed a Pt/In_2O_3/g-C_3N_4 multifunctional catalyst *via* the controlled assembly method. This catalyst produced H atoms through water splitting, adsorbed and activated CO_2 molecules, and inhibited the recombination of photogenerated electrons and holes by accelerating the electron transfer and forming a heterojunction. Thus, it showed high activity and selectivity for HCOOH in the photocatalytic CO_2 reduction process driven by visible light.

Plasmonic metals display outstanding photocatalytic activity in the visible region due to their surface plasmon resonance effect for CO_2 reduction, which is attributed to their generation of hot electrons. Among the ionized metals such as Au, Ag, and Cu nanocrystals, Cu-based catalysts have attracted significant attention in the field of plasma catalysis due to their abundant reserves and cost-effectiveness. Saidina Amin *et al.*[338] loaded Cu onto g-C_3N_4 and TiO_2 (Fig. 23). In the process of catalyst treatment, Cu was easily oxidized to form CuO, and thus formed ternary heterojunctions. The electrons on the loaded Cu were transferred to CuO, and thus the CO_2 adsorbed on the active sites obtained electrons to produce CH_3OH and HCOOH. In the designed catalyst, enhancements in both photocatalytic activity and product specificity were achieved through strategic manipulation of the g-C_3N_4 to Cu–TiO_2 proportion. At a balance

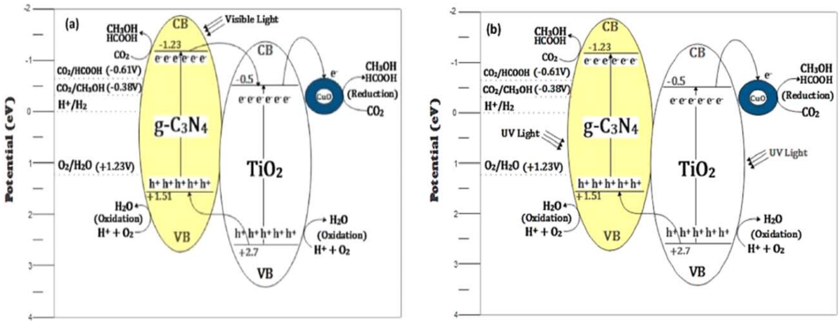

Fig. 23 Schematic reaction mechanism of g-C_3N_4/Cu/TiO_2 composites for the reduction of CO_2 to CH_3OH and HCOOH under UV light (b) and visible light. (a). Reproduced from ref. 338 with permission from [Elsevier], copyright [2017].

of 30% g-C_3N_4 and 70% Cu–TiO_2, the system demonstrated a superior performance with the CH_3OH and HCOOH production rates reaching 1287 μmol g^{-1} h^{-1} and 2534.5 μmol g^{-1} h^{-1}, respectively. Li *et al.*[339] successfully employed a Cu-MOF precursor to synthesize homogeneous core–shell nanoparticles consisting of a Cu_2O shell coated with a Cu core. The surface Cu_2O shell served as the active site for the adsorption and activation of CO_2 molecules, while the heterojunction between the plasma Cu and Cu_2O facilitated efficient photoelectron transport to the adsorbed CO_2 molecules. In the absence of any additives, the composite catalyst of Cu@Cu_2O/C-350 demonstrated photocatalytic reduction of CO_2 to HCOOH with a yield of 67.35 μmol g^{-1} h^{-1}. This study paved the way for developing cost-effective copper-based photocatalysts. According to previous studies, it is clear that the photocatalytic reduction of CO_2 to HCOOH remains a significant challenge at present. Among the various strategies, constructing heterojunctions has emerged as a common approach. Additionally, band gap engineering can modulate the band structure of photocatalysts to match the desired reduction potential for CO to HCOOH (−0.61 V).

For instance, in the work by Murugesan *et al.*,[16] the successful construction of a direct Z-scheme heterostructure involving AgCl/g-C_3N_4 was accomplished, resulting in a remarkable selectivity of 88.9% for CO_2 to HCOOH. Nonetheless, this approach struggles to hinder other thermodynamically more favourable reactions, such as the conversion of CO_2 to CH_3OH (−0.38 V). Moreover, the integration of organic sacrificial agents, including methanol, ethanol, triethanolamine, trimethylamine, and ethylenediaminetetraacetic acid, is instrumental in exhausting the photogenerated holes, enhancing the electron–hole separation, and supplying protons for *H reduction in CO. For instance, Hao *et al.*[18] utilized isopropyl alcohol as a sacrificial agent within MOF membranes (Ir SACs/NH_2-UiO-66). Nevertheless, it should be noted that the addition of these reagents inevitably complicates the product separation and increases the expense of photocatalytic CO_2 emission reduction, which contradicts the advantages of green photocatalytic systems and hinders clean energy applications. Therefore, there is an imperative need to explore universal approaches for achieving the highly selective production of HCOOH through photocatalytic CO_2.[337]

4.2 C_2 and C_{2+} products

In the series of products of CO_2 reduction, C_2 and C_{2+} products have higher added value compared with other products. However, only a few catalyst systems can produce C_2 products. Moreover, most of the C_2 products produced are additional products rather than the main product, and the yield is very low. The photocatalysis of CO_2 with H_2O to produce high-yield and selective C_2 products is a major challenge using the current catalytic systems.[54,120] Present investigations emphasize that obtaining C_2 and C_{2+} compounds relies on minimizing the recombination of photogenerated electrons and holes, while augmenting their separation efficiency within the catalyst. Additionally, an effective catalyst must possess robust capabilities for C–C bonding.[342,343] As shown in Table 5, we summarized the recent progress in photocatalytic CO_2 reduction with H_2O, leading to the formation of C_2 and C_{2+} derivatives. As can be seen in Table 5, there are few studies on C_2 products at present. Regarding the reported photocatalysts, the yield of C_{2+} products formed by photocatalytic CO_2 reduction with H_2O as the reducing agent is generally low, and most of them have low selectivity. Among them, the peak efficiency in the photocatalytic conversion of CO_2 into C_2H_6 stands at an impressive 38.2 μmol g^{-1} h^{-1}.[344] Predominantly, researchers opt for metal oxides as photocatalysts due to their excellent stability. However, unmodified photocatalysts often encounter constraints stemming from swift carrier recombination and an incompatible energy band structure, necessitating their enhancement through modification. Chen *et al.*[345] fabricated Ni nanocluster-embedded black TiO_2 (Ni/TiO_2(OVs)) photocatalysts with integrated dual active sites through a strategy that merged metal support and surface defect architectures. The combination of Ni nanoclusters and oxygen vacancies (OVs) not only established a fast electron transfer pathway, but also the band gap was reduced to enhance the response to visible light. The Ni/TiO_2(OV) photocatalyst possessed stable CO_2 binding sites and the lowest activation energy (0.08 eV), which improved the product selectivity and enhanced the photocatalytic activity. The principal output was CH_3CHO with a production rate of 1.67 μmol g^{-1} h^{-1}, an output 18 times greater than that achieved by the commercial TiO_2. Tatsumi Ishihara and collaborators aimed to transform CO_2 into C_2 compounds by

Table 5 Summary of the photocatalytic systems for CO_2 reduction with H_2O to produce C_2

Catalyst	Light source	Production/μmol g^{-1} h^{-1}	Selectivity	Reference
Au_1/RP	300 W Xe lamp	C_2H_6 1.32	96%	342
Hydrogenated $SrTiO_3$	Ultraviolet lamp (8 W)	C_2H_2 6.5	76%	343
$Cd_{0.8}Zn_{0.2}S/In_2O_3$	300 W Xe lamp	C_2H_6 38.2	82.6%	344
Ni/TiO_2(OVs)	300 W halogen lamp	CH_3CHO 1.67	—	345
$WO_3 \cdot 0.33H_2O$ nanotube	Solar light	CH_3COOH 9.4	85%	346
$Cu^{\delta+}/CeO_2–TiO_2$	300 W Xe lamp (320–850 nm)	C_2H_4 4.51	73.9%	347
$CuGaS_2$@CuO	450 W Xe lamp (with UV cut-off filter)	C_2H_4 20.6	75.1%	348
P/Cu SAs@CN	300 W Xe lamp	C_2H_6 616.6	—	349
ZSM-5@NiV_2Se_4	300 W Xe lamp	C_2H_6 1.85	90.1%	350
$Bi_{19}S_{27}Cl_3$	420 W Xe lamp	CH_3CH_2OH 5.19	85%	351
AuIr@GaN	300 W Xe lamp	C_2H_6: 58 800	5.6%	352
CuO_x@p-ZnO	300 W Xe lamp	C_2H_4 2.7	32.9%	353
Pd–Co_3O_4	300 W Xe lamp	CH_3COOH 13.8	100%	354

surmounting the energy barrier associated with multiple-electron transfer. In their approach,[346] OVs played a crucial role in capturing a substantial quantity of electrons to overcome this energy barrier. However, due to the unstable OVs, low concentration and easy oxidation on the surface, they designed ultrathin $WO_3 \cdot 0.33H_2O$ nanosheets with a large number of stable OVs (Fig. 24a), which could stably and efficiently convert CO_2 into CH_3COOH by using water as the oxidant under visible light. The yield reached 9.4 μmol g^{-1} h^{-1}, and the selectivity reached 85%. In the work by Huang *et al.*,[347] an interface-modification approach was employed to construct a $Cu^{\delta+}/CeO_2–TiO_2$ photocatalyst, featuring $Cu^{\delta+}$ sites uniformly distributed across $CeO_2–TiO_2$ heterostructures (Fig. 24b). This novel photocatalyst exhibited a remarkable enhancement in

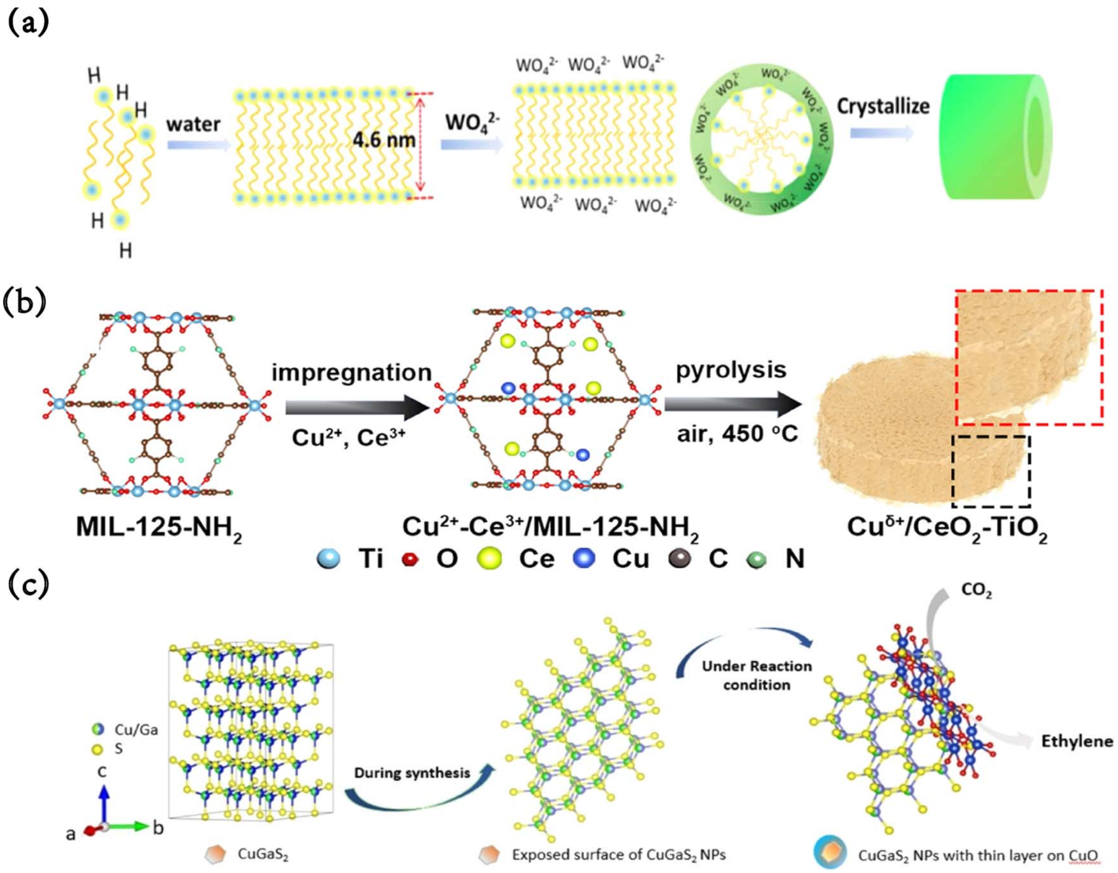

Fig. 24 (a) Schematic illustration of the hydrothermal procedure for the synthesis of oxygen-deficient hydrated $WO_3 \cdot 0.33H_2O$ nanotube. (b) Schematic diagram of the construction of $Cu^{\delta+}/CeO_2–TiO_2$ photocatalyst. (c) Simulation of CuO *in situ* on the upper surface of wurtzite phase of $CuGaS_2$. (a) Reproduced from ref. 346 with permission from [ACS Publications], copyright [2018]. (b) Reproduced from ref. 347 with permission from [ACS Publications], copyright [2022]. (c) Reproduced from ref. 348 with permission from [Wiley Online Library], copyright [2023].

both efficiency and selectivity for C_2H_4 production, reaching 4.51 μmol g^{-1} h^{-1} and 47.5%, respectively. These figures represented a 2.36-fold and 1.32-fold improvement in that by the $Cu^{\delta+}/TiO_2$ catalyst, respectively. Peter *et al.*[348] proposed that surface restructuring facilitated C–C bonding in the CO_2-to-C_2H_4 conversion process. The *in situ* formation of wurtzite phase $CuGaS_2$ occurred on the catalyst surface, accompanied by the development of a thin CuO layer atop the initial catalyst (Fig. 24c). Consequently, CO_2 was effectively transformed into C_2H_4 with a high selectivity of 75.1% and a yield of 20.6 μmol g^{-1} h^{-1}.

Some noble metals can enrich electrons, and single atoms can be used as catalytic active sites. In the work by Li *et al.*,[342] they dispersed individual Au atoms onto red phosphorus (Au_1/RP). The electronically rich phosphorus atoms adjacent to these Au single atoms served as active sites for CO_2 activation, as illustrated in Fig. 25. This configuration notably diminished the energy barrier for C–C bonding, thereby enhancing the kinetic process of C_2H_6 formation. Consequently, Au_1/RP exhibited a C_2H_6 selectivity of 96% and activity of 1.32 μmol g^{-1} h^{-1}, which was achieved without the use of a sacrificial agent. Mao *et al.*[349] developed a photocatalyst consisting of dual P and Cu sites integrated on g-C_3N_4 (P/Cu SACs@CN). This innovative design resulted in an impressive C_2H_6 generation rate of 616.6 μmol g^{-1} h^{-1} during the conversion of CO_2 into hydrocarbons. This research highlighted that the presence of a dual-site structure on the surface of g-C_3N_4 played a pivotal role in the effective conversion of CO_2 into multi-carbon compounds. The kinetic study of charge carriers also showed that the multi-electron transfer process for CO_2 reduction, attributed to the electron and hole trapping sites of the Cu and P double sites in the CN matrix, promoted the formation of charge-rich Cu sites, endowing the P/Cu SAC@CN photocatalysts with excellent charge separation capability.

According to the available studies, evidently all elements contribute to electron and proton accumulation, including elevated photon intensity and energy, presence of co-catalysts and reduced charge recombination, which positively impact the generation of C_2 and higher carbon compounds. From doping nonmetals to metals and building single atoms to building double active sites, catalysts tend to be designed for active sites.

Therefore, more catalyst designs are not satisfied with a single method but use multiple strategies for simultaneous modification such as doping metal or non-metal and surface defect construction. Recent studies have also shown that the presence of both can indeed improve the selectivity for C_2 products; however, they also increase the difficulty of explaining the formation mechanism.

In addition, long-term stability is essential for the practical application of photocatalytic CO_2 reduction. However, most photocatalytic materials are prone to deactivation during reduction reactions. Furthermore, the development of the stable photocatalyst materials for CO_2 reduction still faces great challenges. This, many studies have been devoted to addressing this issue. Some approaches have been studied to improve the stability of photocatalytic CO_2 reduction reaction systems. Photocatalytic CO_2 reduction can usually be performed in highly polar (*e.g.*, dimethylformamide (DMF), dimethyl sulfone (DMSO), and acetonitrile (ACN)), medium polar (*e.g.*, ethyl acetate (EA) and tetrahydrofuran (THF)), and low polar (*e.g.*, ether and toluene) reaction media. However, semiconductors such as halide perovskites are severely unstable when exposed to water, highly polar hydrophobic solvents, oxygen, light, and heat. This is because they have strong ionic properties, making them vulnerable to damage upon contact with polar reaction media. Consequently, they immediately degrade into other structures, and thus choosing the appropriate reaction medium can improve their stability.[355] Also, a protective layer is designed to encapsulate unstable semiconductors to prevent their degradation due to various factors such as photocorrosion and strong acids and bases. Li *et al.*[356] reported the synthesis of a double-doped $CsPbCl_3$ nanocrystal (NC) with core–shell structure as a CO_2 reduction photocatalyst. Due to the size difference between the dopant and bulk ion, surface segregation occurs during the process of elastic stress relaxation. Based on the surface segregation effect, a solid BI-rich shell could be constructed to give the $CsPbCl_3$ NCs a stable crystal structure and morphology. The core–shell double doped $CsPbCl_3$ nanocrystal structure maintained the initial photocatalytic efficiency of 97% without changes in its structure, morphology and size under a harsh environment such as strong irradiation and high humidity. Ziarati *et al.*[357] synthesized a three-dimensional core–shell TiO_{2-x}/LDH photocatalyst through three steps including

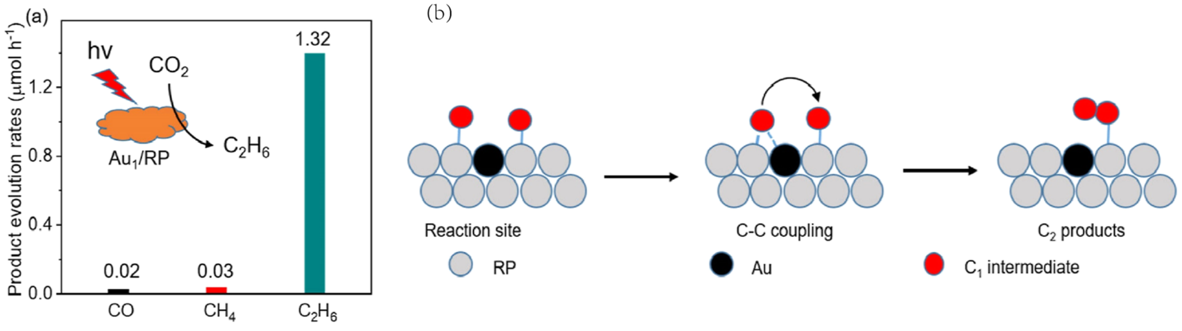

Fig. 25 (a) CO_2 reduction yield of Au_1/RP photocatalysis. (b) Diagram of implanting single-atom Au reaction intermediates on red phosphorus. (a and b) Reproduced from ref. 342 with permission from [ACS Publications], copyright [2022].

solvothermal, hydrogen treatment and hydrothermal reaction. This structure reveals high efficiency for the photoreduction of carbon dioxide into a solar fuel in the absence of a precious metal co-catalyst. The CH_4 yield increased gradually with the extension of the reaction time, and still reached 63 μmol g^{-1} h^{-1} after 12 h illumination. It was concluded that the core–shell photocatalyst avoids the spontaneous movement of surface dispersed particles through space interaction and isolation, and effectively improves the thermal stability and service life of the composite catalyst. However, in practical applications, is necessary to consider the fact that the encapsulation layer should not affect the photo-adsorption efficiency and mass transfer capacity of the semiconductor itself while playing the role of a protective layer.

5 Conclusion and perspective

The use of semiconductor materials and solar photocatalytic reduction of CO_2 to synthesize hydrocarbon fuels is currently one of the ideal models for purifying the environment and the renewable utilization of carbon resources. Herein, we reviewed the common strategies for the design of photocatalysts for CO_2 reduction in recent years, including defect construction, cocatalyst loading, doping, heterojunction formation, single-atom engineering, and surface organometallic catalysis. These modification methods boost the efficiency of electron and hole separation and migration, manipulate the electronic and energy band configuration, and strengthen the capability to adsorb CO_2 to improve the CO_2 reduction performance and regulate the product selectivity. Currently, photocatalysis technology has made some progress and breakthroughs in cleaning the environment and converting solar energy into renewable energy sources through the efforts of researchers around the world. However, given that photocatalysis is a complex reaction process, there are still some bottlenecks in CO_2 photoreduction technology, as follows: (1) the product activity is low. (2) The unclear reaction path and intermediates lead to inaccurate regulation of the final target products. (3) At present, the main reduction products mainly consist of CO and CH_4, where it is difficult to generate multi-carbon products. (4) The understanding of the catalytic reaction mechanism is still not thorough, such as the multi-scale migration and separation mechanisms of photogenerated charges, and the kinetics and mechanism of catalyst surface interface reaction, which limit the understanding of the catalytic reaction properties.

To break through these bottlenecks, it is necessary to develop new types of photocatalytic materials and study the basic issues in photocatalytic reactions, which is also the next development direction of photocatalysis. For the design of photocatalysts, researchers can continue to study the properties of the photo-absorption of the catalyst, the mechanism of photogenerated carrier separation and the tendency of migration to the surface, which are conducive to improving the photocatalytic efficiency. Based on the research results, we believe that some attempts and explorations can be made in the following three aspects. Firstly, dual cocatalysts can be designed to improve the photocatalytic reduction activity of CO_2, as well as study the loading form and preparation method. Secondly, because a composite of semiconductor materials can improve the charge separation rate and expand the spectral response range, research can be conducted on composite semiconductor photocatalytic materials. Thirdly, microstructure control is also an important factor in improving the photocatalytic activity of semiconductors. Due to the fact that photocatalytic reactions occur on the surface of materials, special surface microstructures in materials can significantly affect their photocatalytic activity.

The entire process of photocatalytic CO_2 reduction involves multiple steps, intermediates, and different products, making the process of product selectivity more complex. To accurately regulate the product, we can first clarify the reaction mechanism of photocatalytic CO_2 reduction and optimize its key steps to adjust the product. The photocatalytic CO_2 reduction process involves carrier kinetics and surface catalysis. These processes are influenced by numerous factors, including band structure, charge separation efficiency, and the absorption and activation of the reactants. The dynamics of CO_2 adsorption and activation significantly impact the performance and selectivity in photocatalytic CO_2 conversion; however, revealing the kinetics of these steps in photocatalytic systems remains an arduous task. Therefore, the systematic investigation of the factors influencing the mechanism of photocatalytic CO_2 reduction and product selectivity is extremely important. The carrier kinetics and the energy barrier associated with each step in the photocatalytic CO_2 reduction processes can be elucidated through theoretical simulations, and *in situ* or space/time resolution advanced characterization technology. This will facilitate an in-depth exploration of the factors governing the product generation and uncover the underlying mechanism of photocatalytic CO_2 reduction. It is expected that joint investigations on the structure–effect relationship of photocatalysts using solar energy to convert CO_2 and H_2O into various carbon fuels will break new ground. This provides valuable theoretical guidance for developing highly selective photocatalytic CO_2 reduction catalysts, thus achieving the goal of carbon neutrality.

The surface of a catalyst always changes in the catalytic process. At present, most of the studies on surface reconstruction are carried out in electrocatalytic and thermocatalytic reactions, but there are few studies on the photocatalytic process. Therefore, studies on the surface reconstruction of the catalyst during the reaction may be the future research direction of photocatalytic CO_2 reduction. Surface reconstruction typically exerts the following impacts on catalytic reactions. Firstly, it alters the distribution of active sites by changing the atomic arrangement and crystal structure of the catalyst surface. This modification can either enhance or diminish the number and utilization of active sites, thereby influencing the catalytic performance. Secondly, surface reconfiguration can induce alterations in the interaction between the reactants and catalyst, thereby affecting the adsorption behavior of the reactants. Simultaneously, altering the diffusion of reactants on the catalyst surface significantly influences the reaction rate and selectivity. Furthermore, structural damage or deactivation of the active sites may occur during certain catalytic processes. By restructuring the surface structure through the rearrangement or repair of surface atoms, the stability and service life of the catalyst can be enhanced. Therefore, comprehending and regulating surface reconfiguration are pivotal in designing efficient new catalysts as well as optimizing their catalytic performance. Also, studying the underlying mechanisms of surface reconstruction together with kinetic processes can clarify the structure–activity relationships, providing a theoretical foundation for the design and preparation of catalysts.

Data availability

No primary research results, software or code has been included and no new data were generated or analysed as part of this review.

Conflicts of interest

There are no conflicts to declare.

Acknowledgements

This work is financially supported by the National Natural Science Foundation of China (Grants No. 22372041).

Notes and references

1 S. Chu and A. Majumdar, *Nature*, 2012, **488**, 294–303.
2 F. P. Garcia de Arquer, C. T. Dinh, A. Ozden, J. Wicks, C. McCallum, A. R. Kirmani, D. H. Nam, C. Gabardo, A. Seifitokaldani, X. Wang, Y. C. Li, F. Li, J. Edwards, L. J. Richter, S. J. Thorpe, D. Sinton and E. H. Sargent, *Science*, 2020, **367**, 661–666.
3 B. D. Patterson, F. Mo, A. Borgschulte, M. Hillestad, F. Joos, T. Kristiansen, S. Sunde and J. A. van Bokhoven, *Proc. Natl. Acad. Sci. U. S. A.*, 2019, **116**, 12212–12219.
4 X. Zhang, F. Xie, X. Li, H. Chen, Y. She, C. Wang, Z. Mo, W. Yang, P. Hou, C. Wu, H. Xu and H. Li, *Appl. Surf. Sci.*, 2021, **542**, 22075–22082.
5 M. Mikkelsen, M. Jørgensen and F. C. Krebs, *Energy Environ. Sci.*, 2010, **3**, 43–81.
6 S. N. Habisreutinger, L. Schmidt-Mende and J. K. Stolarczyk, *Angew. Chem., Int. Ed.*, 2013, **52**, 7372–7408.
7 J. Bonin, A. Maurin and M. Robert, *Coord. Chem. Rev.*, 2017, **334**, 184–198.
8 Q. Wang, J. Cai, G. V. Biesold-McGee, J. Huang, Y. H. Ng, H. Sun, J. Wang, Y. Lai and Z. Lin, *Nano Energy*, 2020, **78**, 105313.
9 J. Chen, R. Abazari, K. A. Adegoke, N. W. Maxakato, O. S. Bello, M. Tahir, S. Tasleem, S. Sanati, A. M. Kirillov and Y. Zhou, *Coord. Chem. Rev.*, 2022, **469**, 214664.
10 Q. Xu, Z. Xia, J. Zhang, Z. Wei, Q. Guo, H. Jin, H. Tang, S. Li, X. Pan, Z. Su and S. Wang, *Carbon Energy*, 2022, **5**, e205.
11 B. M. Pirzada, A. H. Dar, M. N. Shaikh and A. Qurashi, *ACS Omega*, 2021, **6**, 29291–29324.
12 A. Li, X. Cao, R.-Z. Fu and S.-Q. Guo, *Biotechnol. Adv.*, 2024, **72**, 108347.
13 Y. Wang, P. Han, X. Lv, L. Zhang and G. Zheng, *Joule*, 2018, **2**, 2551–2582.
14 S. Wang and G.-Q. Lu, *Energy Fuels*, 1996, **10**, 896–904.
15 J. Schneider, M. Matsuoka, M. Takeuchi, J. Zhang, Y. Horiuchi, M. Anpo and D. W. Bahnemann, *Chem. Rev.*, 2014, **114**, 9919–9986.
16 P. Murugesan, S. Narayanan, M. Manickam, P. K. Murugesan and R. Subbiah, *Appl. Surf. Sci.*, 2018, **450**, 516–526.
17 C.-H. Huang and C.-S. Tan, *Aerosol Air Qual. Res.*, 2014, **14**, 480–499.
18 Y. C. Hao, L. W. Chen, J. Li, Y. Guo, X. Su, M. Shu and Q. Zhang, *Nat. Commun.*, 2021, **12**, 2682.
19 W. C. Chueh, C. Falter, M. Abbott, D. Scipio, P. Furler, S. M. Haile and A. Steinfeld, *Science*, 2010, **330**, 1797–1801.
20 D. D. Zhu, J. L. Liu and S. Z. Qiao, *Adv. Mater.*, 2016, **28**, 3423–3452.
21 A. Corma and H. Garcia, *J. Catal.*, 2013, **308**, 168–175.
22 S. Cheng, Z. Sun, K. H. Lim, A. A. Wibowo, T. Zhang, T. Du, L. Liu, H. T. Nguyen, G. K. Li, Z. Yin and S. Kawi, *ACS Catal.*, 2023, **13**, 7221–7229.
23 J. Ran, M. Jaroniec and S. Z. Qiao, *Adv. Mater.*, 2018, **30**, 1704649.
24 Y. Zhang, L. Cao, G. Bai and X. Lan, *Small*, 2023, **19**, 230035.
25 Y. Huo, P. Zhang, J. Chi, F. Fang, Y. Song and D. Sun, *Adv. Energy Mater.*, 2024, **14**, 2304282.
26 Z. Wu, S. Guo, L.-H. Kong, A.-F. Geng, Y.-J. Wang, P. Wang, S. Yao, K.-K. Chen and Z.-M. Zhang, *Chin. J. Catal.*, 2021, **42**, 1790–1797.
27 D.-C. Liu, D.-C. Zhong and T.-B. Lu, *EnergyChem*, 2020, **2**, 10034.
28 W. Chen, B. Han, C. Tian, X. Liu, S. Liang, H. Deng and Z. Lin, *Appl. Catal., B*, 2019, **244**, 996–1003.
29 X. Chang, T. Wang and J. Gong, *Energy Environ. Sci.*, 2016, **9**, 2177–2196.
30 G. Yin, Q. Bi, W. Zhao, J. Xu, T. Lin and F. Huang, *ChemCatChem*, 2017, **9**, 4389–4396.
31 W. Yu, D. Xu and T. Peng, *J. Mater. Chem. A*, 2015, **3**, 19936–19947.
32 X. Li, J. Wen, J. Low, Y. Fang and J. Yu, *Sci. China Mater.*, 2014, **57**, 70–100.
33 S. Sorcar, Y. Hwang, C. A. Grimes and S.-I. In, *Mater. Today*, 2017, **20**, 507–515.
34 A. Meng, S. Wu, B. Cheng, J. Yu and J. Xu, *J. Mater. Chem. A*, 2018, **6**, 4729–4736.
35 S. Xie, Y. Wang, Q. Zhang, W. Deng and Y. Wang, *ACS Catal.*, 2014, **4**, 3644–3653.
36 J. Low, L. Zhang, T. Tong, B. Shen and J. Yu, *J. Catal.*, 2018, **361**, 255–266.
37 F. Xu, J. Zhang, B. Zhu, J. Yu and J. Xu, *Appl. Catal., B*, 2018, **230**, 194–202.
38 J. L. White, M. F. Baruch, J. E. Pander, Y. Hu, I. C. Fortmeyer, J. E. Park, T. Zhang, K. Liao, J. Gu, Y. Yan, T. W. Shaw, E. Abelev and A. B. Bocarsly, *Chem. Rev.*, 2015, **115**, 12888–12935.
39 J. Fu, K. Jiang, X. Qiu, J. Yu and M. Liu, *Mater. Today*, 2020, **32**, 222–243.

40 A. Vasileff, C. Xu, Y. Jiao, Y. Zheng and S.-Z. Qiao, *Chem*, 2018, **4**, 1809–1831.

41 Y. Wang, Q. Guan and J. Xiang, *Int. J. Surg.*, 2018, **55**, 98–102.

42 T. Wang, X. Meng, G. Liu, K. Chang, P. Li, Q. Kang, L. Liu, M. Li, S. Ouyang and J. Ye, *J. Mater. Chem. A*, 2015, **3**, 9491–9501.

43 H. Zhang, T. Wang, J. Wang, H. Liu, T. D. Dao, M. Li, G. Liu, X. Meng, K. Chang, L. Shi, T. Nagao and J. Ye, *Adv. Mater.*, 2016, **28**, 3703–3710.

44 Y. Wang, E. Chen and J. Tang, *ACS Catal.*, 2022, **12**, 7300–7316.

45 K. Zhao, W. Pang, S. Jiang, C. Hu, P. Liu, D. Cui, X. An, B. Tian, C. Gao, P. Zhang, M. Tian, D. Fu and H. Zhao, *Nano Res.*, 2023, **16**, 4812–4820.

46 B. Lei, W. Cui, P. Chen, L. Chen, J. Li and F. Dong, *ACS Catal.*, 2022, **12**, 9670–9678.

47 J. Di, G. Hao, G. Liu, J. Zhou, W. Jiang and Z. Liu, *Coord. Chem. Rev.*, 2023, **482**, 215057.

48 S. Yin, Y. Zhou, Z. Liu, H. Wang, X. Zhao, Z. Zhu, Y. Yan and P. Huo, *Nat. Commun.*, 2024, **15**, 437.

49 V. P. Indrakanti, J. D. Kubicki and H. H. Schobert, *Energy Environ. Sci.*, 2009, **2**, 745–758.

50 Z. Xie, H. Luo, S. Xu, L. Li and W. Shi, *Adv. Funct. Mater.*, 2024, **34**, 2313886.

51 H.-N. Wang, Y.-H. Zou, H.-X. Sun, Y. Chen, S.-L. Li and Y.-Q. Lan, *Coord. Chem. Rev.*, 2021, **438**, 213906.

52 H. J. Son, C. Pac and S. O. Kang, *Acc. Chem. Res.*, 2021, **54**, 4530–4544.

53 S. Singh, A. Modak, K. K. Pant, A. Sinhamahapatra and P. Biswas, *ACS Appl. Nano Mater.*, 2021, **4**, 8644–8667.

54 J. Albero, Y. Peng and H. García, *ACS Catal.*, 2020, **10**, 5734–5749.

55 L. Wang, B. Zhu, J. Zhang, J. B. Ghasemi, M. Mousavi and J. Yu, *Matter*, 2022, **5**, 4187–4211.

56 Y. Yin, W. Jing, F. Wang, Y. Liu and L. Guo, *Carbon*, 2023, **214**, 118317.

57 Q. Liu, J. Lin, H. Cheng, L. Wei and F. Wang, *Angew. Chem., Int. Ed.*, 2023, **62**, e202312151.

58 X. Li and Q.-L. Zhu, *EnergyChem*, 2020, **2**, 10033.

59 J. Liang, H. Yu, J. Shi, B. Li, L. Wu and M. Wang, *Adv. Mater.*, 2023, **35**, 2209814.

60 W. Jiang, H. Loh, B. Q. L. Low, H. Zhu, J. Low, J. Z. X. Heng, K. Y. Tang, Z. Li, X. J. Loh, E. Ye and Y. Xiong, *Appl. Catal., B*, 2023, **321**, 122079.

61 S. Wang, X. Han, Y. Zhang, N. Tian, T. Ma and H. Huang, *Small Struct.*, 2020, **2**, 2000061.

62 L. j. Guo, Y. j. Wang and T. He, *Chem. Rec.*, 2016, **16**, 1918–1933.

63 F. Qi, Y. Pu, D. Wu, X. Tang and Q. Huang, *Chem. Rec.*, 2023, **23**, e202300078.

64 W. A. Thompson, E. Sanchez Fernandez and M. M. Maroto-Valer, *ACS Sustain. Chem. Eng.*, 2020, **8**, 4677–4692.

65 J. Wang, H. Li, P. Gao, Y. Peng, S. Cao and M. Antonietti, *Chem. Eng. J.*, 2022, **443**, 136447.

66 E. Gong, S. Ali, C. B. Hiragond, H. S. Kim, N. S. Powar, D. Kim, H. Kim and S.-I. In, *Energy Environ. Sci.*, 2022, **15**, 880–937.

67 S. Sun, M. Watanabe, J. Wu, Q. An and T. Ishihara, *J. Am. Chem. Soc.*, 2018, **140**, 6474–6482.

68 G. T. S. T. da Silva, A. E. Nogueira, J. A. Oliveira, J. A. Torres, O. F. Lopes and C. Ribeiro, *Appl. Catal., B*, 2019, **242**, 349–357.

69 Y. Xiang, W. Dong, P. Wang, S. Wang, X. Ding, F. Ichihara, Z. Wang, Y. Wada, S. Jin, Y. Weng, H. Chen and J. Ye, *Appl. Catal., B*, 2020, **274**, 119096.

70 S. Hu, P. Qiao, X. Yi, Y. Lei, H. Hu, J. Ye and D. Wang, *Angew. Chem., Int. Ed.*, 2023, **62**, e202304585.

71 Y. Zheng, X. Shen, M. Lin, M. Zhu, B. Yang, J. Yan, Z. Zhuang and Y. Yu, *Small*, 2024, **20**, 2306836.

72 X. Shi, X. a. Dong, Y. Sun, S. Zhang and F. Dong, *Research*, 2022, **2022**, 9818792.

73 S. Cao, Y. Li, B. Zhu, M. Jaroniec and J. Yu, *J. Catal.*, 2017, **349**, 208–217.

74 M. Li, M. Wang, L. Zhu, Y. Li, Z. Yan, Z. Shen and X. Cao, *Appl. Catal., B*, 2018, **231**, 269–276.

75 P. Wang, S. Guo, Q. P. Zhao, S. Y. Xu, H. Lv, T. B. Lu and Z. M. Zhang, *Angew. Chem., Int. Ed.*, 2024, **63**, e202312450.

76 S. Hu, P. Qiao, X. Liang, G. Ba, X. Zu, H. Hu, J. Ye and D. Wang, *Appl. Catal., B*, 2024, **346**, 123737.

77 L. Liu, H. Huang, Z. Chen, H. Yu, K. Wang, J. Huang, H. Yu and Y. Zhang, *Angew. Chem., Int. Ed.*, 2021, **60**, 18303–18308.

78 S. Hussain, Y. Wang, L. Guo and T. He, *J. Photochem. Photobiol., C*, 2022, **52**, 100538.

79 J. Jiang, X. Wang, Q. Xu, Z. Mei, L. Duan and H. Guo, *Appl. Catal., B*, 2022, **316**, 121679.

80 Q. V. Le, V.-H. Nguyen, T. D. Nguyen, A. Sharma, G. Rahman and D. L. T. Nguyen, *Chem. Eng. Sci.*, 2021, **237**, 116547.

81 R. Long, Y. Li, Y. Liu, S. Chen, X. Zheng, C. Gao, C. He, N. Chen, Z. Qi, L. Song, J. Jiang, J. Zhu and Y. Xiong, *J. Am. Chem. Soc.*, 2017, **139**, 4486–4492.

82 S. A. Fors and C. A. Malapit, *ACS Catal.*, 2023, **13**, 4231–4249.

83 Q. Chen, Y. Zhang, E. You, Q. Jiang, X. Chen, Y. Wang, Z. Song, K. Chang, Z. Xie and Q. Kuang, *Small*, 2022, **18**, 2204924.

84 L. Zou, Z. A. Chen, D. H. Si, S. L. Yang, W. Q. Gao, K. Wang, Y. B. Huang and R. Cao, *Angew. Chem., Int. Ed.*, 2023, **62**, e202309820.

85 M. Xing, Y. Zhou, C. Dong, L. Cai, L. Zeng, B. Shen, L. Pan, C. Dong, Y. Chai, J. Zhang and Y. Yin, *Nano Lett.*, 2018, **18**, 3384–3390.

86 T. Guo, X. Xu, Z. Xu, F. You, X. Fan, J. Liu and Z. Wang, *Adv. Mater.*, 2024, 202402071.

87 Y.-H. Chen, M.-Y. Qi, Y.-H. Li, Z.-R. Tang, T. Wang, J. Gong and Y.-J. Xu, *Cell Rep. Phys. Sci.*, 2021, **2**, 10031.

88 K. Li, T. Peng, Z. Ying, S. Song and J. Zhang, *Appl. Catal., B*, 2016, **180**, 130–138.

89 F. Q. Yan, X. Y. Dong, Y. M. Wang, Q. Y. Wang, S. Wang and S. Q. Zang, *Adv. Sci.*, 2024, 2401508.

90 Z. Wang, J. Zhu, X. Zu, Y. Wu, S. Shang, P. Ling, P. Qiao, C. Liu, J. Hu, Y. Pan, J. Zhu, Y. Sun and Y. Xie, *Angew. Chem., Int. Ed.*, 2022, **61**, e202203249.
91 Z. Sun, T. Liao, Y. Dou, S. M. Hwang, M.-S. Park, L. Jiang, J. H. Kim and S. X. Dou, *Nat. Commun.*, 2014, **5**, 3813.
92 S. Yue, Z. Zhao, T. Zhang, P. Wang and S. Zhan, *Mater. Today Energy*, 2024, **40**, 101482.
93 Y. Wang, Z. Hu, W. Wang, Y. Li, H. He, L. Deng, Y. Zhang, J. Huang, N. Zhao, G. Yu and Y.-N. Liu, *Appl. Catal., B*, 2023, **327**, 122419.
94 J. Hou, M. Yang, Q. Dou, Q. Chen, X. Wang, C. Hu and R. Paul, *Chem. Eng. J.*, 2022, **450**, 122319.
95 X. Jia, C. Hu, H. Sun, J. Cao, H. Lin, X. Li and S. Chen, *Appl. Catal., B*, 2023, **324**, 122232.
96 X. Xiong, C. Mao, Z. Yang, Q. Zhang, G. I. N. Waterhouse, L. Gu and T. Zhang, *Adv. Energy Mater.*, 2020, **10**, 2002928.
97 Q. Chen, W. Mo, G. Yang, S. Zhong, H. Lin, J. Chen and S. Bai, *Small*, 2021, **17**, 2101105.
98 D. Hong, T. Kawanishi, Y. Tsukakoshi, H. Kotani, T. Ishizuka and T. Kojima, *J. Am. Chem. Soc.*, 2019, **141**, 20309–20317.
99 D. Kim, S. Bhattacharjee, E. Lam, C. Casadevall, S. Rodríguez-Jiménez and E. Reisner, *Small*, 2024, 202400057.
100 K. Li, S. Zhang, Y. Li, J. Fan and K. Lv, *Chin. J. Catal.*, 2021, **42**, 3–14.
101 Q. Lin, J. Zhao, P. Zhang, S. Wang, Y. Wang, Z. Zhang, N. Wen, Z. Ding, R. Yuan, X. Wang and J. Long, *Carbon Energy*, 2024, **6**, e435.
102 L. Gao, Y. Li, M. Xiao, S. Wang, G. Fu and L. Wang, *2D Mater.*, 2017, **4**, 025031.
103 Y. Zhang, Z. Xu, Q. Wang, W. Hao, X. Zhai, X. Fei, X. Huang and Y. Bi, *Appl. Catal., B*, 2021, **299**, 120679.
104 C. Chen, Y. Li and P. Yang, *Joule*, 2021, **5**, 737–742.
105 H. Wang, H. Feng, Y. Bao, J. Wu, X. Qu, X. Zhang, J. Liu and H. Wang, *Catal. Sci. Technol.*, 2023, **13**, 4996–5004.
106 P. Hu, G. Liang, B. Zhu, W. Macyk, J. Yu and F. Xu, *ACS Catal.*, 2023, **13**, 12623–12633.
107 F. Xu, Z. Li, R. Zhu, Y. Chu, Z. Pan, S. Xia, J. Fu, Z. Xiao, X. Ji, M. Liu and B. Weng, *Appl. Catal., B*, 2022, **316**, 121615.
108 K. Yang, Z. Yang, C. Zhang, Y. Gu, J. Wei, Z. Li, C. Ma, X. Yang, K. Song, Y. Li, Q. Fang and J. Zhou, *Chem. Eng. J.*, 2021, **418**, 129344.
109 L. Yuan, M. Y. Qi, Z. R. Tang and Y. J. Xu, *Angew. Chem., Int. Ed.*, 2021, **60**, 21150–21172.
110 L. Liu and Y. Li, *Aerosol Air Qual. Res.*, 2014, **14**, 453–469.
111 Y. Wang, E. Chen and J. Tang, *ACS Catal.*, 2022, **12**, 7300–7316.
112 K. Li, B. Peng and T. Peng, *ACS Catal.*, 2016, **6**, 7485–7527.
113 Y. Zhou, Z. Wang, L. Huang, S. Zaman, K. Lei, T. Yue, Z. a. Li, B. You and B. Y. Xia, *Adv. Energy Mater.*, 2021, **11**, 2003159.
114 J. Ran, M. Jaroniec and S. Z. Qiao, *Adv. Mater.*, 2018, **30**, 1704649.
115 S. Nahar, M. F. M. Zain, A. A. H. Kadhum, H. A. Hasan and M. R. Hasan, *Materials*, 2017, **10**, 629.
116 B. T. Barrocas, N. Ambrozova and K. Koci, *Materials*, 2022, **15**, 967.
117 L. Liao, G. Xie, X. Xie and N. Zhang, *J. Phys. Chem. C*, 2023, **127**, 2766–2781.
118 L. Wang, W. Chen, D. Zhang, Y. Du, R. Amal, S. Qiao, J. Wu and Z. Yin, *Chem. Soc. Rev.*, 2019, **48**, 5310–5349.
119 S. Wang, J. Wang, Y. Wang, X. Sui, S. Wu, W. Dai, Z. Zhang, Z. Ding and J. Long, *ACS Catal.*, 2024, **14**, 10760–10788.
120 Y. Wu, Q. Hu, Q. Chen, X. Jiao and Y. Xie, *Acc. Chem. Res.*, 2023, **56**, 2500–2513.
121 S. Cheng, Z. Sun, K. H. Lim, T. Z. H. Gani, T. Zhang, Y. Wang, H. Yin, K. Liu, H. Guo, T. Du, L. Liu, G. K. Li, Z. Yin and S. Kawi, *Adv. Energy Mater.*, 2022, **12**, 2200389.
122 H. Wang, L. Zhang, Z. Chen, J. Hu, S. Li, Z. Wang, J. Liu and X. Wang, *Chem. Soc. Rev.*, 2014, **43**, 5234–5244.
123 K. Zhong, P. Sun and H. Xu, *Small*, 2024, 202310677.
124 L. Ran, J. Hou, S. Cao, Z. Li, Y. Zhang, Y. Wu, B. Zhang, P. Zhai and L. Sun, *Sol. RRL*, 2020, **4**, 1900487.
125 P. Raizada, V. Soni, A. Kumar, P. Singh, A. A. Parwaz Khan, A. M. Asiri, V. K. Thakur and V.-H. Nguyen, *Journal of Materiomics*, 2021, **7**, 388–418.
126 E. Pastor, M. Sachs, S. Selim, J. R. Durrant, A. A. Bakulin and A. Walsh, *Nat. Rev. Mater.*, 2022, **7**, 503–521.
127 Y. Ji and Y. Luo, *J. Am. Chem. Soc.*, 2016, **138**, 15896–15902.
128 M. Zhang, D. Zhang, X. Jing, B. Xu and C. Duan, *Angew. Chem., Int. Ed.*, 2024, **63**, e202402755.
129 X. Zu, Y. Zhao, X. Li, R. Chen, W. Shao, Z. Wang, J. Hu, J. Zhu, Y. Pan, Y. Sun and Y. Xie, *Angew. Chem., Int. Ed.*, 2021, **60**, 13840–13846.
130 S. Vinoth, W.-J. Ong and A. Pandikumar, *Coord. Chem. Rev.*, 2022, **464**, 214541.
131 Y. Wang, Q. Lai, Y. He and M. Fan, *Catal. Commun.*, 2018, **108**, 98–102.
132 Z. Geng, X. Kong, W. Chen, H. Su, Y. Liu, F. Cai, G. Wang and J. Zeng, *Angew. Chem., Int. Ed.*, 2018, **57**, 6054–6059.
133 Z. Miao, Q. Wang, Y. Zhang, L. Meng and X. Wang, *Appl. Catal., B*, 2022, **301**, 120802.
134 W. Tu, Y. Zhou and Z. Zou, *Adv. Mater.*, 2014, **26**, 4607–4626.
135 L. Liu, C. Zhao and Y. Li, *J. Phys. Chem. C*, 2012, **116**, 7904–7912.
136 D. Liu, C. Wang, Y. Yu, B.-H. Zhao, W. Wang, Y. Du and B. Zhang, *Chem*, 2019, **5**, 376–389.
137 H. Lai, X. Zeng, T. Song, S. Yin, B. Long, A. Ali and G.-J. Deng, *J. Colloid Interface Sci.*, 2022, **608**, 1792–1801.
138 J. Di, C. Zhu, M. Ji, M. Duan, R. Long, C. Yan, K. Gu, J. Xiong, Y. She, J. Xia, H. Li and Z. Liu, *Angew. Chem., Int. Ed.*, 2018, **57**, 14847–14851.
139 F. Chen, Z. Ma, L. Ye, T. Ma, T. Zhang, Y. Zhang and H. Huang, *Adv. Mater.*, 2020, **32**, 1908350.
140 H. Tan, Z. Zhao, W.-b. Zhu, E. N. Coker, B. Li, M. Zheng, W. Yu, H. Fan and Z. Sun, *ACS Appl. Mater. Interfaces*, 2014, **6**, 19184–19190.
141 M. Xing, J. Zhang, F. Chen and B. Tian, *Chem. Commun.*, 2011, **47**, 4947–4949.

142 L. Li, X. Feng, Y. Nie, S. Chen, F. Shi, K. Xiong, W. Ding, X. Qi, J. Hu, Z. Wei, L.-J. Wan and M. Xia, *ACS Catal.*, 2015, **5**, 4825–4832.

143 H. Xu, C. Yan, R. Li, L. Song and S. Ouyang, *Nanotechnology*, 2022, **33**, 085401.

144 Z. Shi, D. Shi, L. Zhang and Y. Cao, *J. Power Sources*, 2022, **535**, 231421.

145 Y. Zhou, Q. Zhang, X. Shi, Q. Song, C. Zhou and D. Jiang, *J. Colloid Interface Sci.*, 2022, **608**, 2809–2819.

146 H. Zeng, M. h. Oubla, X. Zhong, N. Alonso-Vante, F. Du, Y. Xie, Y. Huang and J. Ma, *Appl. Catal., B*, 2021, **281**, 119535.

147 Z. Li, K. Zhu, J. Li and X. Wang, *CrystEngComm*, 2014, **16**, 10112–10122.

148 Y. Zhang, Y. Li, H. Yu, K. Yu and H. Yu, *J. Mater. Sci. Technol.*, 2022, **106**, 139–146.

149 J. Wu, X. Li, W. Shi, P. Ling, Y. Sun, X. Jiao, S. Gao, L. Liang, J. Xu, W. Yan, C. Wang and Y. Xie, *Angew. Chem., Int. Ed.*, 2018, **57**, 8719–8723.

150 S. Yin, X. Zhao, E. Jiang, Y. Yan, P. Zhou and P. Huo, *Energy Environ. Sci.*, 2022, **15**, 1556–1562.

151 W. Gao, S. Li, H. He, X. Li, Z. Cheng, Y. Yang, J. Wang, Q. Shen, X. Wang, Y. Xiong, Y. Zhou and Z. Zou, *Nat. Commun.*, 2021, **12**, 4717.

152 A. Quindimil, U. De-La-Torre, B. Pereda-Ayo, A. Davó-Quiñonero, E. Bailón-García, D. Lozano-Castelló, J. A. González-Marcos, A. Bueno-López and J. R. González-Velasco, *Catal. Today*, 2020, **356**, 419–432.

153 J. A. H. Dreyer, P. Li, L. Zhang, G. K. Beh, R. Zhang, P. H. L. Sit and W. Y. Teoh, *Appl. Catal., B*, 2017, **219**, 715–726.

154 X. Chen and S. S. Mao, *Chem. Rev.*, 2007, **107**, 2891–2959.

155 B. Kraeutler and A. J. Bard, *J. Am. Chem. Soc.*, 1978, **100**, 4317–4318.

156 W.-N. Wang, W.-J. An, B. Ramalingam, S. Mukherjee, D. M. Niedzwiedzki, S. Gangopadhyay and P. Biswas, *Nano Res.*, 2013, **58**, 305.

157 S. Xie, Y. Wang, Q. Zhang, W. Fan, W. Deng and Y. Wang, *Chem. Commun.*, 2013, **49**, 2451–2453.

158 Z. Xiong, Z. Lei, C.-C. Kuang, X. Chen, B. Gong, Y. Zhao, J. Zhang, C. Zheng and J. C. S. Wu, *Appl. Catal., B*, 2017, **202**, 695–703.

159 Z. Ma, P. Li, L. Ye, L. Wang, H. Xie and Y. Zhou, *Catal. Sci. Technol.*, 2018, **8**, 5129–5132.

160 Ş. Neaţu, J. A. Maciá-Agulló, P. Concepción and H. Garcia, *J. Am. Chem. Soc.*, 2014, **136**, 15969–15976.

161 C. Kim, F. Dionigi, V. Beermann, X. Wang, T. Moller and P. Strasser, *Adv. Mater.*, 2019, **31**, e1805617.

162 Y. Sugano, Y. Shiraishi, D. Tsukamoto, S. Ichikawa, S. Tanaka and T. Hirai, *Angew. Chem., Int. Ed.*, 2013, **52**, 5295–5299.

163 S. Wang and X. Wang, *Appl. Catal., B*, 2015, **162**, 494–500.

164 D. Li, M. Kassymova, X. Cai, S.-Q. Zang and H.-L. Jiang, *Coord. Chem. Rev.*, 2020, **412**, 213262.

165 X. Meng, S. Ouyang, T. Kako, P. Li, Q. Yu, T. Wang and J. Ye, *Chem. Commun.*, 2014, **50**, 11517–11519.

166 X. Feng, F. Pan, H. Zhao, W. Deng, P. Zhang, H.-C. Zhou and Y. Li, *Appl. Catal., B*, 2018, **238**, 274–283.

167 T. Ghanbari, F. Abnisa and W. M. A. Wan Daud, *Sci. Total Environ.*, 2020, **707**, 135090.

168 Z. Wang, K. Teramura, Z. Huang, S. Hosokawa, Y. Sakata and T. Tanaka, *Catal. Sci. Technol.*, 2016, **6**, 1025–1032.

169 Y. Huang, K. Li, J. Zhou, J. Guan, F. Zhu, K. Wang, M. Liu, W. Chen and N. Li, *Chem. Eng. J.*, 2022, **439**, 135744.

170 G. Liu, K. Du, S. Haussener and K. Wang, *ChemSusChem*, 2016, **9**, 2878–2904.

171 Z. Sun, H. Wang, Z. Wu and L. Wang, *Catal. Today*, 2018, **300**, 160–172.

172 X. Wang, S. Blechert and M. Antonietti, *ACS Catal.*, 2012, **2**, 1596–1606.

173 W. J. Ong, L. L. Tan, Y. H. Ng, S. T. Yong and S. P. Chai, *Chem. Rev.*, 2016, **116**, 7159–7329.

174 J. Fu, J. Yu, C. Jiang and B. Cheng, *Adv. Energy Mater.*, 2018, **8**, 1701503.

175 X. Dong and F. Cheng, *J. Mater. Chem. A*, 2015, **3**, 23642–23652.

176 X. Huang, W. Gu, Y. Ma, D. Liu, N. Ding, L. Zhou, J. Lei, L. Wang and J. Zhang, *Res. Chem. Intermed.*, 2020, **46**, 5133–5164.

177 Q. Lin, L. Li, S. Liang, M. Liu, J. Bi and L. Wu, *Appl. Catal., B*, 2015, **163**, 135–142.

178 X. Ma, Y. Lv, J. Xu, Y. Liu, R. Zhang and Y. Zhu, *J. Phys. Chem. C*, 2012, **116**, 23485–23493.

179 F. Almomani, R. Bhosale, M. Khraisheh, A. Kumar and M. Tawalbeh, *Appl. Surf. Sci.*, 2019, **483**, 363–372.

180 H. Guo, Z. Shu, D. Chen, Y. Tan, J. Zhou, F. Meng and T. Li, *Chem. Phys.*, 2020, **533**, 110714.

181 S. Patnaik, D. P. Sahoo and K. Parida, *Carbon*, 2021, **172**, 682–711.

182 M. Arumugam, M. Tahir and P. Praserthdam, *Chemosphere*, 2022, **286**, 131765.

183 T. Xiong, W. Cen, Y. Zhang and F. Dong, *ACS Catal.*, 2016, **6**, 2462–2472.

184 H.-Z. Wu, L.-M. Liu and S.-J. Zhao, *Appl. Surf. Sci.*, 2015, **358**, 363–369.

185 B. Zhu, J. Zhang, C. Jiang, B. Cheng and J. Yu, *Appl. Catal., B*, 2017, **207**, 27–34.

186 X. Ma, Y. Lv, J. Xu, Y. Liu, R. Zhang and Y. Zhu, *J. Phys. Chem. C*, 2012, **116**, 23485–23493.

187 G. Dong, K. Zhao and L. Zhang, *Chem. Commun.*, 2012, **48**, 6178–6180.

188 J. Fang, H. Fan, M. Li and C. Long, *J. Mater. Chem. A*, 2015, **3**, 13819–13826.

189 B. Liu, M. Liu, L. Tian, F. Guo, Y. Xia, T. Wang, W. Hu and R. Guan, *Appl. Surf. Sci.*, 2021, **540**, 148411.

190 H. Zhang, Y. Tang, Z. Liu, Z. Zhu, X. Tang and Y. Wang, *Chem. Phys. Lett.*, 2020, **751**, 137467.

191 Y. Wang, Y. Xu, Y. Wang, H. Qin, X. Li, Y. Zuo, S. Kang and L. Cui, *Catal. Commun.*, 2016, **74**, 75–79.

192 P. Babu, S. Mohanty, B. Naik and K. Parida, *ACS Appl. Energy Mater.*, 2018, **1**, 5936–5947.

193 K. Wang, J. Fu and Y. Zheng, *Appl. Catal., B*, 2019, **254**, 270–282.

194 X. Dong, S. Zhang, H. Wu, Z. Kang and L. Wang, *RSC Adv.*, 2019, **9**, 28894–28901.

195 J. Low, J. Yu, M. Jaroniec, S. Wageh and A. A. Al-Ghamdi, *Adv. Mater.*, 2017, **29**, 1601694.

196 H. J. Yun, H. Lee, N. D. Kim, D. M. Lee, S. Yu and J. Yi, *ACS Nano*, 2011, **5**, 4084–4090.

197 A. Iwase, Y. H. Ng, Y. Ishiguro, A. Kudo and R. Amal, *J. Am. Chem. Soc.*, 2011, **133**, 11054–11057.

198 A. Alhebshi, E. Sharaf Aldeen, R. S. Mim, B. Tahir and M. Tahir, *Int. J. Energy Res.*, 2021, **46**, 5523–5584.

199 A. J. Bard, *J. Photochem.*, 1979, **10**, 59–75.

200 H. Tada, T. Mitsui, T. Kiyonaga, T. Akita and K. Tanaka, *Nat. Mater.*, 2006, **5**, 782–786.

201 J. Yu, S. Wang, J. Low and W. Xiao, *Phys. Chem. Chem. Phys.*, 2013, **15**, 16883–16890.

202 J. Liu, B. Cheng and J. Yu, *Phys. Chem. Chem. Phys.*, 2016, **18**, 31175–31183.

203 Y. Wang, Z. Zhang, L. Zhang, Z. Luo, J. Shen, H. Lin, J. Long, J. C. S. Wu, X. Fu, X. Wang and C. Li, *J. Am. Chem. Soc.*, 2018, **140**, 14595–14598.

204 Y. Wang, X. Shang, J. Shen, Z. Zhang, D. Wang, J. Lin, J. C. S. Wu, X. Fu, X. Wang and C. Li, *Nat. Commun.*, 2020, **11**, 3043.

205 J. Fu, Q. Xu, J. Low, C. Jiang and J. Yu, *Appl. Catal., B*, 2019, **243**, 556–565.

206 Q. Xu, L. Zhang, B. Cheng, J. Fan and J. Yu, *Chem*, 2020, **6**, 1543–1559.

207 Y. Yang, D. Zhang, J. Fan, Y. Liao and Q. Xiang, *Sol. RRL*, 2021, **5**, 2000351.

208 X. Deng, J. Zhang, K. Qi, G. Liang, F. Xu and J. Yu, *Nat. Commun.*, 2024, **15**, 4087.

209 Y. Sun, K. Lai, N. Li, Y. Gao and L. Ge, *Appl. Catal., B*, 2024, **357**, 124302.

210 B. Qiao, A. Wang, X. Yang, L. F. Allard, Z. Jiang, Y. Cui, J. Liu, J. Li and T. Zhang, *Nat. Chem.*, 2011, **3**, 634–641.

211 J. Xing, J. F. Chen, Y. H. Li, W. T. Yuan, Y. Zhou, L. R. Zheng, H. F. Wang, P. Hu, Y. Wang, H. J. Zhao, Y. Wang and H. G. Yang, *Chem.–Eur. J.*, 2014, **20**, 2138–2144.

212 Z. Wang, X. Hao, S. Gerhold, P. Mares, M. Wagner, R. Bliem, K. Schulte, M. Schmid, C. Franchini and U. Diebold, *J. Phys. Chem. C*, 2014, **118**, 19904–19909.

213 J. Lin, A. Wang, B. Qiao, X. Liu, X. Yang, X. Wang, J. Liang, J. Li, J. Liu and T. Zhang, *J. Am. Chem. Soc.*, 2013, **135**, 15314–15317.

214 J. C. Matsubu, V. N. Yang and P. Christopher, *J. Am. Chem. Soc.*, 2015, **137**, 3076–3084.

215 J. Jones, H. Xiong, A. T. DeLaRiva, E. J. Peterson, H. Pham, S. R. Challa, G. Qi, S. Oh, M. H. Wiebenga, X. I. Pereira Hernández, Y. Wang and A. K. Datye, *Science*, 2016, **353**, 150–154.

216 M. Moliner, J. E. Gabay, C. E. Kliewer, R. T. Carr, J. Guzman, G. L. Casty, P. Serna and A. Corma, *J. Am. Chem. Soc.*, 2016, **138**, 15743–15750.

217 S. Wei, A. Li, J.-C. Liu, Z. Li, W. Chen, Y. Gong, Q. Zhang, W.-C. Cheong, Y. Wang, L. Zheng, H. Xiao, C. Chen, D. Wang, Q. Peng, L. Gu, X. Han, J. Li and Y. Li, *Nat. Nanotechnol.*, 2018, **13**, 856–861.

218 W. Huang, S. Zhang, Y. Tang, Y. Li, L. Nguyen, Y. Li, J. Shan, D. Xiao, R. Gagne, A. I. Frenkel and F. Tao, *Angew. Chem., Int. Ed.*, 2016, **55**, 13441–13445.

219 C. Wang, X.-K. Gu, H. Yan, Y. Lin, J. Li, D. Liu, W.-X. Li and J. Lu, *ACS Catal.*, 2017, **7**, 887–891.

220 N. Cheng, S. Stambula, D. Wang, M. N. Banis, J. Liu, A. Riese, B. Xiao, R. Li, T.-K. Sham, L.-M. Liu, G. A. Botton and X. Sun, *Nat. Commun.*, 2016, **7**, 13638.

221 B. J. O'Neill, D. H. K. Jackson, J. Lee, C. Canlas, P. C. Stair, C. L. Marshall, J. W. Elam, T. F. Kuech, J. A. Dumesic and G. W. Huber, *ACS Catal.*, 2015, **5**, 1804–1825.

222 J. S. King, A. Wittstock, J. Biener, S. O. Kucheyev, Y. M. Wang, T. F. Baumann, S. K. Giri, A. V. Hamza, M. Baeumer and S. F. Bent, *Nano Lett.*, 2008, **8**, 2405–2409.

223 C. Liu, C.-C. Wang, C.-C. Kei, Y.-C. Hsueh and T.-P. Perng, *Small*, 2009, **5**, 1535–1538.

224 S. Sun, G. Zhang, N. Gauquelin, N. Chen, J. Zhou, S. Yang, W. Chen, X. Meng, D. Geng, M. N. Banis, R. Li, S. Ye, S. Knights, G. A. Botton, T.-K. Sham and X. Sun, *Sci. Rep.*, 2013, **3**, 1775.

225 Y. Cao, S. Chen, Q. Luo, H. Yan, Y. Lin, W. Liu, L. Cao, J. Lu, J. Yang, T. Yao and S. Wei, *Angew. Chem., Int. Ed.*, 2017, **56**, 12191–12196.

226 G. E. Johnson, C. Wang, T. Priest and J. Laskin, *Anal. Chem.*, 2011, **83**, 8069–8072.

227 G. E. Johnson, T. Priest and J. Laskin, *ACS Nano*, 2012, **6**, 573–582.

228 Z. Zhang, Y. Zhu, H. Asakura, B. Zhang, J. Zhang, M. Zhou, Y. Han, T. Tanaka, A. Wang, T. Zhang and N. Yan, *Nat. Commun.*, 2017, **8**, 16100.

229 M. Kottwitz, Y. Li, R. M. Palomino, Z. Liu, G. Wang, Q. Wu, J. Huang, J. Timoshenko, S. D. Senanayake, M. Balasubramanian, D. Lu, R. G. Nuzzo and A. I. Frenkel, *ACS Catal.*, 2019, **9**, 8738–8748.

230 K. Mou, Z. Chen, X. Zhang, M. Jiao, X. Zhang, X. Ge, W. Zhang and L. Liu, *Small*, 2019, **15**, 1903668.

231 M. J. Islam, M. Granollers Mesa, A. Osatiashtiani, M. J. Taylor, J. C. Manayil, C. M. A. Parlett, M. A. Isaacs and G. Kyriakou, *Appl. Catal., B*, 2020, **273**, 119062.

232 H. Wang, J. Shen, J. Huang, T. Xu, J. Zhu, Y. Zhu and C. Li, *Nanoscale*, 2017, **9**, 16817–16825.

233 X. Wang, X.-P. Fu, W.-Z. Yu, C. Ma, C.-J. Jia and R. Si, *Inorg. Chem. Front.*, 2017, **4**, 2059–2067.

234 Z. Bo, L. R. McCullough, S. Dull, M. A. Ardagh, J. Wang and J. Notestein, *J. Chem. Phys.*, 2019, **151**, 214703.

235 S. L. Wegener, T. J. Marks and P. C. Stair, *Acc. Chem. Res.*, 2012, **45**, 206–214.

236 T. W. Hansen, A. T. DeLaRiva, S. R. Challa and A. K. Datye, *Acc. Chem. Res.*, 2013, **46**, 1720–1730.

237 S. Zhang, L. Nguyen, J.-X. Liang, J. Shan, J. Liu, A. I. Frenkel, A. Patlolla, W. Huang, J. Li and F. Tao, *Nat. Commun.*, 2015, **6**, 7938.

238 X.-L. Ma, J.-C. Liu, H. Xiao and J. Li, *J. Am. Chem. Soc.*, 2018, **140**, 46–49.

239 J. Wan, W. Chen, C. Jia, L. Zheng, J. Dong, X. Zheng, Y. Wang, W. Yan, C. Chen, Q. Peng, D. Wang and Y. Li, *Adv. Mater.*, 2018, **30**, 1705369.

240 G. Liu, A. W. Robertson, M. M.-J. Li, W. C. H. Kuo, M. T. Darby, M. H. Muhieddine, Y.-C. Lin, K. Suenaga, M. Stamatakis, J. H. Warner and S. C. E. Tsang, *Nat. Chem.*, 2017, **9**, 810–816.

241 L. Nie, D. Mei, H. Xiong, B. Peng, Z. Ren, X. I. P. Hernandez, A. DeLaRiva, M. Wang, M. H. Engelhard, L. Kovarik, A. K. Datye and Y. Wang, *Science*, 2017, **358**, 1419–1423.

242 Q. Fu, H. Saltsburg and M. Flytzani-Stephanopoulos, *Science*, 2003, **301**, 935–938.

243 R. Lang, W. Xi, J.-C. Liu, Y.-T. Cui, T. Li, A. F. Lee, F. Chen, Y. Chen, L. Li, L. Li, J. Lin, S. Miao, X. Liu, A.-Q. Wang, X. Wang, J. Luo, B. Qiao, J. Li and T. Zhang, *Nat. Commun.*, 2019, **10**, 234.

244 S. Ji, Y. Qu, T. Wang, Y. Chen, G. Wang, X. Li, J. Dong, Q. Chen, W. Zhang, Z. Zhang, S. Liang, R. Yu, Y. Wang, D. Wang and Y. Li, *Angew. Chem., Int. Ed.*, 2020, **59**, 10651–10657.

245 H. Li, Q. Song, S. Wan, C. W. Tung, C. Liu, Y. Pan, G. Luo, H. M. Chen, S. Cao, J. Yu and L. Zhang, *Small*, 2023, **19**, 2301711.

246 Y. Li, B. Li, D. Zhang, L. Cheng and Q. Xiang, *ACS Nano*, 2020, **14**, 10552–10561.

247 M. Ma, Z. Huang, D. E. Doronkin, W. Fa, Z. Rao, Y. Zou, R. Wang, Y. Zhong, Y. Cao, R. Zhang and Y. Zhou, *Appl. Catal., B*, 2022, **300**, 120695.

248 G. Wang, C.-T. He, R. Huang, J. Mao, D. Wang and Y. Li, *J. Am. Chem. Soc.*, 2020, **142**, 19339–19345.

249 H. Yin, F. Dong, D. Wang and J. Li, *ACS Catal.*, 2022, **12**, 14096–14105.

250 D. Zeng, H. Wang, X. Zhu, H. Cao, Y. Zhou, W. Wang, L. Zhang and W. Wang, *Chem. Eng. J.*, 2023, **451**, 138801.

251 X. Li, W. Bi, L. Zhang, S. Tao, W. Chu, Q. Zhang, Y. Luo, C. Wu and Y. Xie, *Adv. Mater.*, 2016, **28**, 2427–2431.

252 G. Vilé, D. Albani, M. Nachtegaal, Z. Chen, D. Dontsova, M. Antonietti, N. López and J. Pérez-Ramírez, *Angew. Chem., Int. Ed.*, 2015, **54**, 10987.

253 Z. Chen, Q. Zhang, W. Chen, J. Dong, H. Yao, X. Zhang, X. Tong, D. Wang, Q. Peng, C. Chen, W. He and Y. Li, *Adv. Mater.*, 2018, **30**, 1704720.

254 L. Cheng, H. Yin, C. Cai, J. Fan and Q. Xiang, *Small*, 2020, **16**, 2002411.

255 X. Shi, Y. Huang, Y. Bo, D. Duan, Z. Wang, J. Cao, G. Zhu, W. Ho, L. Wang, T. Huang and Y. Xiong, *Angew. Chem., Int. Ed.*, 2022, **61**, e202203063.

256 W. Xie, K. Li, X.-H. Liu, X. Zhang and H. Huang, *Adv. Mater.*, 2023, **35**, 2208132.

257 M. Ma, Z. Huang, D. E. Doronkin, W. Fa, Z. Rao, Y. Zou, R. Wang, Y. Zhong, Y. Cao, R. Zhang and Y. Zhou, *Appl. Catal., B*, 2022, **300**, 120695.

258 X. Li and Z. Xiang, *Nat. Commun.*, 2022, **13**, 57.

259 J. Gu, C.-S. Hsu, L. Bai, H. M. Chen and X. Hu, *Science*, 2019, **364**, 1091–1094.

260 D. Grammatico, A. J. Bagnall, L. Riccardi, M. Fontecave, B.-L. Su and L. Billon, *Angew. Chem., Int. Ed.*, 2022, **61**, e202206399.

261 Y. Liang and R. Anwander, *Dalton Trans.*, 2013, **42**, 12521–12545.

262 P. Serna and B. C. Gates, *Acc. Chem. Res.*, 2014, **47**, 2612–2620.

263 C. Copéret, M. Chabanas, R. Petroff Saint-Arroman and J.-M. Basset, *Angew. Chem., Int. Ed.*, 2003, **42**, 156–181.

264 M. Rimoldi and A. Mezzetti, *Catal. Sci. Technol.*, 2014, **4**, 2724–2740.

265 J.-M. Basset, F. Lefebvre and C. Santini, *Coord. Chem. Rev.*, 1998, **178–180**, 1703–1723.

266 S. R. Docherty and C. Copéret, *J. Am. Chem. Soc.*, 2021, **143**, 6767–6780.

267 H. Ma, Y. Wang, Y. Xu and W. Shi, *Appl. Catal., B*, 2024, **349**, 123857.

268 D. Li, M. Kassymova, X. Cai, S.-Q. Zang and H.-L. Jiang, *Coord. Chem. Rev.*, 2020, **412**, 213262.

269 J. Wang, X.-F. Cui, B. Liu, S. Ling, R. Long and Y.-J. Xiong, *J. Am. Chem. Soc.*, 2018, **140**, 16514–16520.

270 P. Du, Y.-N. Bo, H. Li, R. Liu, C.-M. Wang, H.-J. Liu, T. K. D. Liu, Z. Lu, C. Gao and Y.-J. Xiong, *Appl. Catal., B*, 2023, **330**, 122667.

271 H. Wang, Z. Zhan, Q. Huang, S.-Q. Li, X.-X. Yi, Q. Tang and J.-Y. Wang, *Small*, 2022, **18**, 2105083.

272 Y. Xiao and T.-S. Chung, *Energy Environ. Sci.*, 2011, **4**, 201–208.

273 Z. Zhang, H. Gao, H. Wu, Y. Qian, L. Chen and J. Chen, *ACS Appl. Nano Mater.*, 2018, **1**, 6463–6476.

274 Q. Peng, B. Gong and G. N. Parsons, *Nanotechnology*, 2011, **22**, 155601.

275 V. Rozyyev, J. G. Murphy, E. Barry, A. U. Mane, S. J. Sibener and J. W. Elam, *Appl. Surf. Sci.*, 2021, **562**, 149996.

276 C. Coperet, A. Comas-Vives, M. P. Conley, D. P. Estes, A. Fedorov, V. Mougel, H. Nagae, F. Nunez-Zarur and P. A. Zhizhko, *Chem. Rev.*, 2016, **116**, 323–421.

277 W. Yi, W. Yuan, Y. Meng, S. Zou, Y. Zhou, W. Hong, J. Che, M. Hao, B. Ye, L. Xiao, Y. Wang, H. Kobayashi and J. Fan, *ACS Appl. Mater. Interfaces*, 2017, **9**, 31853–31860.

278 T. W. Goh, C.-K. Tsung and W. Huang, *ACS Appl. Mater. Interfaces*, 2019, **11**, 23254–23260.

279 C. Dong, Y. Li, D. Cheng, M. Zhang, J. Liu, Y.-G. Wang, D. Xiao and D. Ma, *ACS Catal.*, 2020, **10**, 11011–11045.

280 K. Lian, Y. Yue, J.-M. Basset, X. Liu, L. Chen, C. Ozsoy-Keskinbora, X. Bao and H. Zhu, *J. Phys. Chem. C*, 2022, **126**, 16663–16671.

281 K. P. Kuhl, E. R. Cave, D. N. Abram and T. F. Jaramillo, *Energy Environ. Sci.*, 2012, **5**, 7050–7059.

282 X. Wang, Z. Jiang, H. Chen, K. Wang and X. Wang, *J. Alloys Compd.*, 2022, **896**, 163030.

283 Z. Miao, Y. Zhang, N. Wang, P. Xu and X. Wang, *J. Colloid Interface Sci.*, 2022, **620**, 407–418.

284 H. Huang, J. Zhao, B. Weng, F. Lai, M. Zhang, J. Hofkens, M. B. J. Roeffaers, J. A. Steele and J. Long, *Angew. Chem., Int. Ed.*, 2022, **61**, e202204563.

285 Q. Ge, Y. Liu, K. Li, L. Xie, X. Ruan, W. Wang, L. Wang, T. Wang, W. You and L. Zhang, *Angew. Chem., Int. Ed.*, 2023, **62**, e202304189.

286 R. Das, S. Chakraborty and S. C. Peter, *ACS Energy Lett.*, 2021, **6**, 3270–3274.

287 S. Yoshino, A. Iwase, Y. Yamaguchi, T. M. Suzuki, T. Morikawa and A. Kudo, *J. Am. Chem. Soc.*, 2022, **144**, 2323–2332.

288 R. Das, S. Sarkar, R. Kumar, S. D. Ramarao, A. Cherevotan, M. Jasil, C. P. Vinod, A. K. Singh and S. C. Peter, *ACS Catal.*, 2021, **12**, 687–697.

289 R. Pang, K. Teramura, M. Morishita, H. Asakura, S. Hosokawa and T. Tanaka, *Commun. Chem.*, 2020, **3**, 137.

290 H. Huang, J. Zhao, B. Weng, F. Lai, M. Zhang, J. Hofkens, M. B. J. Roeffaers, J. A. Steele and J. Long, *Angew. Chem., Int. Ed.*, 2022, **61**, e202204563.

291 H. Ou, S. Ning, P. Zhu, S. Chen, A. Han, Q. Kang, Z. Hu, J. Ye, D. Wang and Y. Li, *Angew. Chem., Int. Ed.*, 2022, **61**, e202206579.

292 Q. Shi, X. Zhang, Y. Yang, J. Huang, X. Fu, T. Wang, X. Liu, A. Sun, J. Ge, J. Shen, Y. Zhou and Z. Liu, *J. Energy Chem.*, 2021, **59**, 9–18.

293 D. Jiang, W. Wang, E. Gao, S. Sun and L. Zhang, *Chem. Commun.*, 2014, **50**, 2005–2007.

294 Y. Bai, P. Yang, L. Wang, B. Yang, H. Xie, Y. Zhou and L. Ye, *Chem. Eng. J.*, 2019, **360**, 473–482.

295 R. Bhosale, S. Jain, C. P. Vinod, S. Kumar and S. Ogale, *ACS Appl. Mater. Interfaces*, 2019, **11**, 6174–6183.

296 M. Wu, C. Chen, Y.-Y. Xu, C.-Y. Ma, M.-Y. Song and G.-B. Jiang, *J. Am. Chem. Soc.*, 2024, **146**, 9163–9171.

297 W. Yan, Y. Zhang and Y. Bi, *Angew. Chem., Int. Ed.*, 2023, **63**, e202316459.

298 S. Xue, C.-G. Wei, M.-S. Xiao, C. Liang, J.-L. Wang, C. Yang, W.-D. Xing, S.-B. Wang, W. Lin, Z.-Y. Yu and X. Wang, *Proc. Natl. Acad. Sci. U. S. A.*, 2024, **121**, e2319751121.

299 W. Bi, Y. Hu, H. Jiang, L. Zhang and C. Li, *Adv. Funct. Mater.*, 2021, **31**, 2010780.

300 C. Han, B. Wang, N. Wu, S. Shen and Y. Wang, *Appl. Surf. Sci.*, 2020, **515**, 145952.

301 Y.-Y. Li, J.-S. Fan, R.-Q. Tan, H.-C. Yao, Y. Peng, Q.-C. Liu and Z.-J. Li, *ACS Appl. Mater. Interfaces*, 2020, **12**, 54507–54516.

302 P. Yan, F. Ji, W. Zhang, Z. Mo, J. Qian, L. Zhu and L. Xu, *J. Colloid Interface Sci.*, 2023, **634**, 1005–1013.

303 X. Shi, Y. Huang, Y. Bo, D. Duan, Z. Wang, J. Cao, G. Zhu, W. Ho, L. Wang, T. Huang and Y. Xiong, *Angew. Chem., Int. Ed.*, 2022, **61**, e202203063.

304 J. Fan, L. Cheng, Y. Liu, Y. He, Y. Wang, D. Li and J. Feng, *J. Catal.*, 2019, **378**, 164–175.

305 R. Chong, Y. Fan, Y. Du, L. Liu, Z. Chang and D. Li, *Int. J. Hydrogen Energy*, 2018, **43**, 22329–22339.

306 W.-K. Jo, S. Kumar and S. Tonda, *Composites, Part B*, 2019, **176**, 107212.

307 J. Fan, L. Shi, H. Ge, J. Liu, X. Deng, Z. Li and Q. Liang, *Adv. Funct. Mater.*, 2024, 202412078.

308 J. Wu, J. Zhu, W. Fan, D. He, Q. Hu, S. Zhu, W. Yan, J. Hu, J. Zhu, Q. Chen, X. Jiao and Y. Xie, *Nano Lett.*, 2024, **24**, 696–702.

309 Y. Zhao, Y. Wei, X. Wu, H. Zheng, Z. Zhao, J. Liu and J. Li, *Appl. Catal., B*, 2018, **226**, 360–372.

310 X. Wu, H. Ling Tan, C. Zhang, Z. Teng, Z. Liu, Y. Hau Ng, Q. Zhang and C. Su, *Prog. Mater. Sci.*, 2023, **133**, 101047.

311 M. Xu, J. Yang, C. Sun, L. Liu, Y. Cui and B. Liang, *Chem. Eng. J.*, 2020, **389**, 124402.

312 S. Song, Z. Xing, H. Zhao, Z. Li and Z. Wei, *Green Energy Environ.*, 2023, **8**, 1232–1264.

313 Y. Zhao, Y. Wei, X. Wu, H. Zheng, Z. Zhao, J. Liu and J. Li, *Appl. Catal., B*, 2018, **226**, 360–372.

314 S. Yao, J. He, F. Gao, H. Wang, J. Lin, Y. Bai, J. Fang, F. Zhu, F. Huang and M. Wang, *J. Mater. Chem. A*, 2023, **11**, 12539–12558.

315 C. Hu, Z. Jiang, Q. Wu, S. Cao, Q. Li, C. Chen, L. Yuan, Y. Wang, W. Yang, J. Yang, J. Peng, W. Shi, M. Zhai, M. Mostafavi and J. Ma, *Nat. Commun.*, 2023, **14**, 4767.

316 Q. Liu, H. Cheng, T. Chen, T. W. B. Lo, Z. Xiang and F. Wang, *Energy Environ. Sci.*, 2022, **15**, 225–233.

317 C. Shen, X. Y. Meng, R. Zou, K. Sun, Q. Wu, Y. X. Pan and C. J. Liu, *Angew. Chem., Int. Ed.*, 2024, **63**, 202402369.

318 M. Ma, Z. Huang, L. Li, W. Zhang, R. Guo, R. Zhang, W. Fa, C. Han, Y. Cao, S. Yu and Y. Zhou, *Appl. Catal., B*, 2023, **330**, 122626.

319 H. Zhao, J. Duan, Z. Zhang and W. Wang, *ChemCatChem*, 2021, **14**, e202101733.

320 H. Guo, M. Chen, Q. Zhong, Y. Wang, W. Ma and J. Ding, *J. CO2 Util.*, 2019, **33**, 233–241.

321 X. Wang, Y. Wang, M. Gao, J. Shen, X. Pu, Z. Zhang, H. Lin and X. Wang, *Appl. Catal., B*, 2020, **270**, 118876.

322 M. Ma, Z. Huang, R. Wang, R. Zhang, T. Yang, Z. Rao, W. Fa, F. Zhang, Y. Cao, S. Yu and Y. Zhou, *Green Chem.*, 2022, **24**, 8791–8799.

323 W. Jiao, Y. Xie, F. He, K. Wang, Y. Ling, Y. Hu, J. Wang, H. Ye, J. Wu and Y. Hou, *Chem. Eng. J.*, 2021, **418**, 129286.

324 P. Ling, J. Zhu, Z. Wang, J. Hu, J. Zhu, W. Yan, Y. Sun and Y. Xie, *Nanoscale*, 2022, **14**, 14023–14028.

325 S. Gao, B. Gu, X. Jiao, Y. Sun, X. Zu, F. Yang, W. Zhu, C. Wang, Z. Feng, B. Ye and Y. Xie, *J. Am. Chem. Soc.*, 2017, **139**, 3438–3445.

326 Y. Wang, X. Liu, X. Han, R. Godin, J. Chen, W. Zhou, C. Jiang, J. F. Thompson, K. B. Mustafa, S. A. Shevlin, J. R. Durrant, Z. Guo and J. Tang, *Nat. Commun.*, 2020, **11**, 2531.

327 M. M. Kandy and V. G. Gaikar, *Mater. Res. Bull.*, 2018, **102**, 440–449.

328 S. Ijaz, M. F. Ehsan, M. N. Ashiq and T. He, *Catal. Sci. Technol.*, 2015, **5**, 5208–5215.

329 M. Habibi Zare and A. Mehrabani-Zeinabad, *ACS Appl. Energy Mater.*, 2023, **6**, 3173–3199.

330 W.-X. Shi, J.-R. Huang, S.-Y. Xu, H. Luo and J.-W. Zhang, *Adv. Mater.*, 2024, **36**, 2306906.

331 M. A. Gondal, M. A. Dastageer, L. E. Oloore and U. Baig, *J. Photochem. Photobiol., A*, 2017, **343**, 40–50.

332 M. Ma, Z. Huang, D. E. Doronkin and Y. Zhou, *Appl. Catal., B*, 2022, **300**, 120695.

333 G. Yin, H. Abe, R. Kodiyath, S. Ueda, N. Srinivasan, A. Yamaguchi and M. Miyauchi, *J. Mater. Chem. A*, 2017, **5**, 12113–12119.

334 Y. Wang, X. Shang, J. Shen, Z. Zhang, D. Wang, J. Lin, J. C. S. Wu, X. Fu, X. Wang and C. Li, *Nat. Commun.*, 2020, **11**, 3043.

335 M. Zhang, X. Wang, X. Qi, H. Guo, L. Liu, Q. Zhao and W. Cui, *J. Catal.*, 2022, **413**, 31–47.
336 Q. Zhu, Y. Cao, Y. Tao, T. Li, Y. Zhang, H. Shang, J. Song and G. Li, *J. CO2 Util.*, 2021, **54**, 101781.
337 J. He, P. Lv, J. Zhu and H. Li, *RSC Adv.*, 2020, **10**, 22460–22467.
338 D. O. Adekoya, M. Tahir and N. A. S. Amin, *J. CO2 Util.*, 2017, **18**, 261–274.
339 H. Wang, S. Cheng, X. Cai, L. Cheng, R. Zhou, T. Hou and Y. Li, *Catal. Commun.*, 2022, **162**, 106372.
340 P. Wang, X. Ba, X. Zhang, H. Gao, M. Han, Z. Zhao, X. Chen, L. Wang, X. Diao and G. Wang, *Chem. Eng. J.*, 2023, **457**, 141248.
341 Y.-C. Hao, L.-W. Chen, J. Li, Y. Guo, X. Su, M. Shu, Q. Zhang, W.-Y. Gao, S. Li, Z.-L. Yu, L. Gu, X. Feng, A.-X. Yin, R. Si, Y.-W. Zhang, B. Wang and C.-H. Yan, *Nat. Commun.*, 2021, **12**, 2682.
342 H. Ou, G. Li, W. Ren, B. Pan, G. Luo, Z. Hu, D. Wang and Y. Li, *J. Am. Chem. Soc.*, 2022, **144**, 22075–22082.
343 H. Xu, Z. Wang, H. Liao, D. Li, J. Shen, J. Long, W. Dai, X. Wang and Z. Zhang, *Appl. Catal., B*, 2023, **336**, 122935.
344 H. Li, M. Xia, X. Wang, B. Chong, H. Ou, B. Lin and G. Yang, *Appl. Catal., B*, 2024, **342**, 123423.
345 T. Billo, F. Y. Fu, P. Raghunath, I. Shown, W. F. Chen, H. T. Lien, T. H. Shen, J. F. Lee, T. S. Chan, K. Y. Huang, C. I. Wu, M. C. Lin, J. S. Hwang, C. H. Lee, L. C. Chen and K. H. Chen, *Small*, 2018, **14**, 1702928.
346 S. Sun, M. Watanabe, J. Wu, Q. An and T. Ishihara, *J. Am. Chem. Soc.*, 2018, **140**, 6474–6482.
347 T. Wang, L. Chen, C. Chen, M. Huang, Y. Huang, S. Liu and B. Li, *ACS Nano*, 2022, **16**, 2306–2318.
348 S. Chakraborty, R. Das, M. Riyaz, K. Das, A. K. Singh, D. Bagchi, C. P. Vinod and S. C. Peter, *Angew. Chem., Int. Ed.*, 2023, **135**, e202216613.
349 Z. Chen, G. Wang, T. Wang, D.-S. Wang and J.-J. Mao, *Angew. Chem., Int. Ed.*, 2022, **134**, e202210789.
350 Y. Tian, R. Wang, S. Deng, Y. Tao, W. Dai, Q. Zheng, C. Huang, C. Xie, Q. Zeng, J. Lin and H. Chen, *Nano Lett.*, 2023, **23**, 10914–10921.
351 K. Das, R. Das, M. Riyaz, A. Parui, D. Bagchi, A. K. Singh, A. K. Singh, C. P. Vinod and S. C. Peter, *Adv. Mater.*, 2022, **35**, 2205994.
352 B. Zhou, Y. Ma, P. Ou, Z. Ye, X.-Y. Li, S. Vanka, T. Ma, H. Sun, P. Wang, P. Zhou, J. K. Cooper, Y. Xiao, I. A. Navid, J. Pan, J. Song and Z. Mi, *Nat. Catal.*, 2023, **6**, 987–995.
353 W. Wang, C. Deng, S. Xie, Y. Li, W. Zhang, H. Sheng, C. Chen and J. Zhao, *J. Am. Chem. Soc.*, 2021, **143**, 2984–2993.
354 P. Du, J.-Y. Ding, J.-C. Zhu, Q. Hu, D.-P. He, Y. Wu, W.-X. Liu, S. Zhu, J. Hu, J.-F. Zhu, Q.-X. Chen, X.-C. Jiao and Y. Xie, *Angew. Chem., Int. Ed.*, 2024, **63**, e202400828.
355 R. t. Guo, J. Wang, Z. x. Bi, X. Chen, X. Hu and W. g. Pan, *Small*, 2022, **19**, 2206314.
356 J. Zhu, L. Zhou, Y. Zhu, J. Huang, L. Hou, J. Shen, S. Dai and C. Li, *Small*, 2022, **18**, 2104399.
357 A. Ziarati, A. Badiei, R. Grillo and T. Burgi, *ACS Appl. Mater. Interfaces*, 2019, **11**, 5903–5910.